Doctoral theses at NTNU, 2021:138

Marieke Olsman

Ultrasound and microbubble treatment for improved delivery of nanomedicine to tumours and the brain

Doctoral thesis

NTNU
Norwegian University of Science and Technology
Thesis for the Degree of
Philosophiae Doctor
Faculty of Natural Sciences
Department of Physics

NTNU
Norwegian University of
Science and Technology

Marieke Olsman

Ultrasound and microbubble treatment for improved delivery of nanomedicine to tumours and the brain

Thesis for the Degree of Philosophiae Doctor

Trondheim, April 2021

Norwegian University of Science and Technology
Faculty of Natural Sciences
Department of Physics

NTNU
Norwegian University of
Science and Technology

NTNU
Norwegian University of Science and Technology

Thesis for the Degree of Philosophiae Doctor

Faculty of Natural Sciences
Department of Physics

ISBN 978-82-326-5447-5 (printed ver.)
ISBN 978-82-326-5419-2 (electronic ver.)
ISSN 1503-8181 (printed ver.)
ISSN 2703-8084 (online ver.)

Doctoral theses at NTNU, 2021:138

Printed by NTNU Grafisk senter

Abstract

The combined use of ultrasound and intravascular microbubbles, referred to as ultrasound and microbubble treatment, has emerged as a promising technique to enhance delivery of nanomedicine to tumours and the brain. Even though the technique is on its way to the clinic, there are still various aspects to study and optimize to make ultrasound and microbubble treatment even more successful.

In this thesis we first investigated if ultrasound and microbubble treatment combined with nanoparticles exhibiting features to increase internalization by tumour cells upon ultrasound-mediated delivery would improve the therapeutic efficacy of the treatment. This was studied by combining ultrasound and microbubble treatment with liposomes coated with an enzymatic cleavable poly(ethylene) glycol (PEG) layer which upon cleaving may increase internalization of the liposomes by tumour cells and may destabilize the liposomal membrane resulting in accelerated drug release. For the enzyme sensitive liposome and the two types of control liposomes, ultrasound and microbubble treatment resulted in enhanced tumour accumulation, improved extravasation and increased tumour penetration depth of the liposomes. The therapeutic efficacy data indicated that the enzymatic feature of the liposome had a positive effect on the therapeutic efficacy, making it an interesting approach to increase the therapeutic efficacy of ultrasound and microbubble treatment.

Besides improving drug delivery to tumours, ultrasound and microbubble treatment can also be exploited to increase the permeability of the blood-brain barrier (BBB) by opening of tight junctions, creating endothelial cell openings and stimulating endo- and/or trans-cytosis. To exploit the different ultrasound induced transport pathways to the fullest, a high concentration of drug at the site of BBB disruption is favourable. By combining ultrasound and microbubble treatment with a liposome targeting the transferrin receptor on the BBB, it was investigated if this would enhance delivery of liposomes across the BBB compared to liposomes lacking the BBB-targeting moiety. The combined use resulted in a 40 % increase in accumulation of the BBB targeted liposomes whereas the control liposomes showed no increased accumulation. The results demonstrated that

ultrasound and microbubble treatment may enhance endocytosis of the BBB-targeting liposomes which could be an interesting approach to enhance drug delivery to the brain.

The potential of Acoustic Cluster Therapy® (ACT), a microbubble platform specifically engineered for therapeutic applications, to increase the permeability of the BBB and enhance delivery of nanomedicine to the brain was also explored. Directly upon ACT, increased BBB permeability was observed and one hour post ACT a 5.2-fold and 3.7-fold increase in accumulation of a model drug and clinically relevant core-crosslinked polymeric micelles (CCPM) was detected, respectively. Confocal microscopy images of the ACT-treated brains verified the improved extravasation and penetration of the CCPM into the brain parenchyma. Histological analysis of brain sections revealed no treatment related tissue damage. With this study we demonstrated that ACT safely and transiently increases the permeability of the BBB and improves accumulation and distribution of nanomedicine to the brain.

ACT is expected to work by a different mechanism compared to conventionally used microbubbles such as SonoVue™. An intravital microscopy set-up to unravel the mechanism of action of ACT in the brain was therefore established with help of experienced collaborators. The surgical and technical procedures required to conduct *in vivo* multiphoton imaging simultaneously with ultrasound and microbubble treatment were described in detail.

To summarize, the work presented in this thesis has increased our understanding on how ultrasound and microbubble treatment can be used to improve delivery of nanomedicine to tumours and the brain. Even though there is still a lot to learn, the increasing number of (pre)clinical studies demonstrates that ultrasound and microbubble treatment could impact medicine by enhancing drug delivery and thereby improving and enabling treatment of various cancer types and several brain diseases.

Acknowledgements

The work presented in this thesis would not have been possible without the valuable contributions and support of numerous people and I would like to acknowledge some of them in particular.

First, I would like to thank my supervisor Catharina who has guided me through my PhD with great expertise. Your constructive feedback, advice and unlimited optimism has been extremely supportive. It really has been a privilege to have been part of your research group. Moving to Trondheim to work on such exciting projects has definitely been one of my best decisions in life. In addition, I would like to thank my co-supervisor Sigrid for answering all my questions on microbubbles and ultrasound, and for all the valuable advice you have given me throughout my PhD.

Part of the work presented in this thesis has been the result of a collaboration with the Technical University of Denmark (DTU). I would like to thank Thomas who co-supervised me and who together with Catharina initiated the collaboration and secured funding for my PhD position. A special thanks to Viktoria for synthesizing and characterizing all of the liposomes used in this thesis, the great days in the MRI lab and all our nice discussions. Andrew, thank you for your valuable input in discussions and for sharing your knowledge on nanomedicine.

A big thank you to all my co-authors for their contributions to my papers. I also would like to thank all the people at AKM, CAM, CMIC and the MRI facility that have helped me with my experiments. In addition, I would like to thank Cristal Therapeutics for providing nanoparticles and Exact therapeutics for the unlimited access to ACT. In particular I would like to thank Spiros who answered all our 'challenging' questions and his valuable input to experiments.

I would like to thank all my colleagues at the Biophysics and Medical Technology section for the nice work atmosphere they created. I really enjoyed all our lunches, coffee breaks and evenings together. I would especially like to thank my research group for all the great (scientific) discussions and research

collaborations. In particular Melina, who was the 'lucky one' to work with me the most.

A lot of the work presented in this thesis has been produced in the best office in the hallway. To all my previous and current officemates, thank you for all the small talk, the 'MellomBar' competition, motivational speeches and scientific discussions. Due to all of you there has never been a bad day at the office.

I would also like to thank my teammates of the NTNU-SINTEF women football team. You all were an important part of my life in Trondheim and I really enjoyed our training sessions, matches and social gatherings. Hopefully we can soon stand on the football pitch again!

Special thanks to the 'SpS group' for all the Sunday dinners, hiking and cabin trips, moose safari, game nights and other social gatherings. Some of my best memories of Norway involves all of you! I really hope we can stay in touch and enjoy some more evenings filled with nice food, games, laughter, big eyes, beer and (maybe) some Jägermeister.

Ook in Nederland zijn er de nodige mensen die ik graag wil bedanken. Ten eerste de 'Dr Phillies' voor alle city trips, surprise-eieren eten, nutteloze discussies, pubquizes en andere gezellige avonden. Daarnaast waardeer ik al het bezoek dat ik hier de laatste jaren in Trondheim heb mogen ontvangen en ben ik blij dat ik ondanks de afstand met veel vrienden in Nederland contact heb kunnen houden.

Verder wil ik graag mijn ouders, broers, zussen en andere familieleden bedanken voor hun begrip en steun. De aankondiging dat ik had besloten om een baan in Noorwegen aan te nemen kwam waarschijnlijk als een grote verrassing, maar ondanks dat hebben jullie altijd interesse getoond in mijn werk en gesteund waar nodig.

Tot slot wil ik in het bijzonder Colin bedanken. Al jarenlang gedoogt hij mijn slechte muzieksmaak, rijdt hij mij tijdens vakanties uiterst professioneel rond en voorziet hij mij van de meest nutteloze feitjes. Bedankt voor je ontelbare bezoekjes, steun, geduld en nuchterheid wanneer ik het even nodig had.

Takk Norge! | *Goodgoan!*

List of papers

The following papers are included in this thesis:

1. **Ultrasound-mediated delivery enhances therapeutic efficacy of MMP sensitive liposomes**

   Marieke Olsman, Viktoria Sereti, Kristine Andreassen, Sofie Snipstad, Annemieke van Wamel, Rasmus Eliasen, Sigrid Berg, Andrew James Urquhart, Thomas Lars Andresen, Catharina de Lange Davies

   Journal of Controlled Release

   DOI: 10.1016/j.jconrel.2020.06.024

   MO and VS designed and planned the study with assistance of AJU, TLA and CD. MO conducted the in vitro and in vivo studies and analysed all the data. VS and RE synthesized and characterized the liposomes. KA performed microscopy of tissue sections. SS, AvW and SB participated in the in vivo experiments. MO wrote the manuscript. All authors contributed in the revision and discussion of the paper.

2. **Focused ultrasound and microbubble treatment increases delivery of transferrin receptor-targeting liposomes to the brain**

   Marieke Olsman, Viktoria Sereti, Melina Mühlenpfordt, Kasper Bendix Johnsen, Thomas Lars Andresen, Andrew James Urquhart, Catharina de Lange Davies

   Ultrasound in Medicine and Biology

   DOI: 10.1016/j.ultrasmedbio.2021.01.014

   MO and VS designed and planned the study with assistance of AJU, KBJ, TLA and CD. MO conducted the in vivo studies, performed microscopy

imaging and analysed the data. VS synthesized and characterized the liposomes. VS and MM participated in the in vivo experiments. VS and KBJ conducted mass spectroscopy of brain tissue. MO wrote the manuscript. All authors contributed in the revision and discussion of the paper.

3. Acoustic Cluster Therapy (ACT®) increases blood-brain permeability and enhances accumulation of core-crosslinked polymeric micelles

Marieke Olsman*, Melina Mühlenpfordt*, Emma Bøe Olsen, Sverre Helge Torp, Spiros Kotopoulis, Cristianne Rijcken, Qizhi Hu, Marielle Thewissen, Sofie Snipstad, Catharina de Lange Davies

Prepared for submission to Journal of Controlled Release upon intellectual property submission

**Equal contribution*

MO, MM, SK, SS and CD designed and planned the study. MO and MM conducted the in vivo studies and analysed all the data. EBO performed microscopy of brain sections. SHT evaluated the histology. CR, QH and MT synthetized and characterized the nanoparticles. MO and MM wrote the manuscript. All authors contributed in the revision and discussion of the paper.

4. Real-time intravital multiphoton microscopy to visualize focused ultrasound and microbubble treatments to increase blood-brain barrier permeability

Charissa Poon, Melina Mühlenpfordt*, Marieke Olsman*, Spiros Kotopoulis, Catharina de Lange Davies, Kullervo Hynynen

Submitted to Journal of Visualized Experiments

**Equal contribution*

CP, MM and MO acquired images and representative results for the manuscript. MM and MO performed the filming of the video. SK developed the ring transducer. CP, MM and MO wrote the manuscript with contributions of CD and KH. All authors contributed in the revision and discussion of the paper.

List of abbreviations

ABC	ATP binding cassette
ACT	Acoustic cluster therapy
ATP	Adenosine triphosphate
BBB	Blood-brain barrier
BBBD	Blood-brain barrier disruption
BCEC	Brain capillary endothelial cell
CAF	Cancer associated fibroblast
CCPM	Core-crosslinked polymeric micelles
CLSM	Confocal laser scanning microscopy
DLS	Dynamic light scattering
ECM	Extracellular matrix
EPR	Enhanced permeability and retention
FITC	Fluorescein isothiocyanate
FUS	Focused ultrasound
Gd	Gadolinium
HIFU	High intensity focused ultrasound
ICP-MS	Inductively-coupled plasma mass spectrometry
IFP	Interstitial fluid pressure
IgG	Immunoglobulin G
MB	Microbubble
MDR	Multidrug resistance

MI	Mechanical index
MMP	Matrix metalloproteinases
MRI	Magnetic resonance imaging
PDI	Polydispersity index
PEG	Poly(ethylene) glycol
P-gp	P-glycoprotein
PRF	Pulse repetition frequency
ROI	Region of interest
ROS	Reactive oxygen species
TAM	Tumour associated macrophage
TfR	Transferrin receptor

Contents

Chapter 1 – Background

This thesis revolves around the combined use of ultrasound and microbubbles, referred to as ultrasound and microbubble treatment, to improve delivery of drug loaded nanoparticles to tumours and the brain. **Section 1.1** will discuss the use of nanoparticles as drug delivery vehicles followed by a brief description of the targeting strategies that can be employed to improve drug accumulation in tumours. In **section 1.2** the biological barriers which prevent efficient delivery of drug and drug carriers to tumours are discussed, and strategies to overcome these barriers are presented. This is followed up by **section 1.3** describing the blood-brain barrier (BBB), the main barrier which prevents drug delivery to the brain. Besides the anatomy of the BBB, the different transport pathways that may be used for drug delivery are briefly discussed, followed by a paragraph on approaches that have been studied to overcome the BBB. Lastly, **section 1.4** describes how ultrasound and microbubbles can be used to enhance drug delivery to tumours and the brain. The mechanisms are not fully elucidated yet but the currently known induced biophysical effects will be discussed. In addition, an overview of clinical trials employing ultrasound and microbubble treatment for enhanced drug delivery is given.

1.1 Nanomedicine

Nanotechnology used for medical purposes such as diagnosing, monitoring, prevention and treatment of diseases is referred to as nanomedicine [10]. This section will mainly discuss the use of nano-sized drug carriers (e.i. nanoparticles) as drug delivery vehicles since the other applications of nanomedicine are not part of the scope of this thesis.

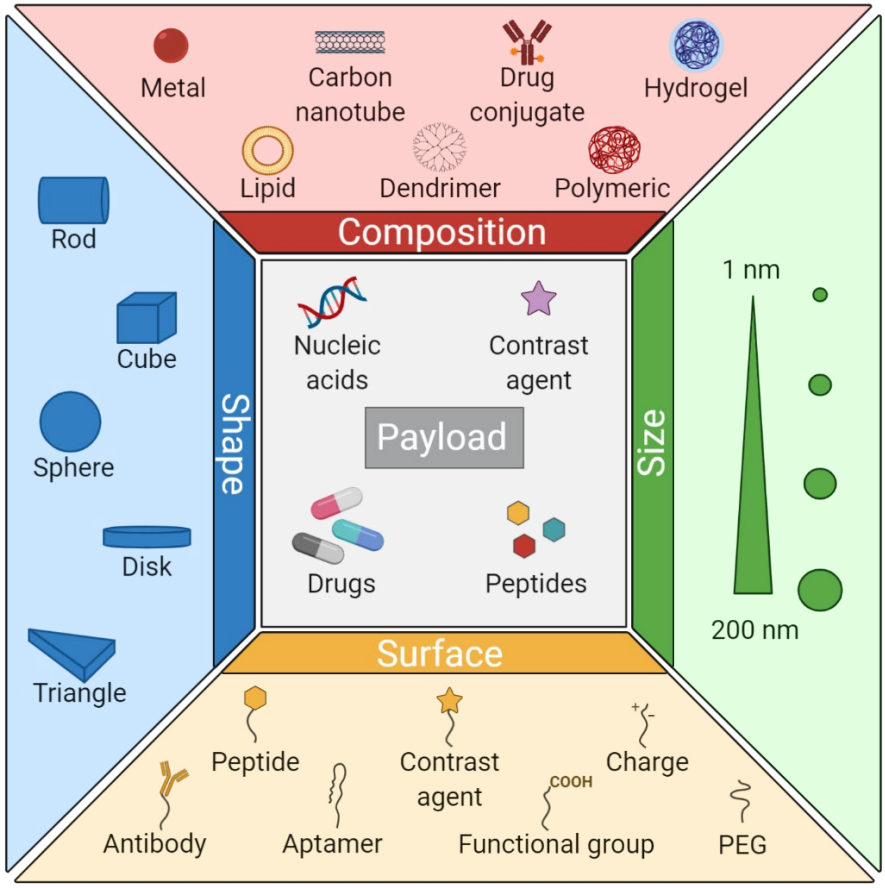

Figure 1. Schematic overview describing the multifunctionality and versatility of nanoparticles. Besides different shapes and sizes, nanoparticles can be composed of different materials and their surface can be decorated and modified. Different types of payloads can be incorporated in the nanoparticle. Figure is inspired by [8] and created with BioRender.

1.1.1 Nanoparticles as drug delivery vehicles

One of the most studied application of nanomedicine is using nanoparticles as drug delivery vehicles, especially for cancer treatment [11-13]. Various nanoparticle-based drug delivery systems have been developed, including polymeric, liposomal and inorganic nanoparticles [11, 14, 15]. A range of different sizes of nanoparticles can be established and by modifying the surface of nanoparticles, further tailoring is possible. Depending on their application, various molecules such as fluorescent dyes, drugs or targeting ligands can be incorporated. An illustration of the multivalence of nanoparticles is shown in **Figure 1**. Nanoparticles offer several advantages over the use of free drug. Due to their size and shape, nanoparticles have a high drug loading capacity which allows loading of several types and even combinations of drug molecules [11, 14]. Especially poorly soluble drugs can benefit from the encapsulation in nanoparticles. In addition, nanoparticles are able to exploit the tumour specific enhanced permeability and re (EPR) effect. The latter will be explained in more detail in the next section. Furthermore, encapsulating drugs in nanoparticles will result in a prolonged circulation time due to their larger size opposed to free drug molecules, and may reduce toxicity [15].

1.1.2 Targeting strategies

To improve accumulation and retention of drug loaded nanoparticles in tumour tissue, various tumour targeting strategies can be employed. The different strategies are illustrated in **Figure 2** and will be briefly discussed in this section.

Passive targeting

Due to uncontrolled growth of tumours, tumour endothelial cells are poorly aligned, resulting in large fenestrations through which drug molecules and nanoparticles can leak out and enter the tumour interstitial space. Combined with a defective lymphatic system which reduces clearance, this results in retention of the extravasated agents. This phenomenon is referred to as the enhanced permeability and retention (EPR) effect and is a specific feature of tumour tissue and therefore a popular tumour targeting strategy [16-18]. By exploiting the EPR-effect, drug molecules and nanoparticles can passively accumulate in tumour tissue.

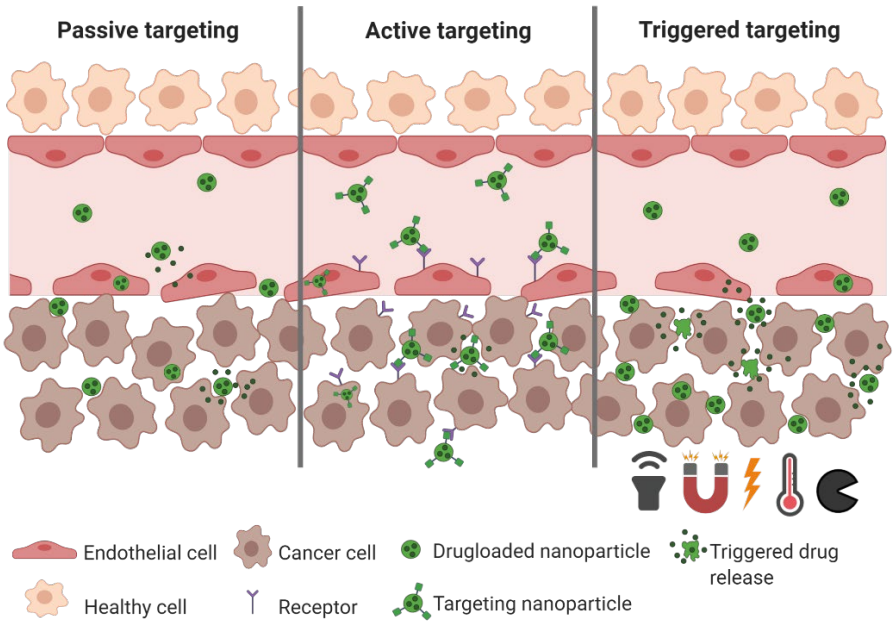

Figure 2. Schematic illustration of the different tumour targeting strategies that can be employed to enhance drug delivery to tumour tissue. Passive targeting is based on the extravasation and accumulation of nanoparticles by the EPR-effect. Active targeting comprises the use of nanoparticles with targeting capabilities towards tumour endothelial cells or cancerous cells. Triggered targeting is based on the use of stimuli-responsive drug carriers or external stimuli to increase accumulation of the drug carrier at the targeted site. Figure created with BioRender.

Active targeting

Active targeting can be achieved by decorating nanoparticles with ligands which bind to receptors expressed on the cell plasma membrane of target cells [19]. Receptors which are solely expressed or overexpressed on the surface of the target cell are of particular interest. In general, the target cells are either tumour endothelial cells or cancerous cells. Targeting tumour endothelial cells may be most efficient since contact between nanoparticles and endothelial cells will be more frequently achieved. Active targeting of cancerous cells still relies on passive accumulation of the nanoparticles by the EPR-effect. Although the active targeting approach may seem to be a promising strategy to increase drug carrier accumulation in tumours, it is questioned whether the active targeting approach is actually leading to increased accumulation. Instead, the observed improved therapeutic efficacy for active targeting drug delivery systems is mainly assigned to increased internalization rates of the targeting nanoparticles by tumour cells

[20-23]. The lack of drug carrier accumulation may be caused by binding of extravasated drug carriers to the first layer of cancerous cells they encounter which may impede further extravasation and penetration of the drug carriers [21, 24]. Optimizing the binding affinity of the targeting ligand to the receptor of interest may therefore be necessary to enable deeper tumour penetration.

Triggered targeting

Drug delivery to tumour tissue can be improved by using stimuli-responsive drug carriers. Several stimuli-responsive drug carriers have been developed with sensitivity towards, for example, enzymes, pH-changes, temperature, light and ultrasound [25]. When stimuli-responsive drug carriers are exposed to a specific stimulus, they will be triggered to locally release their drugs. Another way of triggered targeting is by using external forces such as a magnetic field or ultrasound to improve accumulation of the drug carrier at the target site [26-29]. Especially the combined use of ultrasound and intravascular microbubbles has shown to greatly increase the accumulation, distribution and therapeutic efficacy of drug and drug carriers in tumours and the brain [29-32]. How this can be achieved will be extensively discussed in **section 1.4 Therapeutic ultrasound**.

1.2 Drug delivery to tumours

Upon intravenous administration, nanomedicine will face several biological barriers before reaching and treating their target, the tumour cell. The three main biological barriers that nanoparticles have to overcome are 1) the blood barrier, 2) the tumour tissue barrier and 3) the cellular barrier [33-35]. Each of these barriers vary highly between different types of cancer and will affect the overall therapeutic effect. Understanding these barriers and how they affect nanoparticle delivery is necessary when designing new nanoparticle-based drug delivery systems and cancer therapies. In this section the different challenging aspects of the three aforementioned barriers will be discussed and current methods of overcoming these barriers will be given.

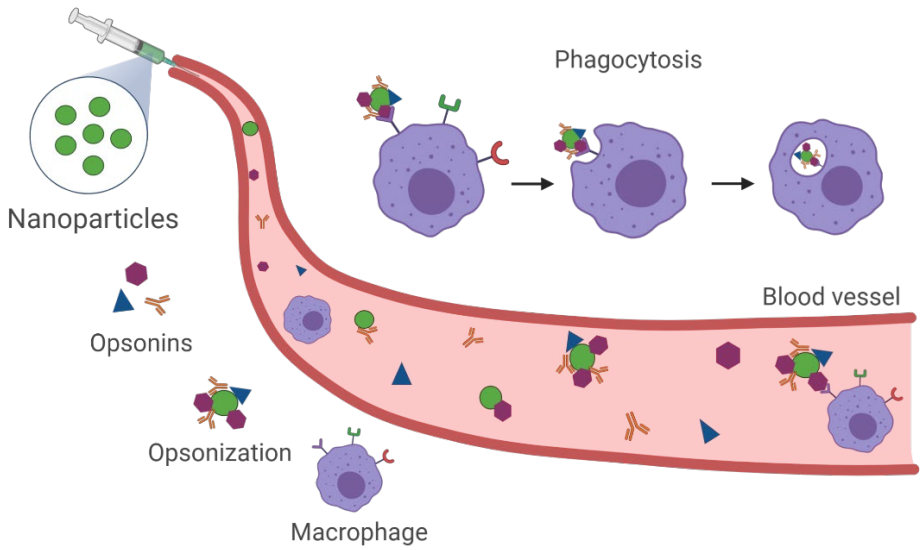

Figure 3. Graphical illustration of opsonization followed by phagocytosis of the nanoparticle by a macrophage. Upon intravenous injection, opsonins bind to the nanoparticles (opsonization) resulting in recognition by phagocytes such as macrophages. These macrophages will phagocytose the nanoparticles thereby removing them from the blood stream. Figure created with BioRender.

1.2.1 The blood barrier

Opsonization and clearance

Once introduced to the bloodstream, plasma proteins (e.i. opsonins) will attach to the surface of nanoparticles forming a protein corona. This process is referred

to as opsonization. The formed protein corona will trigger phagocytes such as macrophages, to internalize the nanoparticles and clear them from the bloodstream before they can become effective [33, 35]. A graphical illustration of opsonization followed by phagocytosis can be found in **Figure 3**. Minimizing opsonization will result in a prolonged circulation time which is beneficial for the therapeutic efficacy of the nanoparticles. The most common way to achieve this is by coating nanoparticles with the hydrophilic polymer poly(ethylene glycol) (PEG) [36-38]. The hydrophilic outer layer of PEGylated nanoparticles prevents binding of plasma proteins, thereby reducing recognition and internalization of the nanoparticles by phagocytes. Along with reduced opsonization, PEGylation of nanoparticles may also result in other beneficial effects such as less nanoparticle aggregation and a charge shielding effect of the NP [39, 40].

Circulation time

Besides opsonization, also the charge, size and shape of the NP will influence the circulation time and in vivo fate, and hence their potential therapeutic efficacy. Neutral nanoparticles (± 10 mV) exhibit a reduced rate of opsonization thereby prolonging their circulation time opposed to highly charged nanoparticles [39, 41-43]. Small nanoparticles (<5 nm) are quickly filtered out by kidneys while larger nanoparticles (>200 nm) mainly accumulate in the spleen and liver [39, 41, 43]. Traditionally, spherical nanoparticles are used for drug delivery purposes, however, due to advances in the nano manufacturing techniques, nanoparticles with different shapes and forms can now be developed in a controlled manner as well [44]. Although there is still a lot unknown about the *in vivo* behaviour of these non-spherical nanoparticles, they may exhibit several advantages over spherical nanoparticles. For example, whereas spherical nanoparticles tend to follow the laminar blood flow, non-spherical nanoparticles are more susceptible to flow forces and therefore tend to drift towards the vessel wall [45-47]. Additionally, non-spherical nanoparticles have a larger surface area opposed to spherical nanoparticles, resulting in a greater tendency to interact with the blood vessel wall and extravasate [33, 48-50]. It has also been demonstrated that using non-spherical shaped nanoparticles can reduce phagocytosis by macrophages, resulting in a prolonged circulation time compared to similar sized spherical nanoparticles [43, 51].

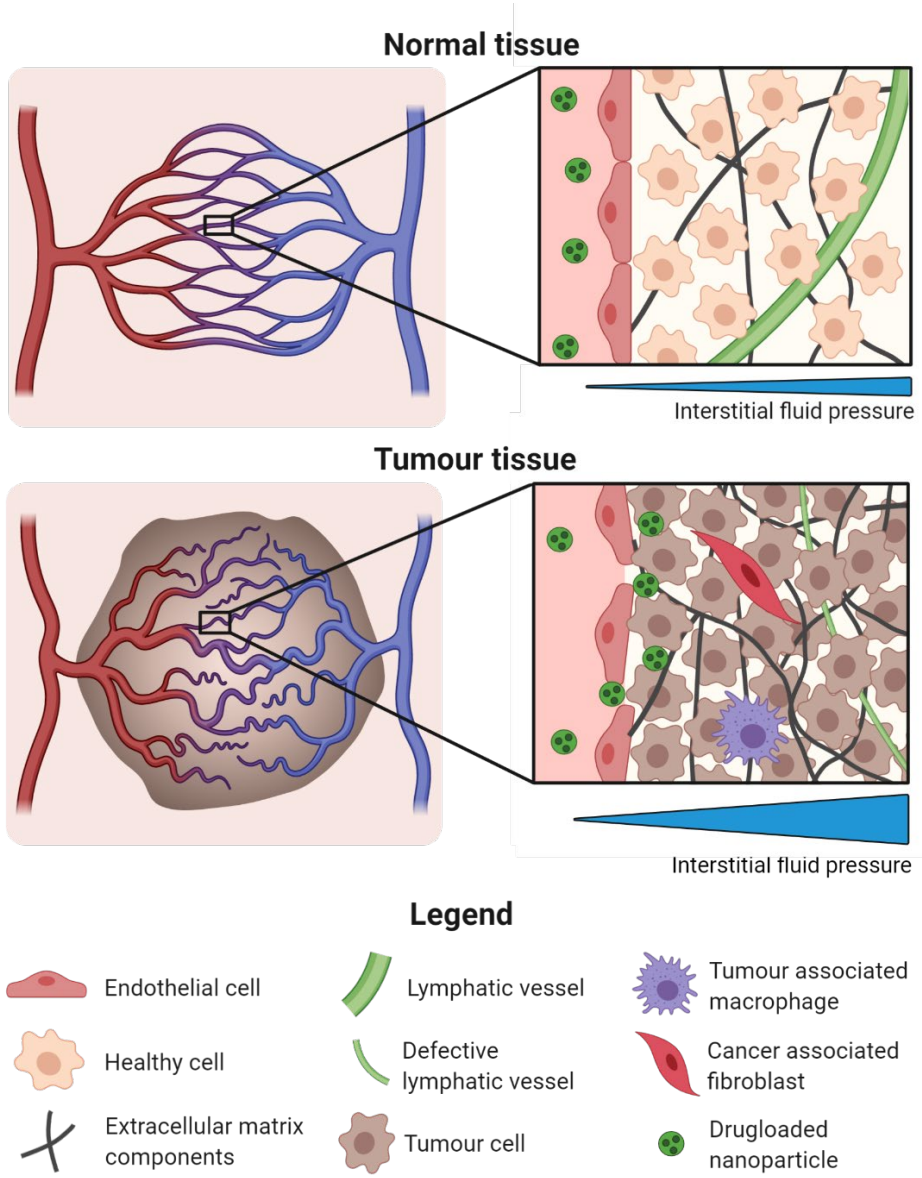

Figure 4. Graphical illustration of the tumour tissue barrier. Upon arriving at the tumour site, the intravenously administrated nanoparticles will encounter a poorly functional tumour vasculature with an abnormal architecture. Due to the EPR effect, nanoparticles will be able to passively accumulate in the tumour tissue. However, extravasated nanoparticles will encounter a tumour interstitium with high interstitial fluid pressure and dense extracellular matrix which hampers tumour penetration of the nanoparticles. In addition, upon extravasation, nanoparticles face the chance of being internalized by tumour associated macrophages and cancer associated fibroblasts. Figure created with BioRender.

1.2.2 Tumour tissue barrier

The enhanced permeability and retention effect

Upon arriving at the tumour site, the systemically administered nanoparticles will encounter a poorly functional vasculature (**Figure 4**). As already briefly described in **section 1.1.2 Targeting strategies**, the tumour vasculature is leaky due to poorly aligned endothelial cells resulting in large fenestrations. Drug and drug carriers that exploit the leakiness of the tumour vasculature and extravasate into the tumour will retain due to a defective lymphatic system which reduces clearance. This tumour specific phenomenon is referred to as the enhanced permeability and retention (EPR) effect and is an interesting target for tumour specific therapy strategies [16-18, 52, 53]. Even though the EPR effect is the main paradigm in cancer nanomedicine, the clinical relevance of the EPR-effect has been questioned, mainly due to the limited clinical success of nanomedicine. The high variability both spatial and temporal of the EPR-effect within a tumour but also between tumours is challenging [54]. In addition, our current understanding on the EPR-effect and the ability of nanoparticles to passively accumulate in tumours by exploiting the EPR-effect is mainly based on small animal tumour models which differ from clinical tumours in several key aspects (e.g. onset, vasculature, microenvironment) [54, 55]. These differences may make the EPR-effect more pronounced in small animal tumour models opposed to human tumours. To understand the reason of the limited clinical success of nanomedicine, more knowledge on the EPR-effect in human tumours is required.

Whereas transport through inter-endothelial gaps was assumed to be the main transport way of drug and drug carriers into the tumour, a trans-endothelial transport pathway has been suggested in the past as well, but evidence was sparse [56]. However, recent research has demonstrated that the major part of intravenously injected nanoparticles entered the tumour interstitium by active transport through the endothelial cells [57]. Further research is needed, but these findings indicate that we should reassess our current perspective and knowledge on transport pathways of nanoparticles into tumours.

Abnormal vasculature architecture

In addition to leakiness, the tumour vasculature exhibits an abnormal architecture, consists of dead ends, is unusual branched and has an uneven distribution of blood vessels, which is more clearly illustrated in **Figure 4** [33-35, 58]. These features create a highly heterogeneous vascular network [59, 60], resulting in high vascular resistance and different levels of perfusion within the

tumour thereby limiting the penetration and an even distribution of drugs and nanoparticles throughout the tumour [33, 61].

High interstitial fluid pressure

Upon accumulating in the tumour interstitium, drug molecules and nanoparticles have to be transported through the tumour extracellular matrix (ECM) to get to the tumour cell. Low molecular weight therapeutic agents are mainly transported by diffusion whereas larger therapeutic agents, such as nanoparticles, are mainly transported by convection. However, due to the poorly functioning vasculature combined with a defective lymphatic system and dense ECM, the interstitial fluid pressure (IFP) in solid tumours is high [62]. This limits convective transport and thus hinders nanoparticles from penetrating the tumour ECM, leaving diffusion or active transport as the main transport mechanism within the tumour ECM [63-65].

Extracellular matrix

Penetration of nanoparticles is further limited by the dense tumour ECM. The ECM is a highly dynamic three-dimensional non-cellular meshwork comprised of components such as collagen, elastin, glycosaminoglycan, proteoglycans and others, which determine the structure that surrounds cells and helps to regulate many important cellular processes [66]. The high tumour cell density, increased volume density of extracellular matrix components, gel-like appearance of the interstitial fluid and observed small pore sizes will hinder penetration of nanoparticles within the tumour [67, 68]. These tumour specific features of the extracellular matrix are more clearly illustrated in **Figure 4**.

Stromal cells

The ECM also houses several types of stromal cells including cancer-associated fibroblasts (CAFs) and tumour-associated macrophages (TAMs). Both are known to play an important role in the proliferation and metastasis of cancer cells and distribution of nanoparticles in tumour tissue [69, 70]. CAFs have been found to promote tumour growth, angiogenesis and tumour metastasis and do so by remodelling the ECM and secreting cytokines. In certain cancer types, CAFs have also been observed to express receptors similar to receptors expressed by tumour cells, resulting in internalization of nanoparticles by CAFs [69, 71]. TAMs are found throughout the tumour and greatly impact the level of accumulation of nanoparticles by phagocytosing extravasated nanoparticles. Although TAMs only account for a small number of the cells in the tumour, it has been observed that TAMs internalize a significant part of the extravasated nanoparticles compared to

tumour cells [70, 72, 73]. Besides phagocytosis of nanoparticles, TAMs also promote angiogenesis, tumour metastasis and immunosuppression by secreting cytokines [74].

Strategies to overcome tumour tissue barrier

The tumour tissue barrier can be partly overcome by selecting a suitable NP design or by remodelling or disruption of the tumour microenvironment. As discussed in **section 1.2.2 Tumour tissue barrier**, the nanoparticle size, shape, charge and composition affect the fate of the nanoparticles in overcoming the tumour tissue barrier. Different NP characteristics are favourable to overcome the different barriers discussed in this section. Whereas larger nanoparticles are favourable due to their prolonged circulation time, penetration will be limited by the high IFP and dense ECM. Smaller nanoparticles will be able to penetrate deeper into the tumour tissue, however, due to their smaller size, they will carry less payload and will be faster cleared from the circulation. A similar issue applies to the effect of the surface charge on tumour penetration. Neutral nanoparticles have a prolonged circulation time opposed to highly charged nanoparticles and are known to accumulate and penetrate tumour tissue well but have shown only low levels of internalization by tumour cells [75]. Whereas positively charged cells are easily internalized by tumour cells, they have a short circulation time and show poor tumour accumulation and penetration characteristics due to electrostatically interactions with components of the ECM [76]. Developing nanoparticles that are capable of changing size and/or charge at the different stages of delivery could therefore be favourable. This can for example be achieved by designing nanoparticles sensitive to changes in pH, enzymes or light [25, 77, 78].

Remodelling or disruption of the tumour microenvironment often focuses on either the tumour vasculature or the tumour ECM. Firstly, physical approaches such as ultrasound with and without microbubbles, radiation and near-infrared laser irradiation can improve vascular permeability, damage the vasculature or disrupt the tumour ECM thereby facilitating penetration of nanoparticles in tumour tissue [79]. Secondly, enzymes, such as collagenase and hyaluronidase, can be used prior to nanoparticle treatment to degrade the tumour ECM thereby improving nanoparticle penetration into the tumour tissue [80-83]. Lastly, chemical agents such as cyclopamine and losartan can be utilized to deplete components of the tumour ECM, reduce IFP and thus improve nanoparticle penetration in the tumour [84, 85].

1.2.3 Cellular barrier

Crossing the plasma membrane

Once nanoparticles succeed in overcoming the blood and tissue barrier, they should preferably enter the cell to release the drug into the cytoplasm. The first barrier they face is the plasma membrane. Small hydrophilic molecules will be able to diffuse easily through the membrane while nanoparticles have to enter the cell mainly through endocytosis.

Endocytosis of nanoparticles by tumour cells can happen through different pathways such as macropinocytosis, caveolae-mediated endocytosis, clathrin-mediated endocytosis or clathrin- and caveolae-independent endocytosis [3, 4]. A graphical illustration of these pathways can be found in **Figure 5**. NP properties such as size, shape, surface decoration and charge, play an important role in the type of endocytic pathway exploited and intracellular trafficking that follows [3]. Since many receptors on the plasma membrane of tumour cells are overexpressed, targeting these receptors can be an interesting approach to enhance endocytosis of nanoparticles.

Size, shape and surface decoration of the nanoparticles will determine the potential contact area, corresponding binding interaction between the nanoparticle and the plasma membrane, and the rate of internalization [3, 43, 86]. The latter is also highly affected by the surface charge of the nanoparticles [87]. Cell membranes are slightly negatively charged such that positively charged nanoparticles often achieve a higher internalization efficiency [87]. However, positively charged nanoparticles are cleared fast from the blood stream [88]. Designing nanoparticles which based on cues in the tumour microenvironment can transform from negatively charged to positively charged nanoparticles, could enhance internalization [33].

Drugs that work inside the nucleus must overcome the cell nuclear barrier in addition. Small drug molecules (less than 70 kDa) and small nanoparticles (less than 10 nm) can passively diffuse through the pores in the nuclear membrane. Access to the DNA can also be achieved during mitosis when the nuclear envelope has degraded.

Endosomes, lysosomes and nuclear delivery

As illustrated in **Figure 5**, upon internalization, nanoparticles are transported intracellularly in endocytic vesicles which fuse with an early endosome. Some nanoparticles entrapped in early endosomes will be expelled from the cell via

recycling endosomes, however, most early endosomes mature into late endosomes and fuse with lysosomes. These vesicles are highly acidic and contain various enzymes which can degrade nanoparticles and the drug it was carrying [3, 4]. Thus, nanoparticles need to achieve endosomal or lysosomal escape, to release their payload into the cytoplasm such that the drugs can become effective. Several types of nanoparticles capable of doing this have been designed [5].

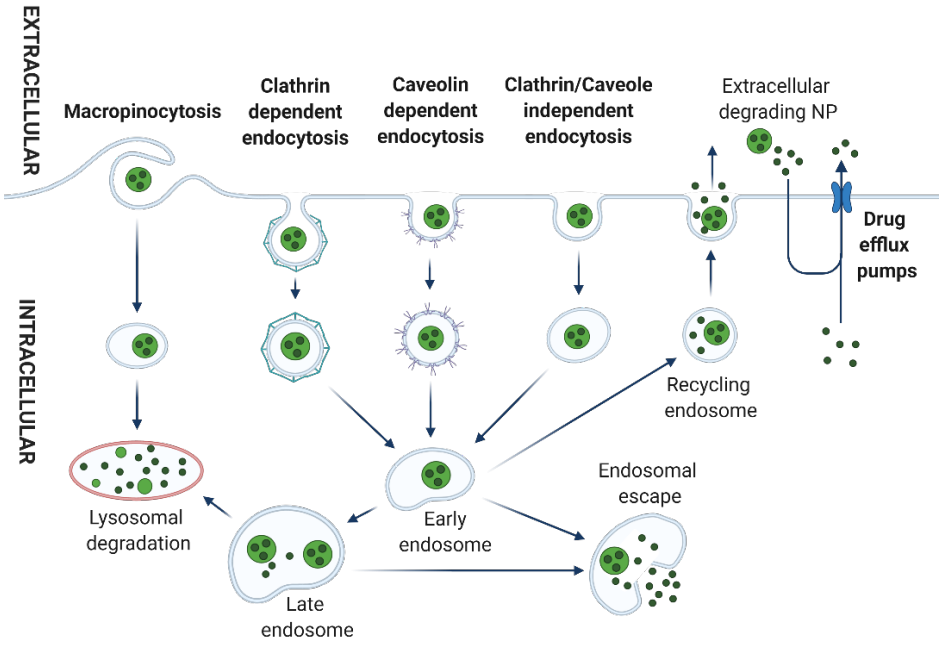

Figure 5. Graphical illustration of the endocytic pathways and intracellular trafficking that follows. In most cases, the drug loaded nanoparticles will end up in lysosomes and get degraded. Drug delivery to the cytosol can be achieved by endosomal escape. Free drug molecules in the cytosol face being secreted by the drug efflux pumps. Intracellular components such as the endoplasmic reticulum, Golgi apparatus, etc are for simplification reasons excluded from this illustration. Figure is inspired by [3-5] and created with BioRender.

Drug efflux pumps

Drugs in the cytoplasm face the chance of being inactivated or expelled from the cell due to multidrug resistance (MDR) mechanisms [89]. The most common mechanism exploited is pumping intracellular drugs out of the cell by ATP binding cassette (ABC) transporters. These transporters are often overexpressed on the cell membrane of tumour cells and brain capillary endothelial cells (BCECs) and result in reduced levels of intracellular drugs thereby affecting the therapeutic efficacy [89]. The P-glycoprotein (P-gp) transporter is one of the common

overexpressed ABC transporters and has the ability to pump hydrophobic chemotherapeutic agents out of the cell [90, 91]. Using nanoparticles which degrade and release their drugs extracellularly could therefore be unfavourable. However, intact nanoparticles are capable of circumventing the P-gp transporters. Another way to enhance intracellular drug concentrations and thus improve the treatment effect is by using MDR inhibitors.

1.3 Drug delivery to the brain

The blood-brain barrier (BBB) strictly controls the transport of substances into the brain thereby maintaining brain homeostasis and protecting the brain from harmful compounds [92, 93]. This, however, also results in limited access of most drugs thereby preventing efficient treatment of many brain diseases such as brain cancer, Alzheimer's disease and others [92, 93]. Understanding the structure and function of the BBB and transport mechanisms across the BBB will be useful when designing new nanoparticle-based drug delivery systems and delivery strategies.

1.3.1 The blood-brain barrier

The BBB roughly consists of endothelial cells, pericytes, astrocyte end feet, immune cells and the basement membrane, and is graphically illustrated in **Figure 6** [92, 94]. Brain capillaries are aligned with endothelial cells which are strongly bound together by tight junctions sealing the paracellular cleft and restricting paracellular transport [92, 94]. Tight junctions consist of transmembrane proteins such as claudins, occludins, junction adhesion molecules (JAM), and are connected to the cytoskeleton through intracellular adaptor proteins such as zonula occludens (ZO) and others [92, 94]. Besides the brain specific tight junctions, brain capillary endothelial cells (BCECs) are also tightly bound together by adherens junctions, an ubiquitous junctional complex in vasculature [95]. BCECs are morphologically and functionally different from other endothelial cells. They express higher levels of ABC transporters, contain higher number of mitochondria and show lower levels of leukocyte adhesion molecules [96]. The endothelial cell layer is supported by pericytes which are located at the abluminal side and are embedded in the basement membrane. Pericytes are capable of regulating blood flow by modulating capillary diameter and are important for maintaining BBB integrity [97]. Besides other functions, pericytes also aid angiogenesis and have been observed to have phagocytic capabilities [98, 99]. The basement membrane in which the pericytes are embedded provides mechanical stability to the vessel and a scaffold for cellular components of the BBB thereby also regulating intercellular communication by acting as a physical barrier [94, 96]. Astrocytes can be found in the brain parenchyma and are in direct contact with the basement membrane by their endfeet. They provide a link between the vasculature and neuronal circuit. Additionally, astrocytes are mainly known for their role in maintaining the BBB microenvironment by monitoring electrochemical activity, innate immune regulation and control levels of parenchymal water and metabolites [92, 94, 96].

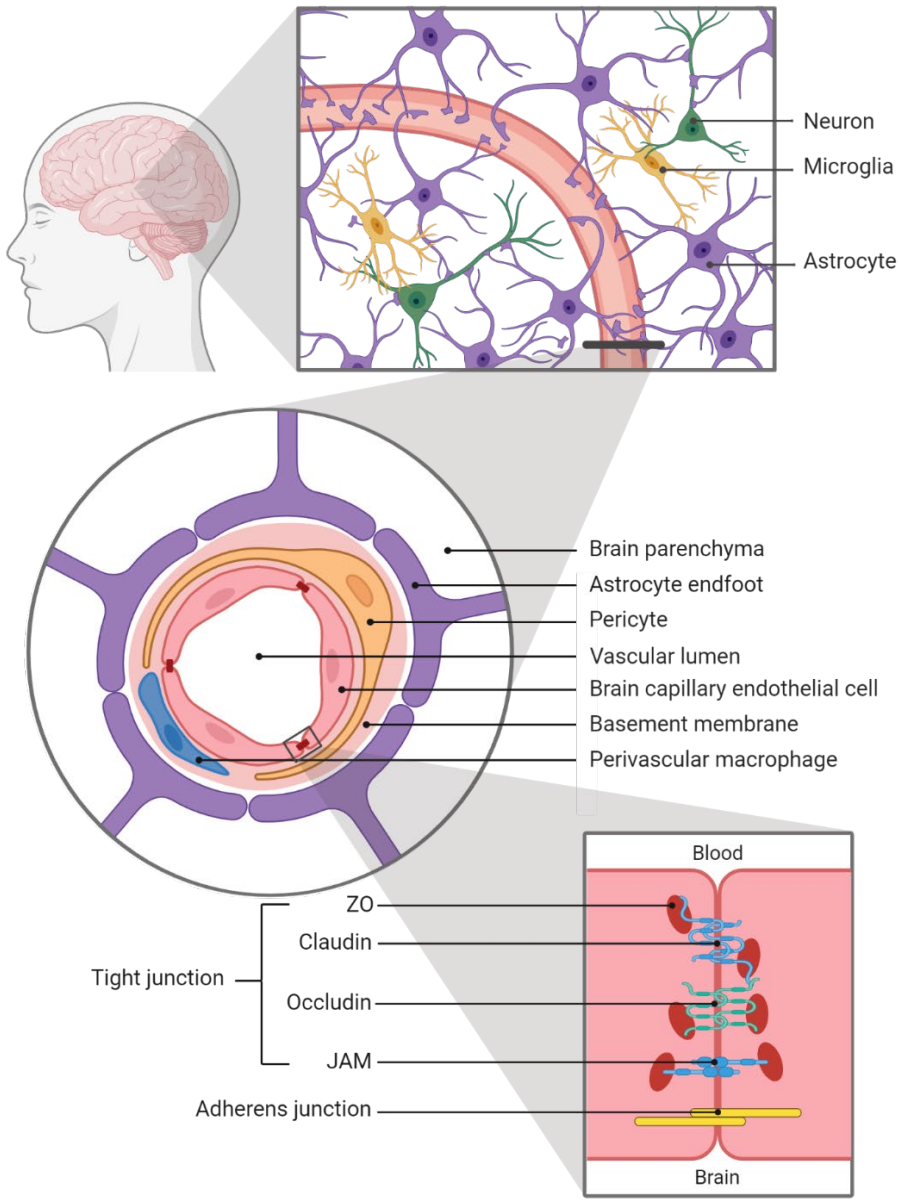

Figure 6. Graphical illustration of the blood-brain barrier (BBB). The BBB roughly consists of brain capillary endothelial cells, pericytes, astrocyte end feet, immune cells and the basement membrane. The brain capillary endothelial cells are strongly bound together by tight junctions thereby sealing the paracellular cleft and restricting paracellular transport. Perivascular macrophages and microglia are the two primary types of immune cells present in the BBB. Figure created with BioRender.

Perivascular macrophages and microglia are the two primary types of immune cells present in the BBB. Both have the ability to phagocytose cellular debris, pathogens and waste products thereby mediating immune response and maintaining the BBB integrity [96, 100]. Both immune cells are active players in several brain disorders and will affect accumulation and distribution of drug and drug carriers in brain tissue [96].

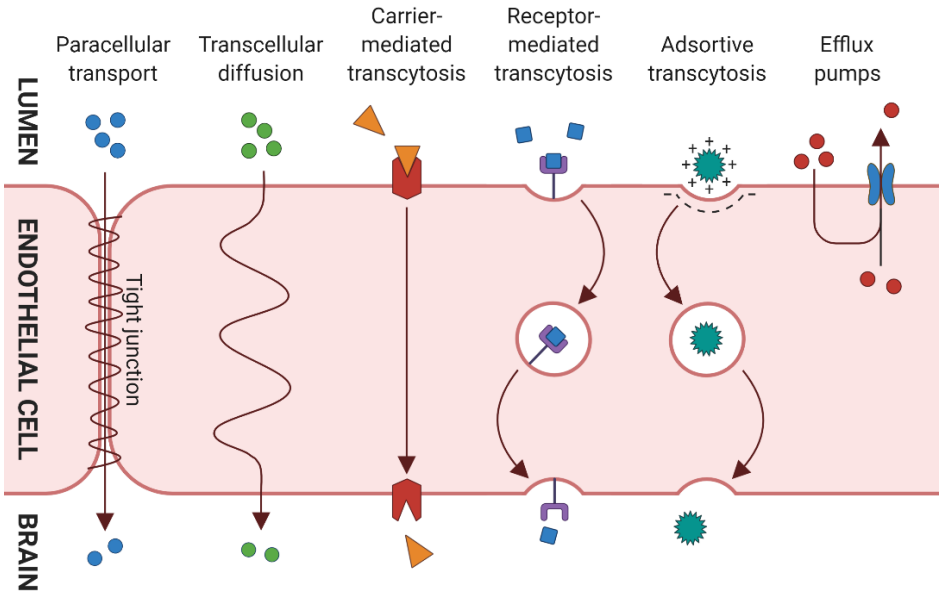

Figure 7. Graphical illustration of the different transport pathways across the blood-brain barrier. Figure is inspired by [6] and created with BioRender.

1.3.2 Transport pathways across the blood-brain barrier

Compounds can enter the brain parenchyma by para- or transcellular transport. Since paracellular transport is highly limited due to tight junctions sealing the inter-endothelial cleft, transport across the BBB is mainly restricted to transcellular pathways. Several transcellular pathways for drug delivery purposes can be exploited at the BBB and these are illustrated in **Figure 7**.

Gases (e.g. oxygen, carbon dioxide) and small lipophilic molecules (< 400 Da) can cross the BBB by transcellular diffusion [6, 93]. Transport proteins facilitate the transport across the BBB of larger molecules such as glucose (carrier-mediated transcytosis). A variety of macromolecules such as transferrin and

insulin binds to receptors on the BBB, following receptor-mediated endocytosis and release of the compound at the abluminal side [93, 101-104]. Cationic molecules (e.g. polymers, albumin) may interact with the negatively charged cell membrane and endocytosed through adsorptive endocytosis [102, 105].

Whereas the aforementioned transport mechanisms can be utilized for drug delivery across the BBB, drugs face the risk of getting expelled back into the lumen by drug efflux pumps which are overly expressed on the plasma membrane of BCECs opposed to regular endothelial cells [90, 106, 107].

1.3.3 Approaches to overcome the blood-brain barrier

Both non-invasive and invasive approaches to circumvent the BBB have been investigated for the last decades. Different designs of drugs, drug carriers and nanoparticles able to exploit the discussed transport mechanisms, have been developed. Unfortunately, due to the restrictive nature of the BBB, low delivery efficiencies are often obtained such that high intravenous doses are required to achieve relevant therapeutic concentrations at the target site often resulting in adverse systemic effects [93, 108]. The permeability of the BBB can temporarily be increased by using disruptive agents such as hyperosmotic solutions, vasodilators or chemical agents [109, 110]. However, these agents offer poor spatial control over the site of increased permeability. Additionally, many of the chemical agents used are toxic and may cause neuronal damage [109, 111]. Delivery of drugs through the nasal epithelium has been explored as well but showed low delivery efficiency [112-114]. Intracerebral or intraventricular injections were used for direct delivery of therapeutic agents to the target region, but these are highly invasive and thus unfavourable [115]. A more promising and non-invasive approach is the use of focused ultrasound in combination with intravascular microbubbles [116]. With this approach, reversible, temporal and local disruption of the BBB can be achieved which has demonstrated to facilitate delivery of chemotherapeutics, antibodies, nanocarriers and stem cells across the BBB [32, 111, 117-124].

1.4 Therapeutic ultrasound

Medical ultrasound is one of the most common and widely used imaging modalities in medicine. Besides diagnostic purposes such as visualizing internal organs, ultrasound can be used for therapeutic purposes such as disintegrating kidney stones, ablating tumours and enhancing drug delivery [125]. How these effects can be achieved will be explained in this section while focusing mainly on ultrasound-mediated drug delivery.

1.4.1 Ultrasound-induced effects

Ultrasound waves consist of alternating pressure deviations causing areas of compression (high pressure) and expansion (low pressure) of molecules in tissue [126]. When propagating through tissue, ultrasound waves will transfer energy to the tissue as thermal and mechanical energy. This can cause hyperthermia, produce radiation force or generate cavitation [125, 127]. Each of these ultrasound-induced effects can be used for therapeutic purposes.

Therapeutic ultrasound is often described by its frequency, negative peak pressure, pulse duration, pulse repetition frequency (PRF), duty cycle and total treatment time [126, 127]. The definition of these parameters is illustrated in **Figure 8**.

Hyperthermia

Sound waves will be absorbed by tissue whereby the rate of absorption is in general frequency dependent. Absorption of the acoustic energy can generate heat which may result in a local temperature increase when it exceeds the rate of heat dissipation. By focusing the ultrasound beam on a precisely defined area in the target tissue and locally heat the tissue, tissue damage can be induced. This non-invasive therapeutic ultrasound technique is referred to as high intensity focused ultrasound (HIFU) and is currently used to, for example, ablate tumours and treat Parkinsonian tremor [125, 128, 129]. Small temperature increases can also be induced by HIFU which have shown to have several biophysical effects (e.g. increased blood flow, enhanced vascular permeability, etc.) which may improve accumulation and distribution of therapeutic agents in tumours [130-136]. Local ultrasound-induced heating can also be combined with thermosensitive drug carriers yielding local drug release [137].

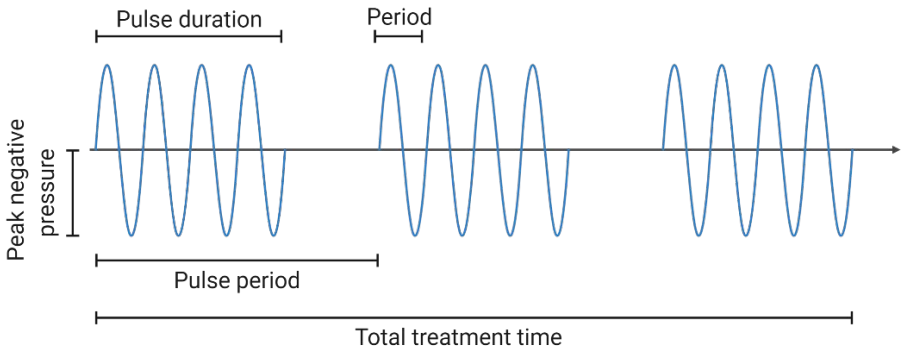

Relevant equations

$$\text{Frequency} = \frac{1}{\text{Period}} \qquad \text{Pulse repetition frequency (PRF)} = \frac{1}{\text{Pulse period}}$$

$$\text{Mechanical index (MI)} = \frac{\text{Peak negative pressure}}{\sqrt{\text{Frequency}}} \qquad \text{Duty cycle} = \frac{\text{Pulse duration}}{\text{Pulse period}} \times 100$$

Figure 8. Graphical illustration of pulsed ultrasound waves often used for therapeutic purposes. The sinus describes areas of high pressure (peaks) and low pressure (valleys). Definitions of relevant parameters and corresponding equations are mentioned. Figure is inspired by [7] and created with BioRender.

Acoustic radiation force

The loss of acoustic energy due to absorption and scattering of ultrasound waves corresponds to a loss of momentum of the soundwave, which is transferred to the tissue [28, 131, 138, 139]. This will generate a force in the direction of the ultrasound wave which can be strong enough to cause tissue displacement, acoustic streaming, shear stresses, push microbubbles (MBs) and nanoparticles towards the blood vessel wall and improve NP penetration in tumour tissue [131, 135, 138].

Cavitation

The formation, growth and collapse of bubbles induced by ultrasound waves is referred to as cavitation [28]. Formation of bubbles can occur when the local pressure drops until the vapor pressure of the medium is reached, and a bubble is formed. Bubbles can also be introduced to the system in the form of ultrasound contrast agents. In the presence of an ultrasound field, microbubbles will expand at low pressure and contract at high pressures, which is referred to as oscillations.

At low acoustic pressure amplitudes, these oscillations will be symmetric and linear. Increasing the acoustic pressure amplitudes will result in non-linear behaviour of the microbubble which shows itself as more expansion than compression of the microbubble. Oscillations of microbubbles will result in microstreaming patterns with properties proportional to the oscillation amplitude. Even higher acoustic pressure amplitudes will force microbubbles to oscillate until they collapse. Acoustic pressure amplitudes insufficient to cause collapse of microbubbles is referred to as stable or non-inertial cavitation whereas microbubble oscillations resulting in collapse is referred to inertial cavitation (**Figure 9**) [136, 140, 141]. In case of the latter, the collapsing microbubbles will generate broad band acoustic emission and can cause shock waves and microjets when close to a rigid boundary [131, 136, 141, 142]. The thresholds at which the different type of microbubble oscillations appear depend on type of microbubble (e.g. initial size, shell type, composition) and environmental conditions [131, 139, 141].

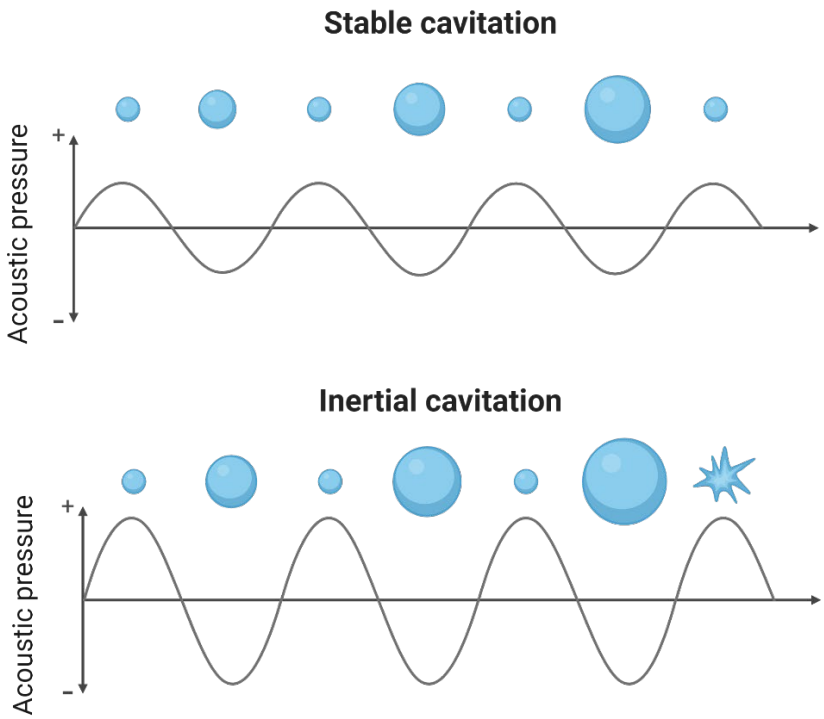

Figure 9. Graphical illustration of cavitation behaviour of microbubbles in the presence of an ultrasound field. Figure inspired by [1, 9] and created with BioRender.

1.4.2 Microbubbles

Currently, conventional ultrasound contrast agents are used for pre-clinical and experimental clinical ultrasound and microbubble treatments. The microbubbles differ in type of shell (e.g. lipid, protein, polymeric, etc.) or gas core (e.g. perfluorocarbon, nitrogen, etc.) and have a size within a range of 1-10 µm which allows them to smoothly flow through the vasculature [136]. Each of these attributes will impact the oscillation behaviour of the microbubble and thus its therapeutic potential.

The currently used microbubbles are primarily designed and optimized for diagnostic purposes. These microbubbles flow, due to their small size, freely through the vasculature and achieve only limited contact with the vessel wall, making them less optimal for therapeutic applications. To overcome their short comings, new microbubble platforms specifically engineered for therapeutic purposes are developed with the aim to improve the efficiency of ultrasound-mediated drug delivery.

1.4.3 Enhanced drug delivery by ultrasound and microbubble treatment

Several preclinical studies have demonstrated the potential of ultrasound and microbubble treatment to improve drug delivery to tumours and the brain [29-32]. The mechanisms behind ultrasound-mediated drug delivery are still not fully elucidated, but various biophysical effects induced by ultrasound and microbubble treatment have been identified and will be briefly discussed in the following section.

Sonoporation

The formation of transient pores in the cell membrane by oscillating microbubbles is referred to as sonoporation [1, 143, 144]. Sonoporation modifies the permeability of the cell plasma membrane such that it facilitates intracellular delivery of drugs and nanoparticles [144, 145]. Oscillating microbubbles can induce pores in the endothelial cell membrane in various ways (**Figure 10A**). Stable oscillating microbubbles can push and pull (**Figure 10A-i**) on the cell membrane during the expansion and contraction phase, respectively. In addition, oscillating microbubbles will induce streaming of fluid (microstreaming, **Figure 10A-ii**) around the microbubble, thereby exerting shear stresses on the cell membrane which can result in rupture of the cell membrane. Acoustic radiation

force may push oscillating microbubbles to and even through the cell membrane to enter cell, thereby rupturing the membrane (**Figure 10A-iii**). Higher acoustic intensities may result in more inertial cavitation, causing microbubbles to collapse. If this happens in the vicinity of the cell membrane, collapsing microbubbles may produce jet streams towards the cell plasma membrane thereby creating pores (**Figure 10A-iv**). Collapsing of a microbubble not in close proximity of an endothelial cell can still cause shear stresses such that the cell membrane ruptures (**Figure 10A-v**). Besides these mechanical forces, other phenomena such as the generation of reactive oxygen species (ROS) may also play an important role in transiently increasing the permeability of cell membranes [146-148].

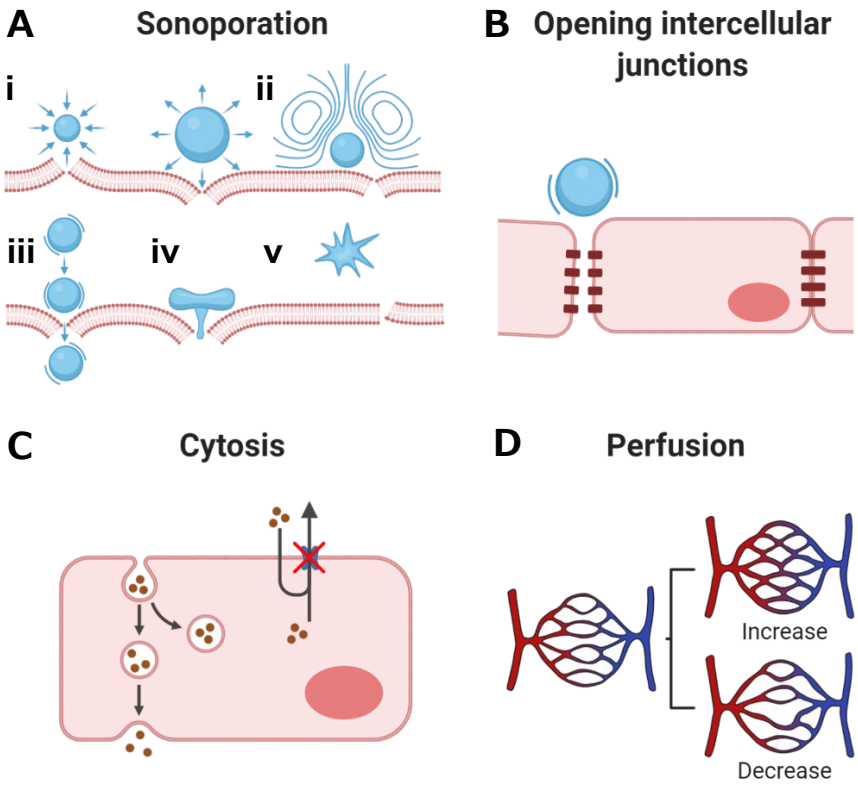

Figure 10. Graphical illustration of a selection of the currently known biophysical effects induced by ultrasound and microbubble treatment. (A) Oscillating microbubbles may induce pores in the cell plasma membrane in various ways (sonoporation), but also (B) open intercellular junctions. Furthermore, it has been demonstrated that cavitating microbubbles stimulate (C) cytosis and may impact the (D) perfusion in tissue. Figure inspired by [1, 2] and created with BioRender.

Opening of intercellular junctions

Oscillating and collapsing microbubbles will exert biomechanical forces on the endothelial cell which will be enough to open the intercellular junctions between endothelial cells (**Figure 10B**). This is particularly of interest in case of drug delivery across the BBB since the BBB consists of endothelial cells linked together by tight junctions. Several researchers have reported on the opening of these tight junctions upon ultrasound and microbubble treatments [149, 150].

Cytosis

Cytosis refers to the transport mechanisms into and out of the cell and comprises endocytosis, exocytosis and transcytosis. Increased incidence of endocytosis, transcytosis and exocytosis upon ultrasound and microbubble treatment has been observed (**Figure 10C**) [1, 150-156]. In addition, it has been demonstrated that upon ultrasound and microbubble treatment, the expression of ABC transporters such as the P-gp transporter was down-regulated in brain endothelial cells, implying reduced exocytosis of internalized drugs [157, 158]. Even though evidence of stimulated cytosis is restricted to *in vitro* experiments, it is believed that stimulated endocytosis, transcytosis and/or exocytosis following ultrasound and microbubble treatment occurs *in vivo* as well [1, 151].

Perfusion

Cavitating microbubbles may induce more macroscopical changes to tissue such as altering the perfusion (**Figure 10D**). Depending on the type of ultrasound exposure applied and timepoint of observation, a reduction or increase in perfusion have been observed upon ultrasound and microbubble treatments. This may be achieved by changes in blood flow, opening of collapsed blood vessels, vasoconstriction and vascular shutdown. These effects have been observed in both tumours and the brain following ultrasound and microbubble treatment [159-163].

Other ultrasound and microbubble induced responses

Inflammatory response

A slightly understudied ultrasound and microbubble induced effect is an inflammatory response in the tumour. The induced micro cell damages and/or micro haemorrhages are likely to stimulate immune cells thereby inducing an immune response. Other immune cells such as neutrophils and macrophages will be recruited to the site of inflammation and will remove cell debris and facilitate cell and tissue recovery processes. This could potentially result in a modest anti-

tumour immune response which also has been observed during HIFU treatments [164, 165]. Recruitment of immune cells such as macrophages to the tumour site could also have consequences for drugs and drug carriers since there will be an increased chance of being phagocytosed.

Cell death

Oscillating microbubbles have been observed to induce cell death (apoptosis) by forming large membrane disruptions resulting in complete lysis of the cell [144]. Additionally, creating of pores in the cell membrane may result in influx of Ca^{2+} ions which can trigger apoptosis. Cells can undergo the same fate if exposed to free radicals and reactive oxygen species generated by oscillating microbubbles [166, 167].

1.4.4 Ultrasound and microbubble treatment in the clinic

In several preclinical studies, ultrasound and microbubble treatments have shown their great potential in improving drug delivery to tumours and across the BBB, often resulting in increased therapeutic efficacy [29-32]. The promising preclinical results in various tumour and disease models have resulted in the initiation of several clinical studies.

One example is the first in man trial performed by Dimcevski et al. in which SonoVue™ microbubbles in combination with the chemotherapeutic agent gemcitabine resulted in extended survival and no additional toxic side effects in patients suffering from pancreatic cancer [168]. Similar studies are initiated to improve ultrasound-enhanced drug delivery in patients suffering of pancreatic ductal adenocarcinoma (NCT0416441), breast cancer (NCT03385200) and liver metastasis originating from primary breast, colon or pancreatic cancer (NCT03477019, NCT03458975, NCT04021277).

Besides improving drug delivery to tumours, microbubbles and ultrasound have also shown to improve the therapeutic sensitivity of tumour cells to ionizing radiation treatment [169]. Several clinical studies have therefore been initiated to study the enhanced ultrasound induced radiation treatment effect in patients suffering of breast cancers, head and neck cancer, and liver cancer (NCT04431674, NCT04431648, NCT03199274).

Additionally, several clinical trials focusing on improved drug delivery across the BBB have been initiated. The largest part of these studies is focusing on patients suffering of brain cancer (NCT04528680, NCT04440358, NCT04417088, NCT04063514). However, ultrasound-induced BBB disruption is also studied in

Alzheimer's patients. Besides assessing the safety and feasibility of ultrasound-induced BBB disruption, the effect on amyloid protein levels in the treated brain areas and cognitive function of Alzheimer's patients is studied (NCT04118764, NCT03119961).

Chapter 2 – Nanoparticles and microbubble platforms employed

In the work presented in this thesis, several nanoparticle-based drug delivery platforms and microbubble platforms have been used and combined to improve drug delivery to either tumour tissue or the brain. A brief description of the three main nanoparticles studied and the motivation behind using them is given in **section 2.1**. In **section 2.2** the two types of microbubble platforms used to achieve improved drug delivery are briefly discussed.

2.1 Nanoparticles

A graphical illustration of the three nanoparticle-based drug delivery systems used in this thesis is shown in **Figure 11**. Details on the liposomes used as controls and how to fabricate the different nanoparticle-based drug delivery systems can be found in the corresponding papers.

2.1.1 Enzyme sensitive liposomes

Liposomes are the most common and studied nanosized drug carrier and already found their way to the clinic. These spherical vesicles consist of one or more lipid bilayers which enclose an aqueous core. Liposomes have the unique ability to entrap both hydrophilic and hydrophobic molecules. The former can be dissolved in the core of the liposomes while the latter can be incorporated in the lipid bilayer itself. Liposomes offer several other advantages over other nanoparticle-based drug delivery systems such as biocompatibility, biodegradability, versatility, stability and ability to carry a large payload [170]. These properties have made liposomes popular drug carriers.

In **Paper I**, we employed enzyme sensitive liposomes, more specifically, matrix metalloproteinase (MMP) sensitive liposomes, and delivered these to the tumour site by ultrasound and microbubble treatment [171]. Many of the nanoparticles developed these days are coated with polyethylene glycol (PEG) which shields nanoparticles from the immune system and thereby extends their circulation half-life significantly [36]. Even though this is a beneficial feature, the PEG coat affects the nanoparticle-cell interactions and is known to reduce internalization and thus therapeutic efficacy of nanoparticles [77, 172, 173]. To improve therapeutic outcome, the enzyme sensitive liposomes used in **Paper I** were coated with PEG-polymers containing a cleavable lipopeptide. After ultrasound-mediated delivery to the interstitial space of the tumour, the PEG-layer will be cleaved by two members of the enzyme MMP family (MMP-2 and MMP-9) which are overexpressed in several cancer types [174]. Cleaving of the PEG-layer is expected to improve interaction between cells and drug-loaded nanoparticles, and to accelerate drug release. It was therefore hypothesized that this combination would enhance therapeutic efficacy of the MMP-sensitive liposomes opposed to its non-MMP sensitive version.

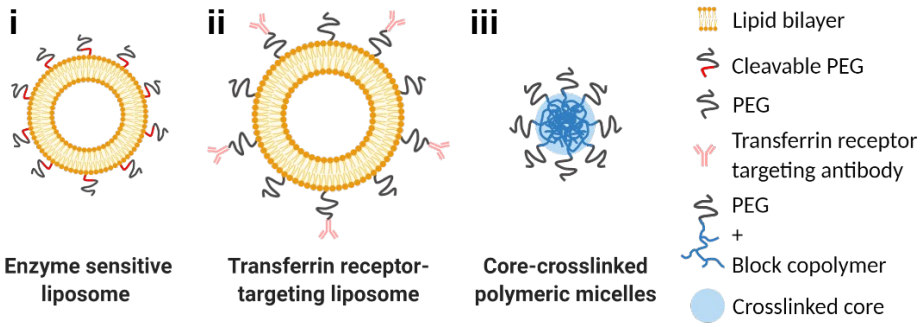

Figure 11. Graphical illustrations of the (i) enzyme sensitive liposome, (ii) transferrin receptor-targeting liposome and (iii) core-crosslinked polymeric micelles. Depending on the study conducted, the nanoparticles were labelled with fluorophores and/or loaded with drugs. Figure created with BioRender.

2.1.2 Transferrin receptor-targeting liposomes

In **Paper II** we again used a liposomal-based drug nanocarrier but this time the liposomes were decorated with a ligand targeting the transferrin receptor on the plasma membrane of brain capillary endothelial cells (BCECs). The BCECs are part of the blood-brain barrier (BBB) which tightly regulates transport across the BBB and thereby impedes the access of most drugs. Many drug delivery systems try

to employ transport mechanisms already present on the BBB, such as receptor mediated endocytosis, to get drugs across the BBB. Of the receptors on the BBB, the transferrin receptor has received special interest since its expression is restricted to only the brain capillary endothelial cells compared to other endothelial cells. In **Paper II** we used liposomes targeting this receptor in combination with disruption of the BBB by focused ultrasound and microbubbles. The latter has shown to transiently and safely increase the permeability of the BBB thereby also enhancing endocytosis. By using a transferrin receptor-targeting liposome combined with ultrasound-induced permeability of the BBB it was hypothesised that this combined approach could improve delivery across the BBB.

2.1.3 Core-crosslinked polymeric micelles

Core-crosslinked polymeric micelles (CCPM) have emerged as a promising nanoparticle-based drug delivery platform. The CCPM used in **Paper III** were kindly provided by Cristal Therapeutics (Maastricht, The Netherlands) and consist of highly tuneable polymers and biodegradable drug linkers. The therapeutic agent of interest can be easily incorporated, generating a wide range of possible applications [175, 176]. In several preclinical studies [73, 177, 178], the CCPM have shown great tumour accumulation and therapeutic potential which has also resulted in the initiation of a phase II clinical trial (CPC634). Even though the CCPM show great accumulation behaviour and therapeutic efficacy in tumours, delivery across the BBB is dissatisfying due to the BBB impeding access of almost all substances. In **Paper III** we therefore combined the use of CCPM with ultrasound-induced increase of the BBB permeability, which could improve delivery of the CCPM across the BBB thereby generating a new range of therapeutic applications of these clinically promising tuneable drug nanocarriers.

2.2 Microbubble platforms

Two different microbubble platforms for drug delivery have been employed in the work presented in this thesis and will be briefly discussed in the following section.

2.2.1 SonoVue™ microbubbles

SonoVue™ microbubbles (Bracco Imaging, Italy) have a lipid shell and contain the gas sulphur hexafluoride (SF_6). The mean bubble diameter is 2.5 µm and upon systemic administration, the microbubbles have a circulation half-life time of 1-2 minutes. The bubble concentration of SonoVue™ is within the range 100-500 million microbubbles per ml [179]. In the studies presented in **Paper I-II and IV**, administration volumes in rodents were typically between 25 and 100 µl. The cavitation behaviour of SonoVue™ microbubbles is well characterized and these microbubbles have also shown their therapeutic potential in both preclinical and clinical studies [30, 168, 180, 181].

2.2.2 Acoustic Cluster Therapy®

Acoustic Cluster Therapy® (ACT) is an example of a novel microbubble platform specifically engineered for drug delivery applications [182]. The ACT formulation consists of clusters formed by negatively charged lipid-shelled microbubbles (Sonazoid™) which contain the gas perfluorobutane (C_4F_{10}) and positively charged microdroplets consisting perfluoromethylcyclopentane (C_6F_{12}) stabilised with a lipid membrane. The suspension contains approximately $1.2x10^8$ of these clusters which have a median diameter of approximately 5 µm [182].

A graphical illustration of the ACT concept is shown in **Figure 12**. Upon intravenous co-injection with the therapeutic agent, a population of the clusters are activated within the target pathology by high frequency ultrasound (2.0-3.0 MHz) at relatively low intensity (MI of 0.2-0.4). The oscillating microbubble part of the ACT-clusters will induce vaporization of the microdroplet, resulting in a large microbubble (20-30 µm) which will transiently lodge in the microvasculature. Applying a second insonation step with low frequency (0.5 MHz) and low intensity (<0.2 MI) will induce controlled volume oscillation of the large ACT bubble, thereby exerting biomechanical forces on the capillary wall and enhancing drug delivery locally. Due to their large size, ACT bubbles will cover a large area within the blood vessel, have closer contact with the endothelium and stay for prolonged time (5-10 minutes) [182]. Due to these attributes, it is

hypothesized that ACT applies a higher magnitude of biomechanical work on the capillary wall opposed to conventionally used microbubbles.

Several pre-clinical studies in different cancer models have demonstrated the improved therapeutic efficacy when combining ACT with chemotherapeutic agents [183-186]. The promising pre-clinical results have resulted in the initialization of the first in man study to evaluate the efficacy of ACT (phase I ACTIVATE study, NCT04021277). However, the use of the ACT principle to improve delivery to the brain is understudied, but could, in case of positive results, generate new therapeutic applications. The potential of ACT to increase the permeability of the BBB and enhance delivery of clinically relevant nanoparticles was therefore studied in **Paper III**.

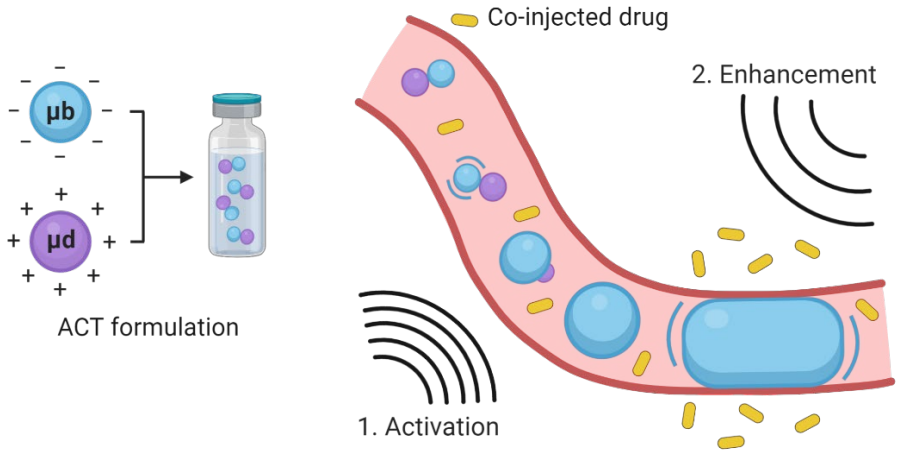

Figure 12. Graphical illustration of the ACT concept. ACT clusters are formed by mixing microbubbles (μm) with microdroplets (μd). Upon intravenous injection, the target site is first exposed to high frequency ultrasound which induces vaporization of the microdroplet, creating a large ACT-bubble which will lodge in the vasculature. Thereafter, low frequency ultrasound is applied which lets the microbubble oscillate facilitating delivery of the co-injected drug into the tumour tissue or across the BBB. Figure created with BioRender.

Chapter 3 – Objectives

The overall aim of the work presented in this thesis was to study the effect of different types of nanoparticles and microbubble platforms on nanoparticle delivery to tumours and the brain. In addition, an intravital microscopy set-up to perform ultrasound and microbubble treatment in the brain simultaneously with multiphoton microscopy has been established and described.

Besides obtaining knowledge which will contribute to the general understanding of enhanced drug delivery upon ultrasound and microbubble treatment, the following more specific aims can be defined:

- To know whether liposomes with enzymatic cleavable poly(ethylene) glycol layer combined with ultrasound and microbubble treatment improve tumour accumulation, microdistribution and therapeutic efficacy of the liposomes.
- To determine the effect of different acoustic pressures on the delivery of liposomes to tumour tissue.
- To know whether targeting of liposomes to the blood-brain barrier combined with ultrasound and microbubble treatment improves delivery of the liposomes across the blood-brain barrier.
- To exploit the novel microbubble platform Acoustic Cluster Therapy® to increase the permeability of the blood-brain barrier and enhance delivery of the clinically promising tuneable core-crosslinked polymeric micelles to the brain.
- To establish an intravital microscopy set-up which facilitates performing ultrasound and microbubble treatments in the brain simultaneously with multiphoton microscopy.

Chapter 4 – Summary of papers

This thesis comprises four papers and ultrasound and microbubble treatment plays an important role in each of them. In **Paper I**, focused ultrasound and microbubbles were used to improve the delivery and therapeutic efficacy of enzyme sensitive liposomes in a prostate cancer xenograft model. In **Paper II**, focused ultrasound and microbubble treatment was employed to increase the permeability of the blood-brain barrier (BBB) and improve delivery of transferrin receptor targeting liposomes. In **Paper III** a novel microbubble drug delivery platform was used to increase the permeability of the blood-brain barrier and facilitate delivery of a clinically staged nanoparticle. Lastly, **Paper IV** describes an intravital microscopy procedure which makes it possible to perform multiphoton microscopy imaging simultaneously with ultrasound and microbubble treatment in the murine brain.

Paper I

To improve the therapeutic efficacy of nanoparticle-based drug delivery systems, it is essential to improve their accumulation and penetration in tumour tissue, enhance cellular uptake and ensure efficient drug release at the tumour site. Commonly used nanoparticles are often coated with poly(ethylene) glycol (PEG) to shield them from the immune system. This may extend their circulation half-life time significantly compared to non-PEGylated nanoparticles and small drug molecules, which may increase accumulation at the tumour site. Additionally, the PEG-layer prevents aggregation of the nanoparticles and may have a charge shielding effect. The latter may improve penetration through the extracellular matrix due to reduced electrostatic interactions with extracellular components. However, the presence of PEG on the surface of nanoparticles is known to affect nanoparticle-cell interaction, resulting in reduced cellular uptake and thereby potentially reducing their therapeutic potential.

In **Paper I** we therefore introduced an enzyme sensitive liposome which is coated with cleavable PEG. Cleavage of the PEG-layer by two members of the enzyme matrix metalloproteinase (MMP) family may improve interstitial transport, could destabilize the liposomal membrane which may result in accelerated drug release

and increased cellular uptake. The main aim of the work presented in **Paper I** was to study the effect of focused ultrasound and microbubbles on the delivery and therapeutic efficacy of the MMP sensitive liposome. The performance of the MMP sensitive liposome was compared to a non-MMP sensitive version and a liposomal formulation similar to the commercially available Doxil® formulation. The cellular uptake and cytotoxicity of the liposomes were studied *in vitro*. *In vivo* the effect of focused ultrasound and microbubbles on tumour accumulation, biodistribution, microdistribution and therapeutic efficacy of the three types of liposomes were investigated. We concluded that for all liposomes, focused ultrasound and microbubbles treatment resulted in an improved tumour accumulation, increased extravasation, and increased penetration depth of the liposomes. The latter was surprisingly independent of the ultrasound intensity used. The MMP sensitive liposome showed a better therapeutic efficacy and improved penetration depth of the liposomes into the tumour interstitium compared to the non-MMP sensitive version. These results indicated that cleaving of the PEG-layer may have had a positive impact on the therapeutic efficacy. However, of all the liposomes studied, the Doxil-like liposome outcompeted the MMP and non-MMP sensitive liposome, both with and without the use of ultrasound and microbubble treatment.

Paper II

As previously discussed in this thesis, the blood-brain barrier is a major obstacle when treating several brain disorders. Focused ultrasound in combination with intravascular microbubbles has shown to increase the permeability of the BBB by opening the tight junctions, creating endothelial cell openings, stimulating endocytosis and increasing transcytosis. The main aim of the work presented in **Paper II** was to study if combining focused ultrasound and microbubbles with transferrin receptor-targeting liposomes would result in enhanced delivery across the BBB, compared to liposomes lacking the BBB targeting moiety.

As a model system, post-natal rats were used because of their high expression of the transferrin receptor on the BBB. Magnetic resonance image (MRI) guided focused ultrasound was employed to increase the permeability of the BBB in one of the hemispheres. The extend of BBB permeability was evaluated by contrast-enhanced MRI. The two liposomes studied were loaded with cisplatin and labelled with a fluorophore. The amount of cisplatin entering the brain tissue was quantitated by inductively-coupled plasma mass spectroscopy (ICP-MS). The distribution of liposomes in brain tissue was imaged by confocal laser scanning microscopy (CLSM).

For all animals, an increased BBB permeability was observed after focused ultrasound and microbubble treatment. A 40% increase in accumulation of the transferrin receptor targeting liposomes was detected in the hemisphere treated with focused ultrasound relative to the control hemisphere. The liposome lacking the BBB targeting moiety showed no increased accumulation in the focused ultrasound treated hemisphere. High magnification CLSM images showed that the liposomes in the ultrasound treated hemisphere were mainly located in the brain endothelial cells and/or perivascular space. The results presented in **Paper II** demonstrate that focused ultrasound and microbubble treatment combined with blood-brain barrier targeting liposomes could be an interesting approach to enhance drug delivery to the brain.

Paper III

The restrictive nature of the BBB prevents efficient treatment of many brain diseases. Focused ultrasound and microbubble treatment has shown to safely and transiently increase the permeability of the BBB. Currently, microbubbles primarily designed and optimized for diagnostic purposes are being employed. These microbubbles flow, due to their small size (1-3 μm), freely through the vasculature and achieve only limited contact with the vessel wall, making them less optimal for therapeutic applications. New microbubble platforms are currently developed to address these shortcomings and Acoustic Cluster Therapy® (ACT) is one of them. The ACT concept consists of an intravenous injection of microdroplet-microbubble clusters. By using high frequency ultrasound (2-3 MHz), these clusters are activated into large microbubbles (20-25 μm) which transiently lodge in a small fraction of the targeted vasculature. A second ultrasound exposure step with low frequency ultrasound (500 kHz) is expected to induce controlled volume oscillations of the ACT bubbles which thereby exert biomechanical forces on the capillary wall and enhance local accumulation of a co-injected therapeutic agent at the targeted site. The large ACT bubbles will cover a large area within the blood vessel and stay for a prolonged time resulting in intensified contact with the endothelium compared to conventional used microbubbles. In **Paper III** we studied the potential of ACT to increase the permeability of the BBB and improve accumulation of the model drug IRDye® 800CW-PEG and CCPM in the brain. One hour post treatment, we observed increased accumulation of the IRDye® 800CW-PEG (5.2-fold) and CCPM (3.7-fold) in the ACT treated brains opposed to control brains. CLSM verified the improved delivery of CCPM to the brain and showed increased extravasation and penetration depth of the CCPM upon ACT. No treatment related tissue damage

was observed in brain sections. With this study we demonstrated that ACT is capable to increase the permeability of the BBB safely and enhances accumulation and tissue distribution of macromolecules and clinically relevant nanoparticles in the brain.

Paper IV

Ultrasound exposure in the presence of microbubbles has emerged as an effective method to transiently and locally increase the permeability of the BBB, and thereby facilitating transport of drugs across. Successfulness of focused ultrasound and microbubble treatment is commonly evaluated by contrast-enhanced magnetic resonance imaging or by dye extravasation visualized with *in vivo* imaging or in *ex vivo* histology. However, most of these evaluation methods have been performed after completion of the focused ultrasound and microbubble treatment such that essential information on the dynamic biological responses during, and immediately following ultrasound exposure are missed. This kind of information may aid in understanding the mechanisms behind focused ultrasound and microbubble treatment.

Paper IV describes the surgical and technical procedures required to conduct *in vivo* multiphoton imaging with high spatial and temporal resolution imaging of the brain parenchyma during ultrasound and microbubble treatment. Optical access to the brain is obtained via an open-skull cranial window. A piece of skull with a diameter of 3-4 mm is removed and the exposed area of the brain is sealed with an optically transparent coverslip. For good ultrasound coupling and as support for the transducer, agarose is applied on top of the cranial window after which a ring-shaped transducer attached to a second coverslip is mounted on top. When this whole procedure is performed under sterile surgery procedures and if anti-inflammatory measures are taken, ultrasound and microbubble treatments and imaging sessions can even be performed for several weeks. To visualize the vasculature and to quantify ultrasound induced effects such as leakage kinetics and vascular changes, fluorescent dextran conjugates can be intravenously injected. In short, this paper describes the cranial window placement, ring transducer placement, imaging procedure, common troubleshooting steps as well as advantages and limitations of the procedure discussed.

Chapter 5 – Discussion and future outlook

The combined use of ultrasound and microbubbles has emerged as a new strategy to enhance drug delivery to tumours and across the blood-brain barrier (BBB). New nanoparticle-based drug delivery systems and microbubble platforms are continuously being developed to achieve more efficient drug delivery to tumours and the brain. The work presented in this thesis aims to contribute in this development.

The novelty in both **Paper I** and **Paper II** is the use of ultrasound and microbubble treatment combined with liposomes exhibiting features which may improve delivery to tumour cells (**Paper I**) or enhance drug delivery across the BBB (**Paper II**). In both cases ultrasound and microbubble treatment was performed with the commonly used ultrasound contrast agent SonoVue™. In **Paper III** the potential of the novel microbubble platform Acoustic Cluster Therapy® (ACT) to increase the permeability of the BBB and to facilitate delivery of a clinically relevant nanoparticle to the brain was studied. Lastly, **Paper IV** describes the surgical and technical procedures that enable real-time *in vivo* multiphoton fluorescence imaging of the rodent brain during focused ultrasound and microbubble treatments to increase the BBB permeability. Based on the procedures described in **Paper IV**, experiments on unravelling the mechanism behind ACT-induced increase of BBB permeability have been initiated. More data needs to be acquired, but interesting observations have already been made.

Nanoparticle delivery to tumours

Nanoparticle-based drug delivery systems have aroused attention because of their promising potential in increasing drug delivery to tumours due to their ability to exploit the EPR-effect. However, a thorough literature review summarizing data on nanoparticle uptake into tumours published during the last decade showed that only a small fraction of intravenously administered nanoparticles was recovered in tumours (median 0.7 %) [187]. Additionally, other research demonstrated that the majority of extravasated nanoparticles were trapped in the extracellular matrix or taken up by immune cells resulting in low delivery efficiency to tumour cells (0.0014%) [70]. For core-crosslinked polymeric micelles

(CCPM), the nanoparticles used in **Paper III**, approximately 66 % of internalized CCPM in tumour tissue were observed inside immune cells [73]. The poor delivery to tumours and low internalization efficiency by tumour cells represent the current challenges in achieving a sufficient therapeutic effect with nanoparticle-based drug delivery systems.

The main reason why drug loaded nanoparticles have evolved as an interesting way to increase drug delivery to tumour tissue is that they exploit the EPR-effect. Even though the EPR effect is the main paradigm in cancer nanomedicine, it has been questioned, mainly due to the limited success of nanomedicine in the clinic. However, recent research sheds new light on our knowledge on the transport pathways of nanoparticles into tumours. Whereas passive accumulation of nanomedicine has always been assumed to be the main transport pathway into tumours, recent research demonstrated that active transport of intravenous administered nanoparticles through endothelial cells into the tumour might be more dominant [57]. Other interesting research demonstrated a dose threshold for nanoparticle tumour delivery in mice [188]. Doses above the threshold of 1 trillion nanoparticles were found to overwhelm the clearance system. This enabled up to 12 % tumour delivery and at the largest number of injected nanoparticles, 93 % of the cells in the tumour had internalized nanoparticles [188]. The found threshold was translatable to different types of nanoparticles and several tumour models [188]. Even though the research presented above has received some critique [189], these recent findings indicate that instead of developing more complicated nanoparticle-based drug delivery systems, we ought to reassess our current perspective and knowledge on delivery and transport pathways of nanoparticles in tumours.

Ultrasound-mediated delivery of nanomedicine to tumours

As extensively discussed in **Chapter 1** in this thesis, ultrasound in combination with systemically administered microbubbles can improve delivery of drugs and drug carriers to tumour tissue [28-30, 130, 190-192]. Even though ultrasound enhanced delivery of drug carriers has been associated with enhanced therapeutic efficacy, extravasated drug carriers will potentially still face low internalization rates by tumour cells as discussed in the previous paragraph. This may reduce the real therapeutic potential of ultrasound and microbubble treatment. In **Paper I** we therefore combined ultrasound and microbubble treatment with liposomes exhibiting a feature beneficial for internalization by tumour cells upon extravasation. These liposomes were coated with an enzymatic cleavable poly(ethylene) glycol (PEG) layer. Upon delivery to the tumour site, the enzymes

MMP-2 and MMP-9 will cleave the PEG-layer which may facilitate internalization of the liposomes by the tumour cells and thus increase the therapeutic efficacy. The performance of the enzyme sensitive liposome was compared to its non-enzyme sensitive version and a liposome formulation similar to the clinically approved Doxil® formulation. For all three liposomes studied, ultrasound and microbubble treatment resulted in enhanced accumulation, improved extravasation, and increased penetration of the liposomes from the blood vessels into the tumour tissue. These findings agreed with what others have observed upon using ultrasound and microbubble treatment [28-30, 130, 190-192]. However, in addition, we demonstrated that ultrasound-mediated delivery of the enzyme sensitive liposome indeed resulted in improved therapeutic efficacy whereas the therapeutic efficacy of the non-enzyme sensitive liposome did not improve upon ultrasound and microbubble treatment. These findings could indicate that the enzymatic feature of the liposome might have contributed to the observed enhanced therapeutic efficacy.

If the observed enhanced therapeutic efficacy can be completely assigned to the enzyme sensitive attribute of the liposome is of course disputable. Firstly, in the presented work, the positive effect of cleavage of the PEG-layer on internalization by tumour cells has been studied solely *in vitro*. Assumptions on *in vivo* behaviour are based on the verified presence of the enzymes MMP-2 and MMP-9 and not on their demonstrated *in vivo* activity. Acquiring information on if, where, how long and at what incidence cleavage of the liposomes takes place *in vivo* is a highly challenging task. Demonstrating the *in vivo* presence of the enzymes of interest combined with *in vitro* activity has therefore currently been the standard for assumptions on *in vivo* behaviour [193]. Secondly, small differences in liposomal characteristics (e.g. size, surface charge, etc.) were observed between the two liposomes with similar lipid composition. The differences were within an acceptable range, but it is unknown if and to what extent these differences might have affected the *in vivo* behaviour of the liposomes. Additionally, upon systemic administration, liposomal characteristics may be altered due to interactions with blood components or by being exposed to different environmental conditions (e.g. osmolarity, pH, temperature). Our knowledge on what happens to the drug delivery system upon administration is limited due to the complexity of the biological system. *In vitro* obtained characterization data is therefore used to interpret *in vivo* behaviour of nanoparticles which could easily result in drawing the wrong conclusions and makes it difficult to compare the performances of different nanoparticle-based drug delivery systems. Unravelling of the *in vivo* characteristics and behaviour of the nanoparticle-based drug delivery systems will

be challenging, but it will most likely help us forward in developing better drug delivery systems.

The enhanced therapeutic effect observed upon ultrasound and microbubble treatment is often explained by the improved delivery and tumour penetration of the drug carrier due to increased tumour vasculature permeability, and sonoporation facilitating intracellular drug delivery. Direct comparison of studies on ultrasound-mediated delivery is challenging due to the many parameters (e.g. nanoparticle type, tumour model, ultrasound settings, etc.) involved. Nevertheless, when ignoring experimental differences, an ultrasound-induced increase in drug carrier delivery in the range of 2 to 12-fold with variable therapeutic efficacies including complete tumour regression as result has been reported [171, 186, 190, 191, 194, 195]. Although increased intracellular concentrations of drugs are observed upon ultrasound and microbubble treatments [1, 196, 197], it is surprising that the 'modest' increase in tumour accumulation of the drug carrier can result in an impressive therapeutic efficacy such as complete tumour regression. Especially when taking into account the high numbers on internalization of drug carriers by immune cells and relatively low delivery efficiency to tumour cells presented previously. The focus in ultrasound mediated drug delivery is often on biomechanical effects such as creating pores, opening intracellular junctions and microstreaming, resulting in improved delivery of the drug carrier which is often quantified and given as the reason for the observed enhanced therapeutic efficacy. However, each of the ultrasound-induced effects and cavitating microbubbles by themselves will induce responses on a cell biological level which, in the end, will be the main determinant for the fate of the cells affected, and thus might be interesting to understand and study. Examples of biological effects which currently have been observed upon ultrasound and microbubble treatment are stimulated cytosis processes, apoptosis and altered gene expressions [1, 153, 166, 198]. Inducing these biological effects may be therapeutically beneficially. It for example has been reported that induced effects by ultrasound and microbubble treatment improved the tumour response to radiation treatment [199-201]. The observed effect was explained by ultrasound and microbubble induced endothelial cell apoptosis which was enhanced by ionizing radiation treatment, leading to reduction of blood flow and the induction of tumour cell death [200]. Besides (indirectly) reducing the blood flow in tumours [162, 163], the opposite has also been observed upon ultrasound and microbubble treatment [160]. The latter effect may be therapeutically beneficial as well since it might increase the oxygenation level in hypoxic areas of the tumour. These hypoxic areas are often associated with

treatment resistance and local increase in oxygenation level by ultrasound and microbubble treatment might make tumour cells more susceptible to chemotherapeutic agents and radiation therapy [169, 202].

Another slightly underappreciated ultrasound induced effect which will contribute to the therapeutic efficacy of the treatment and should be studied and exploited more, is the anti-tumour immune response. In case of high intensity focused ultrasound (HIFU) treatments, anti-tumour responses have been reported and held responsible for the complete tumour regression observed in animal tumour models [164, 165]. Also in case of ultrasound and microbubble treatment, an induced anti-tumour response has been reported [203] so its occurrence is therefore not unlikely. This may be explained by the micro cell damages and/or micro haemorrhages induced by cavitating microbubbles, which stimulate immune cells and thus induce an immune response. Besides improving delivery of nanomedicine by cavitating microbubbles, inducing small haemorrhages in the tumour could intensify the immune response and could thus be favourable in case of therapeutic purposes. Combined with what has been discussed in the previous paragraph, ultrasound and microbubble treatment could on purpose be used to reduce the vasculature in tumours. The induced tissue damage will most likely show similarities with a regular blue mark, but since tissue damage is currently often reported as an unwanted side effect of ultrasound and microbubble treatment, the therapeutic potential of inducing modest tissue damage and its long term consequences on tumour growth are understudied.

Improving drug delivery across the blood-brain barrier

Whereas **Paper I** focuses on the use of ultrasound and microbubble treatment to enhance drug delivery to tumour tissue, in **Paper II**, **Paper III** and **Paper IV** ultrasound and microbubble treatment is employed to increase the permeability of the BBB. In **Paper II** ultrasound and microbubble treatment was combined with a liposome decorated with an antibody directed against the BBB to improve delivery across the BBB. Ultrasound and microbubble treatment is known to stimulate different cytosis processes such as endocytosis and transcytosis [111, 150, 204]. It was therefore hypothesized that combining ultrasound and microbubble treatment with a liposome that can exploit endogenous BBB transport pathways (e.g. receptor-mediated transcytosis) would result in an increased delivery of liposomes across the BBB. The performance of the transferrin receptor-targeting liposome (Anti-TfR) was compared to a liposome decorated with an isotype of the Anti-TfR antibody (e.g. IgG) which thus lacked the BBB targeting moiety. Both liposomes were loaded with cisplatin and labelled

with a fluorophore to study the brain accumulation by ICP-MS and distribution of the liposome in the brain by CLSM, respectively. The main finding of the work presented in **Paper II** was the 40% increase in cisplatin accumulation in the FUS-treated hemisphere opposed to the control hemisphere in animals receiving the Anti-TfR liposome while no increased accumulation was observed in animals treated with the IgG liposome. CLSM tilescans of brain sections showed that the location of liposomal fluorescence corresponded with the observed gadolinium-induced contrast in the corresponding MR image acquired post ultrasound and microbubble treatment. High magnification CLSM imaging revealed that liposomes in the ultrasound treated hemisphere were mainly observed in endothelial cells and/or perivascular space. Only a small number of liposomes was observed in the brain parenchyma. Based on our findings, we concluded that combining focused ultrasound and microbubble treatment with a BBB-targeting liposome enhanced their accumulation in the brain.

Since ultrasound-mediated delivery of a drug carrier is often associated with extravasation and improved penetration depth within the ultrasound targeted tissue, as for example observed in **Paper I**, it was surprising that we only observed a minimal amount of liposomal fluorescence in the brain parenchyma (**Paper II**). The absence of liposomal fluorescence in the brain parenchyma could imply that the FUS treatment employed did not create openings and/or pores large enough to facilitate free access for the 180 nm sized liposomes to the brain parenchyma. In case extravasation of the liposomes did occur, the large size of the liposomes (~180 nm) may hamper its diffusion into the brain parenchyma [51]. The relatively low acoustic pressure (0.26 MPa) used and corresponding mechanical index (0.25) is far below the threshold for irreversible BBB disruption (0.46 MI) [119]. The latter is mainly associated with inertial cavitation behaviour of microbubbles causing microvascular damage. It is therefore expected that the SonoVue™ microbubbles mainly exhibited stable cavitation behaviour which has been associated with opening of the inter-endothelial tight junctions. The increase in blood-brain permeability was verified with contrast enhanced MRI which indicated clear extravasation of the gadolinium containing MR contrast agent. Different studies have been performed to investigate the size of the openings and/or pores in the BBB induced by ultrasound and microbubble treatment [205, 206] and the optimum size for drug carriers exploited for ultrasound-mediated delivery to the brain [207, 208]. These studies demonstrated that the size of ultrasound-induced openings in the BBB depends on several parameters such as microbubble characteristics (e.g. type, size), microbubble concentration and ultrasound parameters (e.g. acoustic pressure, pulse length) [206, 209-211].

Based on these studies, a size limit for extravasating macromolecules upon ultrasound and microbubble treatment was suggested whereby higher acoustic pressures facilitated the delivery of larger macromolecules across the BBB [206]. With acoustic pressures higher than employed in **Paper II**, a maximum size of inter-endothelial cell openings of around 65 nm was observed. Even though it has been suggested that by optimizing ultrasound settings, inter-endothelial cell openings larger than 65 nm can be generated, it seems to be unlikely that pores and/or openings large enough to facilitate free access of the liposomes (~180 nm) to the brain parenchyma were acquired with the low acoustic pressures used in **Paper II**. The enhanced accumulation of the transferrin receptor-targeting liposomes observed in the ultrasound treated hemisphere can therefore be most likely assigned to ultrasound enhanced endocytosis and/or transcytosis.

The fact that only a minimal amount of liposomal fluorescence was observed in the brain parenchyma does not specifically mean that the delivery of the payload (e.g. cisplatin) to the abluminal side was unsuccessful. Unfortunately, the exact location of the cisplatin is unknown. The fate of the cisplatin, located in the core of the liposome, will depend on the intracellular sorting upon receptor mediated endocytosis. The exact mechanism is still unknown, but the binding affinity of the antibody towards the transferrin receptor is one of the determining factors [212]. Interestingly, recent research with the same liposomes as used in **Paper II** but without the use of ultrasound and microbubble treatment demonstrated that upon transcytosis, the liposomes accumulated in the perivascular space and did not extravasate into the brain parenchyma [213].

Ultrasound induced effects in tumour and brain tissue

The conventional ultrasound contrast agent SonoVue™ was employed in **Paper I** to improve delivery of the enzyme sensitive liposomes to subcutaneous tumour tissue and in **Paper II** to enhance the delivery of transferrin receptor targeting liposomes to a healthy rat pup brain. To achieve improved delivery in the different tissue types, different ultrasound pressures were applied. That different targeted tissues demand different ultrasound pressures to achieve improved delivery of nanomedicine is not surprising since ultrasound and microbubbles will interact differently with the different types of tissue. As discussed in **Chapter 1**, tumour tissue differs in various ways from healthy tissue. Firstly, the tumour vasculature is highly abnormal. It has an atypical architecture, contains dead ends, has high vascular resistance, is unusually branched and is leaky due to poorly aligned endothelial cells resulting in large fenestrations. Secondly, the high cell density and dense extra cellular matrix may result in stiffer tissue compared to healthy

tissue. Lasty, the poorly functioning vasculature combined with a defective lymphatic system and dense extra cellular matrix results in a high interstitial fluid pressure [62]. The aforementioned tissue properties are known to not only differ highly within and between tumours but also between cancer types [54, 59]. Whereas tumour tissue has a leaky and poorly functional vasculature, the blood-brain barrier is quite the opposite. Brain capillaries are aligned with endothelial cells which are strongly bound together by tight junctions sealing the paracellular cleft and restricting paracellular transport. In addition, brain tissue is relatively 'soft' compared to other tissues since it only contains a minimal amount of connective tissue [214]. The properties of tumour tissue and brain tissue are clearly different such that biophysical effects induced by oscillating microbubbles and their impact will vary as well. The leaky tumour vasculature will to some extent already facilitate the extravasation of nanomedicine. To really improve delivery and penetration further into the slightly stiff tumour tissue with high interstitial pressure, the impact of the oscillating microbubbles needs to preferably reach beyond the endothelial cell layer. By using higher pressures, the microbubble oscillations will, to some extent, be more forcefully thereby inducing biophysical effects facilitating extravasation and penetration of the co-injected drug or drug carrier. However, in case of brain tissue, the main purpose of using ultrasound and microbubble treatment is to increase the permeability of the blood-brain barrier since this is the main barrier to overcome in case of drug delivery to the brain. To open the tight junctions, oscillating microbubbles mainly need to interact with the endothelial cell layer. To not permanently damage the brain, this should preferably be done in a safe and temporarily manner such that as low as possible pressures should be used. In case of tumour tissue, too much tissue damage should be prevented as well, but this is a less crucial prerequisite compared to brain tissue.

The anatomical differences between tissue types and the variety in other experimental details (e.g. ultrasound settings, type of microbubble, microbubble concentration, etc.) will affect the *in vivo* behaviour of the microbubble and thus the efficiency of the ultrasound and microbubble treatment. By monitoring the *in vivo* behaviour of the microbubbles, the reproducibility and efficiency of the treatment could potentially be improved. This can be achieved by detecting the acoustic emission of the microbubbles and including a feedback controller mechanism such that the pressures can be adapted based on the observed *in vivo* behaviour of the microbubbles. Several research groups started exploring the use of such a cavitation detection system to improve the efficiency of their ultrasound and microbubble treatment as well as high intensity focused ultrasound (HIFU)

treatments [215-217]. A cavitation detection system was part of the experimental set-up in **Paper I** but was mainly used to study if there would be a correlation between the acoustic emission of the microbubbles and the obtained therapeutic efficacy, but no correlation was found. The commercial ultrasound set-up employed in **Paper II** contains a cavitation detection system and feedback controller mechanism, but unfortunately this system was defective. Variations in the increase in blood-brain barrier permeability and thus delivery of the transferrin receptor targeting liposomes were observed between the different treatment spots which was most likely caused by differences in thickness and curvature of the skull at the different treatment locations. A feedback controller mechanism could have been of great help to improve the efficiency of the ultrasound and microbubble treatment employed in **Paper II**.

Microbubbles for therapeutic applications

Microbubbles (e.g. SonoVue™, Optison™, Definity™) currently used in most ultrasound and microbubble treatment studies are primarily designed and optimized for diagnostic purposes. These microbubbles flow, due to their small size, freely through the vasculature, stay confined in the vascular lumen and have only limited contact with the vessel wall. In addition, these microbubbles are typically cleared within 2-3 minutes from the vasculature and are easily destroyed by ultrasound such that often multiple injections are needed to achieve efficient treatment. To overcome their short comings, new microbubble platforms specifically engineered for therapeutic purposes with the aim to improve the efficiency of ultrasound-mediated drug delivery are being developed.

Examples of optimal properties of therapeutic microbubbles to improve the efficiency of ultrasound-mediated drug delivery are an increased size to optimize contact with endothelial cells and a long circulation time to prolong treatment time. As already discussed, ACT is an example of a therapeutic microbubble platform which exhibits these properties. Another approach to improve treatment efficiency is to use microbubbles with a narrow size distribution such that a more efficient, predictive and reproducible cavitation response can be achieved *in vivo.* A different way to improve ultrasound-induced drug delivery is to load the microbubbles with drugs and to attach or incorporate drug-loaded nanoparticles to the microbubble surface [190, 218-220]. However, these microbubbles encounter some additional challenges such as relatively poor drug loading and *in vivo* stability issues [218, 221]. Although a large microbubble size can be beneficial for treatment purposes, the opposite is true as well. Being confined in the vascular lumen limits the range of induced effects by the cavitating

microbubbles. Therefore, small nanobubbles and nanodroplets able to exploit the EPR-effect in tumour tissue are developed. Ultrasound can be used to vaporize the (drug-loaded) nanodroplets, creating microbubbles which may locally enhance intracellular drug delivery and improve drug distribution within the tumour interstitium. Similar effects have been observed upon the use of the nanocup, a nanobubble stabilized by a cup-shaped nanoparticle [222]. These nanocups showed *in vivo* cavitation activity for several minutes and were observed to penetrate well beyond the vessel wall. Furthermore, they showed enhanced delivery and penetration in a tumour model of a co-injected antibody [222].

Each of the microbubble discussed above was developed to overcome the limitations of currently used microbubbles and the use of these novel therapeutic microbubbles will expand our knowledge on ultrasound and microbubble treatment. A microbubble which can be used for a range of therapeutic applications would be most beneficial for the clinic but it is also not unlikely that microbubbles will be engineered for a specific application since the different therapeutic application may demand different types of microbubble behaviour.

Acoustic Cluster Therapy and the blood-brain barrier

ACT has shown great therapeutic potential in several preclinical cancer models which resulted in the first in man study (phase I ACTIVATE study, NCT04021277). However, the potential of ACT to increase the permeability of the BBB and consequent brain uptake remains understudied. The work presented in **Paper III** showed for the first time the potential of ACT to increase the permeability of the BBB and facilitate delivery of a clinically relevant nanoparticle such as CCPM. One hour post ACT, a 3.7 fold increase in CCPM accumulation was observed in ACT-treated murine brains opposed to control brains. High magnification CLSM images verified the improved delivery and extravasation of the CCPM upon ACT.

Whereas we did not observe any clear extravasation of the transferrin receptor targeting liposomes upon ultrasound and microbubble treatment (**Paper II**), clear extravasation of the core-crosslinked polymeric micelles (CCPM) into the brain parenchyma was observed upon Acoustic Cluster Therapy® (ACT) (**Paper III**). The two main differences between the two studies were the difference in size of the nanoparticles used and the microbubble platform employed to increase the permeability of the BBB. As previously discussed, the smaller size of the CCPM (~65 nm, **Paper III**) opposed to the liposomes (~180 nm) used in **Paper II** will be beneficial for extravasation purposes upon ultrasound induced opening of inter endothelial cell openings. As discussed earlier, the maximum observed inter-

endothelial cell openings upon ultrasound and microbubble treatment performed with conventional ultrasound contrast agents was observed to be approximately 65 nm. However, ACT is expected to work by a different mechanism compared to conventional microbubbles such that ACT-induced inter-endothelial cell openings could potentially be of a different size.

Unravelling the mechanisms with intravital microscopy

In case of conventional used microbubbles (e.i. ultrasound contrast agents), great effort has been put in understanding the mechanism behind ultrasound induced increase in BBB permeability. Real time *in vivo* multiphoton fluorescence imaging performed simultaneously with ultrasound and microbubble treatment is one of the experimental techniques which contributed greatly to the understanding of ultrasound induced increase of BBB permeability [204, 223, 224]. Whereas the findings are likely translatable between the conventionally used ultrasound contrast agents, ACT most likely works by a different mechanism. We therefore established, with help of experienced collaborators, the aforementioned intravital microscopy technique in our lab. This collaboration resulted in **Paper IV** which describes the surgical and technical procedures that enable real-time *in vivo* multiphoton fluorescence imaging of the rodent brain during focused ultrasound and microbubble treatments. Optical access to the brain is obtained by an open-skull cranial window which is sealed with an optically transparent coverslip. A ring transducer attached to a coverslip is mounted on top with agarose as a coupling medium between the two cover glasses. By intravenously injecting fluorescent dextran conjugates and/or nanoparticles, the vasculature can be visualized, and the effect of focused ultrasound and microbubble treatment can be studied. Even though the temporal resolution is not high enough to image bubble oscillations, this experimental technique will most likely be sufficient to get new insights in the mechanism behind ACT-induced increase of the BBB permeability.

As previously discussed, the latter was studied and observed on a more macroscopical scale in **Paper III** and raised several research questions regarding the mechanism of ACT in the brain. To give some examples: Do the ACT bubbles lodge at the site of activation or do they keep circulating upon activation? How long do the ACT-bubbles reside in the vasculature of a healthy brain? Does activation of the ACT clusters result in dilation of the (micro)vessel and extravasation of the co-injected agent. Is the enhancement exposure step the main driver behind extravasation of the co-injected therapeutic agent? Are the 'clouds of CCPM' observed in **Paper III** the result of a single ACT-bubble? These research questions can hopefully be answered by using the intravital microscopy

procedure described in **Paper IV**. These experiments have been initiated and have already resulted in interesting observations. More experiments still need to be performed, but it will likely contribute to our understanding of how ACT works in the brain. Besides studying the mechanism of ACT, the procedure described in **Paper IV** could also be of interest to study the ultrasound-induced improved delivery to the brain of nanoparticle-based drug delivery systems such as the transferrin receptor-targeting liposomes used in **Paper II**. By imaging the brain both during but also for a certain time after ultrasound and microbubble treatment, novel knowledge on the transport pathways of nanosized drug carriers upon ultrasound and microbubble treatment into the brain can be acquired.

Clinical relevance

The work presented in this thesis describes how several nanoparticle-based drug delivery systems and microbubble platforms were used to improve delivery of nanomedicine to tumour tissue as well as the brain. The findings have increased our understanding on the combined use of nanomedicine and ultrasound and microbubble treatment, but most likely their clinical impact will be of different degrees. The enzyme sensitive liposome used in **Paper I** showed better therapeutical behaviour compared to the non-enzyme sensitive version of the liposome but was clearly outcompeted by the clinically used Doxil formulation. Nevertheless, the idea of combining ultrasound and microbubble treatment with a nanoparticle exhibiting features which improves internalization by tumour cells upon ultrasound-mediated delivery remains to be an interesting approach to improve the therapeutic efficacy of ultrasound and microbubble treatment. The findings in **Paper II** indicated that ultrasound and microbubble treatment improved endocytosis of the transferrin receptor-targeted liposomes. Up to now, ultrasound induced stimulation of endocytosis processes was mainly observed in *in vitro* experiments. These findings can be of clinical relevance, especially when endothelial cells are the main target. However, more information needs to be acquired on the fate of the liposomal load upon ultrasound and microbubble treatment. It would especially be of great interest to know if the cisplatin is transported across the blood-brain barrier and penetrated the brain tissue, since this information can currently not be extracted from the results. The procedure described in **Paper IV** could be employed to study the *in vivo* fate of the blood-brain barrier targeting liposomes upon ultrasound and microbubble treatment. If the payload of the liposomes indeed crosses the blood-brain barrier, this could be an interesting approach to improve drug delivery to the brain. However, to get a representative perspective on its clinical relevance, the delivery efficiency of the transferrin receptor-targeted liposomes should be compared to the performance

of for example smaller sized nanoparticles (~50-100 nm) when combined with ultrasound and microbubble treatment. Exploiting the opened tight junctions could be a more efficient way of drug delivery. In **Paper III** both the use of ACT and the core-crosslinked polymeric micelles (CCPM) are to some extent of clinical relevance. The versatile CCPM have shown great therapeutic potential in both preclinical and clinical work. A therapeutic agent of interest can easily be incorporated into the CCPM, generating a wide range of possible applications. Combining these CCPM with ultrasound and either ACT or a conventional microbubble could generate even more therapeutic applications. In addition, the findings in **Paper III** show that ACT has potential to safely and transiently increase the permeability of the blood-brain barrier. However, more research on the optimal ultrasound settings for ACT when employed in the brain and on the mechanism of ACT should be conducted. Also here, the method described in **Paper IV** can be used to acquire this specific knowledge on ACT. An extra challenge which slows down the translation of ultrasound and microbubble treatment to the clinic is the need for ultrasound transducers that are able to generate the required ultrasound pulses. This demands extensive testing and characterization of the ultrasound probe and ultrasound treatment procedure before it can be safely used in the clinic. In addition, extra care needs to be taken when using low-frequency ultrasound, since there will be a risk of brain damage due to standing waves and inertial cavitation [225].

In several preclinical studies, ultrasound and microbubble treatment has shown its great potential in improving drug delivery to tumours and the brain. The promising results have resulted in several clinical trials in which clinically approved ultrasound contrast agents and drugs are used. Several new microbubble platforms specifically developed for therapeutic applications are currently under development and are expected to be superior to currently employed microbubbles. Even though the future of ultrasound and microbubble treatment in the clinic looks bright, we still do not fully understand the mechanism and all the biophysical effects induced. Although the ongoing clinical trials show that complete understanding of the mechanism is not necessary to get a novel technique to clinic, knowledge on the mechanism can help us to increase the therapeutic potential of ultrasound and microbubble treatments. Either by developing even better microbubble platforms or by developing nanomedicine with features that can exploit the ultrasound induced effects to the fullest. However, it will be a highly challenging task to fully understand the mechanism and induced effects because of several reasons. Firstly, we work with a very complex biological system, which by itself, we do not fully understand yet.

Secondly, there are a large amount of known and still unknown parameters involved. Both reasons will not only make it hard to compare studies to find the perfect ultrasound settings or microbubble to use but will likely make it difficult to reproduce results.

Instead of focusing on fully understanding the mechanism, it could be of interest to study why, in some cases, ultrasound and microbubble treatment does not result in an enhanced treatment effect in tumours or the brain. Even though this is most likely a disappointing result from the researcher's point of view, it will indirectly teach us something about the mechanism of action. If we, for example in case of tumour treatment, could figure out which tumour features are the reason for failure of the ultrasound and microbubble treatment, we could use this information to stratify patients in the clinic. In this case it is important to characterize the tumours well such that the tumour features of interest can be identified. In addition, as already briefly discussed in **Chapter 1** we could try to alter the disadvantageous tumour features such that the tumour becomes more susceptible to ultrasound and microbubble treatment. Furthermore, where conventional ultrasound contrast agents might fail in improving drug delivery to certain tumour types, it might be that some of the newly developed microbubble will be successful in these tumours due to a different mechanism of action. Various microbubble platforms engineered more specifically for enhancing drug delivery will be available in the future such that we might be able to pick the microbubble based on the type of treatment required, just like the way we currently select drugs.

Chapter 6 – Concluding remarks

The combined use of ultrasound and microbubbles has emerged as a promising technique to enhance delivery of drug and drug carriers to tumours and the brain. New nanoparticle-based drug delivery systems and microbubble platforms to achieve more efficient drug delivery to tumours and the brain are continuously being developed. The work presented in this thesis has increased our understanding on how ultrasound and microbubble treatment can be used to improve delivery of nanomedicine to subcutaneous tumour tissue as well as to the brain.

Three nanoparticle-based drug delivery systems have been studied and two types of microbubble platforms have been employed to improve delivery of nanomedicine to either subcutaneous tumours or brain. Firstly, the performance of an enzyme sensitive liposome in a subcutaneous tumour evaluated and compared to a non-enzyme sensitive liposome and the clinically used Doxil liposome. For all three liposomes, improved extravasation and accumulation was observed upon ultrasound and microbubble treatment conducted with the conventional used microbubble SonoVue™. In the therapeutic study, the enzyme sensitive liposome performed better than the non-enzyme sensitive liposome but was outcompeted by the Doxil formulation. The second nanoparticle-based drug delivery system evaluated was a transferrin receptor-targeting liposome. Combining this liposome with ultrasound and microbubble treatment, again conducted with the microbubble SonoVue™, resulted in a 40% increase in accumulation in the ultrasound treated hemisphere opposed to the hemisphere acting as an internal control. Performance of the transferrin receptor-targeting liposome was compared to a liposome lacking blood-brain barrier targeting properties. The latter liposome showed no increased accumulation upon ultrasound and microbubble treatment. This indicated that the observed increase in accumulation of the transferrin receptor-targeting liposome can most likely be assigned to induced endocytosis and/or transcytosis by ultrasound and microbubble treatment. The third nanoparticle-based drug delivery system studied were the versatile core-crosslinked polymeric micelles (CCPM). The potential of the novel microbubble platform Acoustic Cluster Therapy® (ACT) to increase the delivery of the macromolecule IRDye® 800CW-PEG and CCPM to the

murine brain was explored. ACT increased the permeability of the blood-brain barrier significantly which also resulted in a significant increase in accumulation and extravasation of the macromolecule and CCPM in the brain. The ACT-induced increase in permeability of the blood-brain barrier was reversible and no tissue damage was observed.

To be able to obtain a more mechanistic insight on for example the *in vivo* behaviour of ACT in the brain, an intravital microscopy set-up was established with help of experienced collaborators. This collaboration resulted in a methodology paper which describes in detail the surgical and technical procedures required to conduct *in vivo* multiphoton imaging simultaneously with ultrasound and microbubble treatment. In addition, an overview of the type results that can be acquired with this set-up is presented and the challenges and limitations of the procedure are described.

To summarize, the increasing number of preclinical and clinical studies demonstrates that many are convinced that ultrasound and microbubble treatment could impact medicine by enhancing drug delivery and thereby improving and enabling treatments of cancer and various brain diseases.

References

1. Lentacker, I., et al., *Understanding ultrasound induced sonoporation: definitions and underlying mechanisms.* Adv Drug Deliv Rev, 2014. 72: p. 49-64.
2. Snipstad, S., et al., *Sonopermeation to improve drug delivery to tumors: from fundamental understanding to clinical translation.* Expert Opin Drug Deliv, 2018. 15(12): p. 1249-1261.
3. Oh, N. and J.-H. Park, *Endocytosis and exocytosis of nanoparticles in mammalian cells.* International journal of nanomedicine, 2014. 9(Suppl 1): p. 51.
4. Iversen, T.-G., T. Skotland, and K. Sandvig, *Endocytosis and intracellular transport of nanoparticles: present knowledge and need for future studies.* Nano today, 2011. 6(2): p. 176-185.
5. Smith, S.A., et al., *The endosomal escape of nanoparticles: Toward more efficient cellular delivery.* Bioconjugate chemistry, 2018. 30(2): p. 263-272.
6. Abbott, N.J., L. Rönnbäck, and E. Hansson, *Astrocyte–endothelial interactions at the blood–brain barrier.* Nature reviews neuroscience, 2006. 7(1): p. 41.
7. Poon, C., D. McMahon, and K. Hynynen, *Noninvasive and targeted delivery of therapeutics to the brain using focused ultrasound.* Neuropharmacology, 2016.
8. Sun, T., et al., *Engineered nanoparticles for drug delivery in cancer therapy.* Angewandte Chemie International Edition, 2014. 53(46): p. 12320-12364.
9. Peruzzi, G., et al., *Perspectives on cavitation enhanced endothelial layer permeability.* Colloids and Surfaces B: Biointerfaces, 2018. 168: p. 83-93.
10. Tinkle, S., et al., *Nanomedicines: addressing the scientific and regulatory gap.* Annals of the New York Academy of Sciences, 2014. 1313(1): p. 35-56.
11. Peer, D., et al., *Nanocarriers as an emerging platform for cancer therapy.* Nature Nanotechnology, 2007. 2(12): p. 751-760.
12. Farokhzad, O.C. and R. Langer, *Impact of nanotechnology on drug delivery.* ACS nano, 2009. 3(1): p. 16-20.
13. Sanna, V., N. Pala, and M. Sechi, *Targeted therapy using nanotechnology: focus on cancer.* International journal of nanomedicine, 2014. 9: p. 467.
14. Cho, K., et al., *Therapeutic nanoparticles for drug delivery in cancer.* Clinical cancer research, 2008. 14(5): p. 1310-1316.
15. Wilczewska, A.Z., et al., *Nanoparticles as drug delivery systems.* Pharmacological reports, 2012. 64(5): p. 1020-1037.
16. Matsumura, Y. and H. Maeda, *A new concept for macromolecular therapeutics in cancer chemotherapy: mechanism of tumoritropic accumulation of proteins and the antitumor agent smancs.* Cancer research, 1986. 46(12 Part 1): p. 6387-6392.

17. Fang, J., H. Nakamura, and H. Maeda, *The EPR effect: Unique features of tumor blood vessels for drug delivery, factors involved, and limitations and augmentation of the effect.* Adv Drug Deliv Rev, 2011. 63(3): p. 136-51.
18. Iyer, A.K., et al., *Exploiting the enhanced permeability and retention effect for tumor targeting.* Drug Discov Today, 2006. 11(17-18): p. 812-8.
19. Bazak, R., et al., *Cancer active targeting by nanoparticles: a comprehensive review of literature.* Journal of cancer research and clinical oncology, 2015. 141(5): p. 769-784.
20. Gabizon, A., et al., *Tumor cell targeting of liposome-entrapped drugs with phospholipid-anchored folic acid–PEG conjugates.* Advanced drug delivery reviews, 2004. 56(8): p. 1177-1192.
21. Barenholz, Y., *Liposome application: problems and prospects.* Current opinion in colloid & interface science, 2001. 6(1): p. 66-77.
22. Kirpotin, D.B., et al., *Antibody targeting of long-circulating lipidic nanoparticles does not increase tumor localization but does increase internalization in animal models.* Cancer research, 2006. 66(13): p. 6732-6740.
23. Emanuel, N., et al., *Targeted delivery of doxorubicin via sterically stabilized immunoliposomes: pharmacokinetics and biodistribution in tumor-bearing mice.* Pharmaceutical research, 1996. 13(6): p. 861-868.
24. Juweid, M., et al., *Micropharmacology of monoclonal antibodies in solid tumors: direct experimental evidence for a binding site barrier.* Cancer research, 1992. 52(19): p. 5144-5153.
25. Mura, S., J. Nicolas, and P. Couvreur, *Stimuli-responsive nanocarriers for drug delivery.* Nature materials, 2013. 12(11): p. 991-1003.
26. Alexiou, C., et al., *Cancer therapy with drug loaded magnetic nanoparticles—magnetic drug targeting.* Journal of Magnetism and Magnetic Materials, 2011. 323(10): p. 1404-1407.
27. Tietze, R., et al., *Magnetic nanoparticle-based drug delivery for cancer therapy.* Biochemical and biophysical research communications, 2015. 468(3): p. 463-470.
28. Pitt, W.G., G.A. Husseini, and B.J. Staples, *Ultrasonic drug delivery–a general review.* Expert opinion on drug delivery, 2004. 1(1): p. 37-56.
29. Theek, B., et al., *Sonoporation enhances liposome accumulation and penetration in tumors with low EPR.* J Control Release, 2016. 231: p. 77-85.
30. Kotopoulis, S., et al., *Sonoporation-Enhanced Chemotherapy Significantly Reduces Primary Tumour Burden in an Orthotopic Pancreatic Cancer Xenograft.* Molecular Imaging and Biology, 2014. 16(1): p. 53-62.
31. Treat, L.H., et al., *Improved anti-tumor effect of liposomal doxorubicin after targeted blood-brain barrier disruption by MRI-guided focused ultrasound in rat glioma.* Ultrasound Med Biol, 2012. 38(10): p. 1716-25.
32. Liu, H.L., et al., *Blood-brain barrier disruption with focused ultrasound enhances delivery of chemotherapeutic drugs for glioblastoma treatment.* Radiology, 2010. 255(2): p. 415-25.

33. Huang, Q. and J. Du, *Barriers for Tumor Drug Delivery*, in *New Nanomaterials and Techniques for Tumor-targeted Systems*, R. Huang and Y. Wang, Editors. 2020, Springer Singapore: Singapore. p. 5-26.
34. Sriraman, S.K., B. Aryasomayajula, and V.P. Torchilin, *Barriers to drug delivery in solid tumors.* Tissue barriers, 2014. 2(3): p. e29528.
35. Jain, R.K. and T. Stylianopoulos, *Delivering nanomedicine to solid tumors.* Nat Rev Clin Oncol, 2010. 7(11): p. 653-64.
36. Gabizon, A. and F. Martin, *Polyethylene glycol-coated (pegylated) liposomal doxorubicin.* Drugs, 1997. 54(4): p. 15-21.
37. Nunes, S.S., et al., *Influence of PEG coating on the biodistribution and tumor accumulation of pH-sensitive liposomes.* Drug Deliv Transl Res, 2019. 9(1): p. 123-130.
38. Hamidi, M., A. Azadi, and P. Rafiei, *Pharmacokinetic consequences of pegylation.* Drug Deliv, 2006. 13(6): p. 399-409.
39. Ernsting, M.J., et al., *Factors controlling the pharmacokinetics, biodistribution and intratumoral penetration of nanoparticles.* J Control Release, 2013. 172(3): p. 782-94.
40. Harasym, T.O., et al., *Poly(ethylene glycol)-modified phospholipids prevent aggregation during covalent conjugation of proteins to liposomes.* Bioconjug Chem, 1995. 6(2): p. 187-94.
41. Li, S.D. and L. Huang, *Pharmacokinetics and biodistribution of nanoparticles.* Mol Pharm, 2008. 5(4): p. 496-504.
42. Levchenko, T.S., et al., *Liposome clearance in mice: the effect of a separate and combined presence of surface charge and polymer coating.* Int J Pharm, 2002. 240(1-2): p. 95-102.
43. Duan, X. and Y. Li, *Physicochemical characteristics of nanoparticles affect circulation, biodistribution, cellular internalization, and trafficking.* Small, 2013. 9(9-10): p. 1521-1532.
44. Liu, Y., et al., *The shape of things to come: importance of design in nanotechnology for drug delivery.* Therapeutic delivery, 2012. 3(2): p. 181-194.
45. Toy, R., et al., *The effects of particle size, density and shape on margination of nanoparticles in microcirculation.* Nanotechnology, 2011. 22(11): p. 115101.
46. Doshi, N., et al., *Flow and adhesion of drug carriers in blood vessels depend on their shape: a study using model synthetic microvascular networks.* Journal of Controlled Release, 2010. 146(2): p. 196-200.
47. Lee, S.-Y., M. Ferrari, and P. Decuzzi, *Shaping nano-/micro-particles for enhanced vascular interaction in laminar flows.* Nanotechnology, 2009. 20(49): p. 495101.
48. Toy, R., et al., *Shaping cancer nanomedicine: the effect of particle shape on the in vivo journey of nanoparticles.* Nanomedicine, 2014. 9(1): p. 121-134.
49. Smith, B.R., et al., *Shape matters: intravital microscopy reveals surprising geometrical dependence for nanoparticles in tumor models of extravasation.* Nano letters, 2012. 12(7): p. 3369-3377.

50. Arnida, M., et al., *Geometry and surface characteristics of gold nanoparticles influence their biodistribution and uptake by macrophages.* European Journal of Pharmaceutics and Biopharmaceutics, 2011. 77(3): p. 417.
51. Wolak, D.J. and R.G. Thorne, *Diffusion of macromolecules in the brain: implications for drug delivery.* Mol Pharm, 2013. 10(5): p. 1492-504.
52. Maeda, H., et al., *Tumor vascular permeability and the EPR effect in macromolecular therapeutics: a review.* J Control Release, 2000. 65(1-2): p. 271-84.
53. Hobbs, S.K., et al., *Regulation of transport pathways in tumor vessels: role of tumor type and microenvironment.* Proceedings of the National Academy of Sciences, 1998. 95(8): p. 4607-4612.
54. Hansen, A.E., et al., *Positron Emission Tomography Based Elucidation of the Enhanced Permeability and Retention Effect in Dogs with Cancer Using Copper-64 Liposomes.* ACS Nano, 2015. 9(7): p. 6985-95.
55. Nichols, J.W. and Y.H. Bae, *EPR: Evidence and fallacy.* Journal of Controlled Release, 2014. 190: p. 451-464.
56. Moghimi, S. and D. Simberg, *Nanoparticle transport pathways into tumors.* Journal of Nanoparticle Research, 2018. 20(6): p. 169.
57. Sindhwani, S., et al., *The entry of nanoparticles into solid tumours.* Nature materials, 2020. 19(5): p. 566-575.
58. Nakamura, Y., et al., *Nanodrug delivery: is the enhanced permeability and retention effect sufficient for curing cancer?* Bioconjugate chemistry, 2016. 27(10): p. 2225-2238.
59. Maeda, H., *Toward a full understanding of the EPR effect in primary and metastatic tumors as well as issues related to its heterogeneity.* Advanced drug delivery reviews, 2015. 91: p. 3-6.
60. Dagogo-Jack, I. and A.T. Shaw, *Tumour heterogeneity and resistance to cancer therapies.* Nature reviews Clinical oncology, 2018. 15(2): p. 81.
61. Minchinton, A.I. and I.F. Tannock, *Drug penetration in solid tumours.* Nature Reviews Cancer, 2006. 6(8): p. 583-592.
62. Boucher, Y., L.T. Baxter, and R.K. Jain, *Interstitial pressure gradients in tissue-isolated and subcutaneous tumors: implications for therapy.* Cancer research, 1990. 50(15): p. 4478-4484.
63. Jain, R.K., *Delivery of molecular and cellular medicine to solid tumors.* Microcirculation, 1997. 4(1): p. 1-23.
64. Heldin, C.-H., et al., *High interstitial fluid pressure—an obstacle in cancer therapy.* Nature Reviews Cancer, 2004. 4(10): p. 806-813.
65. Heine, M., et al., *High interstitial fluid pressure is associated with low tumour penetration of diagnostic monoclonal antibodies applied for molecular imaging purposes.* PloS one, 2012. 7(5): p. e36258.
66. Lu, P., V.M. Weaver, and Z. Werb, *The extracellular matrix: a dynamic niche in cancer progression.* Journal of Cell Biology, 2012. 196(4): p. 395-406.

67. Zhang, Z., et al., *Rational design of nanoparticles with deep tumor penetration for effective treatment of tumor metastasis.* Advanced Functional Materials, 2018. 28(40): p. 1801840.
68. Barua, S. and S. Mitragotri, *Challenges associated with penetration of nanoparticles across cell and tissue barriers: a review of current status and future prospects.* Nano today, 2014. 9(2): p. 223-243.
69. Miao, L., C.M. Lin, and L. Huang, *Stromal barriers and strategies for the delivery of nanomedicine to desmoplastic tumors.* Journal of Controlled Release, 2015. 219: p. 192-204.
70. Dai, Q., et al., *Quantifying the Ligand-Coated Nanoparticle Delivery to Cancer Cells in Solid Tumors.* ACS Nano, 2018. 12(8): p. 8423-8435.
71. Miao, L., et al., *The binding site barrier elicited by tumor-associated fibroblasts interferes disposition of nanoparticles in stroma-vessel type tumors.* ACS nano, 2016. 10(10): p. 9243-9258.
72. Miller, M.A., et al., *Tumour-associated macrophages act as a slow-release reservoir of nano-therapeutic Pt (IV) pro-drug.* Nature communications, 2015. 6(1): p. 1-13.
73. Biancacci, I., et al., *Optical imaging of the whole-body to cellular biodistribution of clinical-stage PEG-b-pHPMA-based core-crosslinked polymeric micelles.* Journal of Controlled Release, 2020.
74. Zhou, J., et al., *Tumor-Associated Macrophages: Recent Insights and Therapies.* Frontiers in Oncology, 2020. 10: p. 188.
75. Hao Zhou, Z.F., J. Deng, P.K. Lemons, D.C. Arhontoulis, W.B. Bowne, H. Cheng, *Hyaluronidase embedded in nanocarrier PEG shell for enhanced tumor penetration and highly efficient antitumor efficacy.* Nano Letters, 2016. 16.5: p. 2368-3277.
76. Lieleg, O., R.M. Baumgartel, and A.R. Bausch, *Selective filtering of particles by the extracellular matrix: an electrostatic bandpass.* Biophys J, 2009. 97(6): p. 1569-77.
77. Romberg, B., W.E. Hennink, and G. Storm, *Sheddable coatings for long-circulating nanoparticles.* Pharm Res, 2008. 25(1): p. 55-71.
78. Zhang, Y.R., et al., *Strategies to improve tumor penetration of nanomedicines through nanoparticle design.* Wiley Interdisciplinary Reviews-Nanomedicine and Nanobiotechnology, 2019. 11(1): p. 1519.
79. Gouarderes, S., et al., *Vascular and extracellular matrix remodeling by physical approaches to improve drug delivery at the tumor site.* Expert Opinion on Drug Delivery, 2020: p. 1-24.
80. Dolor, A. and F.C. Szoka Jr, *Digesting a path forward: the utility of collagenase tumor treatment for improved drug delivery.* Molecular pharmaceutics, 2018. 15(6): p. 2069-2083.
81. Lee, S., et al., *Extracellular matrix remodeling in vivo for enhancing tumor-targeting efficiency of nanoparticle drug carriers using the pulsed high intensity focused ultrasound.* Journal of Controlled Release, 2017. 263: p. 68-78.

82. Eikenes, L., et al., *Collagenase increases the transcapillary pressure gradient and improves the uptake and distribution of monoclonal antibodies in human osteosarcoma xenografts.* Cancer research, 2004. 64(14): p. 4768-4773.
83. Eikenes, L., et al., *Hyaluronidase induces a transcapillary pressure gradient and improves the distribution and uptake of liposomal doxorubicin (Caelyx™) in human osteosarcoma xenografts.* British journal of cancer, 2005. 93(1): p. 81-88.
84. Cun, X., et al., *A dual strategy to improve the penetration and treatment of breast cancer by combining shrinking nanoparticles with collagen depletion by losartan.* Acta biomaterialia, 2016. 31: p. 186-196.
85. Zhang, B., et al., *Cyclopamine disrupts tumor extracellular matrix and improves the distribution and efficacy of nanotherapeutics in pancreatic cancer.* Biomaterials, 2016. 103: p. 12-21.
86. Zhu, M., et al., *Physicochemical properties determine nanomaterial cellular uptake, transport, and fate.* Accounts of chemical research, 2013. 46(3): p. 622-631.
87. Verma, A. and F. Stellacci, *Effect of surface properties on nanoparticle-cell interactions.* Small, 2010. 6(1): p. 12-21.
88. Lazarovits, J., et al., *Nanoparticle-blood interactions: the implications on solid tumour targeting.* Chem Commun (Camb), 2015. 51(14): p. 2756-67.
89. Szakács, G., et al., *Targeting multidrug resistance in cancer.* Nature reviews Drug discovery, 2006. 5(3): p. 219-234.
90. Fletcher, J.I., et al., *ABC transporters in cancer: more than just drug efflux pumps.* Nature Reviews Cancer, 2010. 10(2): p. 147-156.
91. Gottesman, M.M., T. Fojo, and S.E. Bates, *Multidrug resistance in cancer: role of ATP–dependent transporters.* Nature Reviews Cancer, 2002. 2(1): p. 48-58.
92. Abbott, N.J., et al., *Structure and function of the blood-brain barrier.* Neurobiol Dis, 2010. 37(1): p. 13-25.
93. Pardridge, W.M., *Drug transport across the blood-brain barrier.* J Cereb Blood Flow Metab, 2012. 32(11): p. 1959-72.
94. Serlin, Y., et al. *Anatomy and physiology of the blood–brain barrier*. in *Seminars in cell & developmental biology*. 2015. Elsevier.
95. Greene, C. and M. Campbell, *Tight junction modulation of the blood brain barrier: CNS delivery of small molecules.* Tissue barriers, 2016. 4(1): p. e1138017.
96. Sharif, Y., et al., *Blood brain barrier: A review of its anatomy and physiology in health and disease.* Clinical Anatomy, 2018. 31(6): p. 812-823.
97. Peppiatt, C.M., et al., *Bidirectional control of CNS capillary diameter by pericytes.* Nature, 2006. 443(7112): p. 700-704.
98. Armulik, A., G. Genové, and C. Betsholtz, *Pericytes: developmental, physiological, and pathological perspectives, problems, and promises.* Developmental cell, 2011. 21(2): p. 193-215.
99. Armulik, A., et al., *Pericytes regulate the blood–brain barrier.* Nature, 2010. 468(7323): p. 557-561.

100. Streit, W.J., et al., *Role of microglia in the central nervous system's immune response.* Neurological research, 2005. 27(7): p. 685-691.
101. Zhang, T.T., et al., *Strategies for transporting nanoparticles across the blood-brain barrier.* Biomater Sci, 2016. 4(2): p. 219-29.
102. Pulgar, V.M., *Transcytosis to cross the blood brain barrier, new advancements and challenges.* Frontiers in neuroscience, 2019. 12: p. 1019.
103. Li, G., K. Shao, and C.S. Umeshappa, *Recent progress in blood-brain barrier transportation research*, in *Brain Targeted Drug Delivery System*, H. Gao and X. Gao, Editors. 2019, Academic Press. p. 33-51.
104. Fu, B.M., *Transport across the blood-brain barrier*, in *Molecular, Cellular, and Tissue Engineering of the Vascular System*. 2018, Springer. p. 235-259.
105. Lu, W., *Adsorptive-mediated brain delivery systems.* Current pharmaceutical biotechnology, 2012. 13(12): p. 2340-2348.
106. Shen, S. and W. Zhang, *ABC transporters and drug efflux at the blood-brain barrier.* Reviews in the Neurosciences, 2010. 21(1): p. 29.
107. Löscher, W. and H. Potschka, *Role of drug efflux transporters in the brain for drug disposition and treatment of brain diseases.* Progress in neurobiology, 2005. 76(1): p. 22-76.
108. Pardridge, W.M. and R.J. Boado, *Reengineering biopharmaceuticals for targeted delivery across the blood-brain barrier.* Methods Enzymol, 2012. 503: p. 269-92.
109. Rapoport, S.I., *Osmotic opening of the blood-brain barrier: principles, mechanism, and therapeutic applications.* Cell Mol Neurobiol, 2000. 20(2): p. 217-30.
110. Nagy, Z., et al., *Opening of tight junctions in cerebral endothelium. I. Effect of hyperosmolar mannitol infused through the internal carotid artery.* Journal of Comparative Neurology, 1979. 185(3): p. 569-578.
111. Burgess, A. and K. Hynynen, *Noninvasive and targeted drug delivery to the brain using focused ultrasound.* ACS Chem Neurosci, 2013. 4(4): p. 519-26.
112. Dhuria, S.V., L.R. Hanson, and W.H. Frey, 2nd, *Intranasal delivery to the central nervous system: mechanisms and experimental considerations.* J Pharm Sci, 2010. 99(4): p. 1654-73.
113. Lochhead, J.J. and R.G. Thorne, *Intranasal delivery of biologics to the central nervous system.* Adv Drug Deliv Rev, 2012. 64(7): p. 614-28.
114. Illum, L., *Nasal drug delivery - recent developments and future prospects.* J Control Release, 2012. 161(2): p. 254-63.
115. White, E., et al., *A robust MRI-compatible system to facilitate highly accurate stereotactic administration of therapeutic agents to targets within the brain of a large animal model.* J Neurosci Methods, 2011. 195(1): p. 78-87.
116. Hynynen, K., et al., *Noninvasive MR imaging-guided focal opening of the blood-brain barrier in rabbits.* Radiology, 2001. 220(3): p. 640-6.
117. Burgess, A., et al., *Focused ultrasound-mediated drug delivery through the blood-brain barrier.* Expert Rev Neurother, 2015. 15(5): p. 477-91.

118. Liu, H.L., et al., *Combining microbubbles and ultrasound for drug delivery to brain tumors: current progress and overview.* Theranostics, 2014. 4(4): p. 432-44.
119. McDannold, N., N. Vykhodtseva, and K. Hynynen, *Blood-brain barrier disruption induced by focused ultrasound and circulating preformed microbubbles appears to be characterized by the mechanical index.* Ultrasound Med Biol, 2008. 34(5): p. 834-40.
120. Meairs, S. and A. Alonso, *Ultrasound, microbubbles and the blood-brain barrier.* Prog Biophys Mol Biol, 2007. 93(1-3): p. 354-62.
121. Alkins, R., et al., *Focused ultrasound delivers targeted immune cells to metastatic brain tumors.* Cancer Res, 2013. 73(6): p. 1892-9.
122. Burgess, A., et al., *Targeted delivery of neural stem cells to the brain using MRI-guided focused ultrasound to disrupt the blood-brain barrier.* PLoS One, 2011. 6(11): p. e27877.
123. Etame, A.B., et al., *Enhanced delivery of gold nanoparticles with therapeutic potential into the brain using MRI-guided focused ultrasound.* Nanomedicine, 2012. 8(7): p. 1133-42.
124. Kobus, T., et al., *Growth inhibition in a brain metastasis model by antibody delivery using focused ultrasound-mediated blood-brain barrier disruption.* J Control Release, 2016. 238: p. 281-288.
125. Miller, D.L., et al., *Overview of therapeutic ultrasound applications and safety considerations.* Journal of ultrasound in medicine, 2012. 31(4): p. 623-634.
126. Fulgham, P.F., *Physical Principles of Ultrasound*, in *Practical Urological Ultrasound*. 2017, Springer. p. 13-30.
127. O'Brien Jr, W.D., *Ultrasound–biophysics mechanisms.* Progress in biophysics and molecular biology, 2007. 93(1-3): p. 212-255.
128. Schlesinger, I., A. Sinai, and M. Zaaroor, *MRI-guided focused ultrasound in Parkinson's disease: a review.* Parkinson's Disease, 2017. 2017.
129. Meng, Y., K. Hynynen, and N. Lipsman, *Applications of focused ultrasound in the brain: From thermoablation to drug delivery.* Nature Reviews Neurology, 2020: p. 1-16.
130. Zhou, Y., *Ultrasound-mediated drug/gene delivery in solid tumor treatment.* Journal of healthcare engineering, 2013. 4.
131. Frenkel, V., *Ultrasound mediated delivery of drugs and genes to solid tumors.* Adv Drug Deliv Rev, 2008. 60(10): p. 1193-208.
132. Couture, O., et al., *Review of ultrasound mediated drug delivery for cancer treatment: updates from pre-clinical studies.* Transl Cancer Res, 2014. 3(5): p. 494-511.
133. Song, J.H., A. Healey, and P. Prentice, *High-speed observations of Acoustic Cluster Therapy "activation" and "therapy".* The Journal of the Acoustical Society of America, 2018. 144(3): p. 1852-1852.

134. Yudina, A. and C. Moonen, *Ultrasound-induced cell permeabilisation and hyperthermia: strategies for local delivery of compounds with intracellular mode of action.* International journal of hyperthermia, 2012. 28(4): p. 311-319.
135. Jain, A., et al., *Ultrasound-based triggered drug delivery to tumors.* Drug delivery and translational research, 2018. 8(1): p. 150-164.
136. Udroiu, I., *Ultrasonic drug delivery in Oncology.* JBUON, 2015. 20: p. 381-390.
137. Partanen, A., et al., *Mild hyperthermia with magnetic resonance-guided high-intensity focused ultrasound for applications in drug delivery.* International journal of hyperthermia, 2012. 28(4): p. 320-336.
138. Dayton, P., et al., *Acoustic radiation force in vivo: a mechanism to assist targeting of microbubbles.* Ultrasound in medicine & biology, 1999. 25(8): p. 1195-1201.
139. Hernot, S. and A.L. Klibanov, *Microbubbles in ultrasound-triggered drug and gene delivery.* Advanced drug delivery reviews, 2008. 60(10): p. 1153-1166.
140. Husseini, G.A., W.G. Pitt, and A.M. Martins, *Ultrasonically triggered drug delivery: breaking the barrier.* Colloids and surfaces B: Biointerfaces, 2014. 123: p. 364-386.
141. Kooiman, K., et al., *Ultrasound-responsive cavitation nuclei for therapy and drug delivery.* Ultrasound in Medicine & Biology, 2020.
142. Versluis, M., et al., *Ultrasound Contrast Agent Modeling: A Review.* Ultrasound in Medicine & Biology, 2020.
143. Hu, Y., J.M. Wan, and A.C. Yu, *Membrane perforation and recovery dynamics in microbubble-mediated sonoporation.* Ultrasound Med Biol, 2013. 39(12): p. 2393-405.
144. Ward, M., J. Wu, and J.-F. Chiu, *Ultrasound-induced cell lysis and sonoporation enhanced by contrast agents.* The Journal of the Acoustical Society of America, 1999. 105(5): p. 2951-2957.
145. Fan, Z., D. Chen, and C. Deng, *Improving ultrasound gene transfection efficiency by controlling ultrasound excitation of microbubbles.* Journal of Controlled Release, 2013. 170(3): p. 401-413.
146. Escoffre, J.-M., et al., *New insights on the role of ROS in the mechanisms of sonoporation-mediated gene delivery.* Ultrasonics Sonochemistry, 2020. 64: p. 104998.
147. Juffermans, L.J., et al., *Low-intensity ultrasound-exposed microbubbles provoke local hyperpolarization of the cell membrane via activation of BKCa channels.* Ultrasound in medicine & biology, 2008. 34(3): p. 502-508.
148. Juffermans, L., et al., *Transient permeabilization of cell membranes by ultrasound-exposed microbubbles is related to formation of hydrogen peroxide.* American Journal of Physiology-Heart and Circulatory Physiology, 2006. 291(4): p. H1595-H1601.
149. Sheikov, N., et al., *Effect of focused ultrasound applied with an ultrasound contrast agent on the tight junctional integrity of the brain microvascular endothelium.* Ultrasound Med Biol, 2008. 34(7): p. 1093-104.

150. Sheikov, N., et al., *Cellular mechanisms of the blood-brain barrier opening induced by ultrasound in presence of microbubbles.* Ultrasound Med Biol, 2004. 30(7): p. 979-89.
151. De Cock, I., et al., *Ultrasound and microbubble mediated drug delivery: acoustic pressure as determinant for uptake via membrane pores or endocytosis.* Journal of controlled release, 2015. 197: p. 20-28.
152. Hauser, J., et al., *Ultrasound enhanced endocytotic activity of human fibroblasts.* Ultrasound Med Biol, 2009. 35(12): p. 2084-92.
153. Meijering, B.D., et al., *Ultrasound and microbubble-targeted delivery of macromolecules is regulated by induction of endocytosis and pore formation.* Circulation research, 2009. 104(5): p. 679-687.
154. Fekri, F., et al., *Ultrasound Microbubble Treatment Enhances Clathrin-Mediated Endocytosis and Fluid-Phase Uptake through Distinct Mechanisms.* PLoS One, 2016. 11(6): p. e0156754.
155. Yuana, Y., et al., *Microbubbles-assisted ultrasound triggers the release of extracellular vesicles.* International journal of molecular sciences, 2017. 18(8): p. 1610.
156. Afadzi, M., et al., *Mechanisms of the ultrasound-mediated intracellular delivery of liposomes and dextrans.* IEEE transactions on ultrasonics, ferroelectrics, and frequency control, 2012. 60(1): p. 21-33.
157. Aryal, M., et al., *Effects on P-glycoprotein expression after blood-brain barrier disruption using focused ultrasound and microbubbles.* PLoS One, 2017. 12(1): p. e0166061.
158. Cho, H., et al., *Localized down-regulation of P-glycoprotein by focused ultrasound and microbubbles induced blood-brain barrier disruption in rat brain.* Scientific reports, 2016. 6: p. 31201.
159. Yemane, P.T., et al., *Effect of Ultrasound on the Vasculature and Extravasation of Nanoscale Particles Imaged in Real Time.* Ultrasound Med Biol, 2019. 45(11): p. 3028-3041.
160. Keravnou, C.P., et al., *Microvascular Injury and Perfusion Changes Induced by Ultrasound and Microbubbles in a Machine-Perfused Pig Liver.* Ultrasound Med Biol, 2016. 42(11): p. 2676-2686.
161. Goertz, D.E., *An overview of the influence of therapeutic ultrasound exposures on the vasculature: high intensity ultrasound and microbubble-mediated bioeffects.* International Journal of Hyperthermia, 2015. 31(2): p. 134-144.
162. Goertz, D.E., et al., *Antitumor effects of combining docetaxel (taxotere) with the antivascular action of ultrasound stimulated microbubbles.* PLoS One, 2012. 7(12): p. e52307.
163. Goertz, D.E., R. Karshafian, and K. Hynynen. *Antivascular effects of pulsed low intensity ultrasound and microbubbles in mouse tumors*. in *2008 IEEE Ultrasonics Symposium*. 2008. IEEE.

164. Shi, G., et al., *Low-frequency HIFU induced cancer immunotherapy: tempting challenges and potential opportunities.* Cancer Biology & Medicine, 2019. 16(4): p. 714.
165. Wu, F., L. Zhou, and W.R. Chen, *Host antitumour immune responses to HIFU ablation.* International Journal of Hyperthermia, 2007. 23(2): p. 165-171.
166. Riesz, P. and T. Kondo, *Free radical formation induced by ultrasound and its biological implications.* Free Radical Biology and Medicine, 1992. 13(3): p. 247-270.
167. VanBavel, E., *Effects of shear stress on endothelial cells: possible relevance for ultrasound applications.* Progress in biophysics and molecular biology, 2007. 93(1-3): p. 374-383.
168. Dimcevski, G., et al., *A human clinical trial using ultrasound and microbubbles to enhance gemcitabine treatment of inoperable pancreatic cancer.* Journal of Controlled Release, 2016. 243: p. 172-181.
169. Eisenbrey, J.R., et al., *Sensitization of hypoxic tumors to radiation therapy using ultrasound-sensitive oxygen microbubbles.* International Journal of Radiation Oncology* Biology* Physics, 2018. 101(1): p. 88-96.
170. Sercombe, L., et al., *Advances and challenges of liposome assisted drug delivery.* Frontiers in pharmacology, 2015. 6: p. 286.
171. Olsman, M., et al., *Ultrasound-mediated delivery enhances therapeutic efficacy of MMP sensitive liposomes.* Journal of Controlled Release, 2020. 325: p. 121-134.
172. Miller, C.R., et al., *Liposome-cell interactions in vitro: effect of liposome surface charge on the binding and endocytosis of conventional and sterically stabilized liposomes.* Biochemistry, 1998. 37(37): p. 12875-83.
173. Mishra, S., P. Webster, and M.E. Davis, *PEGylation significantly affects cellular uptake and intracellular trafficking of non-viral gene delivery particles.* European Journal of Cell Biology, 2004. 83(3): p. 97-111.
174. Roomi, M.W., et al., *Patterns of MMP-2 and MMP-9 expression in human cancer cell lines.* Oncol Rep, 2009. 21(5): p. 1323-33.
175. Talelli, M., et al., *Core-crosslinked polymeric micelles: principles, preparation, biomedical applications and clinical translation.* Nano today, 2015. 10(1): p. 93-117.
176. Hu, Q., et al., *Tailoring the physicochemical properties of core-crosslinked polymeric micelles for pharmaceutical applications.* Journal of controlled release, 2016. 244: p. 314-325.
177. Coimbra, M., et al., *Antitumor efficacy of dexamethasone-loaded core-crosslinked polymeric micelles.* Journal of controlled release, 2012. 163(3): p. 361-367.
178. Hu, Q., et al., *Complete regression of breast tumour with a single dose of docetaxel-entrapped core-cross-linked polymeric micelles.* Biomaterials, 2015. 53: p. 370-378.
179. Schneider, M., *Characteristics of sonovue™.* Echocardiography, 1999. 16: p. 743-746.

180. Lin, Y., et al., *Effect of acoustic parameters on the cavitation behavior of SonoVue microbubbles induced by pulsed ultrasound.* Ultrason Sonochem, 2017. 35(Pt A): p. 176-184.
181. Wu, S.K., et al., *Characterization of Different Microbubbles in Assisting Focused Ultrasound-Induced Blood-Brain Barrier Opening.* Sci Rep, 2017. 7: p. 46689.
182. Sontum, P., et al., *Acoustic Cluster Therapy (ACT)–A novel concept for ultrasound mediated, targeted drug delivery.* International journal of pharmaceutics, 2015. 495(2): p. 1019-1027.
183. Bush, N., et al., *Theranostic attributes of Acoustic Cluster Therapy and its use for enhancing the effectiveness of liposomal doxorubicin treatment of human triple negative breast cancer in mice.* Frontiers in Pharmacology, 2020. 11: p. 75.
184. Bush, N.L., et al., *Therapeutic dose response of acoustic cluster therapy in combination with irinotecan for the treatment of human colon cancer in mice.* Frontiers in pharmacology, 2019. 10: p. 1299.
185. Kotopoulis, S., et al., *Sonoporation with Acoustic Cluster Therapy (ACT®) induces transient tumour volume reduction in a subcutaneous xenograft model of pancreatic ductal adenocarcinoma.* Journal of Controlled Release, 2017. 245: p. 70-80.
186. van Wamel, A., et al., *Acoustic Cluster Therapy (ACT) enhances the therapeutic efficacy of paclitaxel and Abraxane® for treatment of human prostate adenocarcinoma in mice.* Journal of controlled release, 2016. 236: p. 15-21.
187. Wilhelm, S., et al., *Analysis of nanoparticle delivery to tumours.* Nature reviews materials, 2016. 1(5): p. 1-12.
188. Ouyang, B., et al., *The dose threshold for nanoparticle tumour delivery.* Nature Materials, 2020: p. 1-10.
189. Skotland, T. and K. Sandvig, *Transport of nanoparticles across the endothelial cell layer.* Nano Today, 2020. 36: p. 101029.
190. Snipstad, S., et al., *Ultrasound Improves the Delivery and Therapeutic Effect of Nanoparticle-Stabilized Microbubbles in Breast Cancer Xenografts.* Ultrasound Med Biol, 2017. 43(11): p. 2651-2669.
191. van Wamel, A., et al., *Acoustic Cluster Therapy (ACT)—pre-clinical proof of principle for local drug delivery and enhanced uptake.* Journal of Controlled Release, 2016. 224: p. 158-164.
192. Eggen, S., et al., *Ultrasound-enhanced drug delivery in prostate cancer xenografts by nanoparticles stabilizing microbubbles.* J Control Release, 2014. 187: p. 39-49.
193. Andresen, T.L., D.H. Thompson, and T. Kaasgaard, *Enzyme-triggered nanomedicine: Drug release strategies in cancer therapy (Invited Review).* Molecular membrane biology, 2010. 27(7): p. 353-363.
194. Tinkov, S., et al., *New doxorubicin-loaded phospholipid microbubbles for targeted tumor therapy: in-vivo characterization.* Journal of Controlled Release, 2010. 148(3): p. 368-372.

195. Chowdhury, S.M., et al., *Ultrasound and microbubble mediated therapeutic delivery: Underlying mechanisms and future outlook.* Journal of Controlled Release, 2020.
196. Helfield, B., et al., *Biophysical insight into mechanisms of sonoporation.* Proceedings of the National Academy of Sciences, 2016. 113(36): p. 9983-9988.
197. Pang, Z., et al., *Enhanced intracellular delivery and chemotherapy for glioma rats by transferrin-conjugated biodegradable polymersomes loaded with doxorubicin.* Bioconjug Chem, 2011. 22(6): p. 1171-80.
198. McMahon, D., R. Bendayan, and K. Hynynen, *Acute effects of focused ultrasound-induced increases in blood-brain barrier permeability on rat microvascular transcriptome.* Scientific reports, 2017. 7: p. 45657.
199. Lai, P., et al., *Breast tumor response to ultrasound mediated excitation of microbubbles and radiation therapy in vivo.* Oncoscience, 2016. 3(3-4): p. 98.
200. Czarnota, G.J., et al., *Tumor radiation response enhancement by acoustical stimulation of the vasculature.* Proceedings of the National Academy of Sciences, 2012. 109(30): p. E2033-E2041.
201. Tran, W., et al., *Microbubble and ultrasound radioenhancement of bladder cancer.* British journal of cancer, 2012. 107(3): p. 469-476.
202. Graham, K. and E. Unger, *Overcoming tumor hypoxia as a barrier to radiotherapy, chemotherapy and immunotherapy in cancer treatment.* International journal of nanomedicine, 2018. 13: p. 6049.
203. Liu, H.-L., et al., *Low-pressure pulsed focused ultrasound with microbubbles promotes an anticancer immunological response.* Journal of translational medicine, 2012. 10(1): p. 221.
204. Nhan, T., et al., *Drug delivery to the brain by focused ultrasound induced blood-brain barrier disruption: quantitative evaluation of enhanced permeability of cerebral vasculature using two-photon microscopy.* J Control Release, 2013. 172(1): p. 274-280.
205. Chen, H. and E.E. Konofagou, *The size of blood–brain barrier opening induced by focused ultrasound is dictated by the acoustic pressure.* Journal of Cerebral Blood Flow & Metabolism, 2014. 34(7): p. 1197-1204.
206. Samiotaki, G. and E.E. Konofagou, *Dependence of the reversibility of focused-ultrasound-induced blood-brain barrier opening on pressure and pulse length in vivo.* IEEE transactions on ultrasonics, ferroelectrics, and frequency control, 2013. 60(11): p. 2257-2265.
207. Ohta, S., et al., *Investigating the optimum size of nanoparticles for their delivery into the brain assisted by focused ultrasound-induced blood–brain barrier opening.* Scientific reports, 2020. 10(1): p. 1-13.
208. Gao, K. and X. Jiang, *Influence of particle size on transport of methotrexate across blood brain barrier by polysorbate 80-coated polybutylcyanoacrylate nanoparticles.* Int J Pharm, 2006. 310(1-2): p. 213-9.

209. Wang, S., et al., *Microbubble type and distribution dependence of focused ultrasound-induced blood–brain barrier opening.* Ultrasound in medicine & biology, 2014. 40(1): p. 130-137.
210. Choi, J.J., et al., *Microbubble-size dependence of focused ultrasound-induced blood-brain barrier opening in mice in vivo.* IEEE Trans Biomed Eng, 2010. 57(1): p. 145-54.
211. Song, K.-H., et al., *Microbubble gas volume: A unifying dose parameter in blood-brain barrier opening by focused ultrasound.* Theranostics, 2017. 7(1): p. 144.
212. Johnsen, K.B. and T. Moos, *Revisiting nanoparticle technology for blood-brain barrier transport: Unfolding at the endothelial gate improves the fate of transferrin receptor-targeted liposomes.* J Control Release, 2016. 222: p. 32-46.
213. Kucharz, K., et al., *Post-capillary venules is the locus for transcytosis of therapeutic nanoparticles to the brain.* bioRxiv, 2020: p. 2020.06.05.133819.
214. Burnside, E. and E. Bradbury, *Manipulating the extracellular matrix and its role in brain and spinal cord plasticity and repair.* Neuropathology and applied neurobiology, 2014. 40(1): p. 26-59.
215. Arvanitis, C.D., et al., *Passive mapping of cavitation activity for monitoring of drug delivery.* The Journal of the Acoustical Society of America, 2010. 127(3): p. 1977-1977.
216. Choi, J.J., et al., *Non-invasive and real-time passive acoustic mapping of ultrasound-mediated drug delivery.* Physics in Medicine & Biology, 2014. 59(17): p. 4861.
217. O'Reilly, M.A. and K. Hynynen, *Blood-brain barrier: Real-time feedback-controlled focused ultrasound disruption by using an acoustic emissions–based controller.* Radiology, 2012. 263(1): p. 96-106.
218. Gong, Q., et al., *Drug-loaded microbubbles combined with ultrasound for thrombolysis and malignant tumor therapy.* BioMed research international, 2019. 2019.
219. Fan, C.H., et al., *Drug-loaded bubbles with matched focused ultrasound excitation for concurrent blood-brain barrier opening and brain-tumor drug delivery.* Acta Biomater, 2015. 15: p. 89-101.
220. Geers, B., et al., *Self-assembled liposome-loaded microbubbles: The missing link for safe and efficient ultrasound triggered drug-delivery.* Journal of controlled release, 2011. 152(2): p. 249-256.
221. Zhao, Y.-Z., et al., *Potential and problems in ultrasound-responsive drug delivery systems.* International journal of nanomedicine, 2013. 8: p. 1621.
222. Kwan, J.J., et al., *Ultrasound-propelled nanocups for drug delivery.* small, 2015. 11(39): p. 5305-5314.
223. Cho, E.E., et al., *Two-photon fluorescence microscopy study of cerebrovascular dynamics in ultrasound-induced blood-brain barrier opening.* J Cereb Blood Flow Metab, 2011. 31(9): p. 1852-62.

224. Burgess, A., et al., *Analysis of focused ultrasound-induced blood–brain barrier permeability in a mouse model of Alzheimer's disease using two-photon microscopy.* Journal of controlled release, 2014. 192: p. 243-248.
225. Baron, C., et al., *Simulation of intracranial acoustic fields in clinical trials of sonothrombolysis.* Ultrasound in medicine & biology, 2009. 35(7): p. 1148-1158.

PAPER I

Ultrasound-mediated delivery enhances therapeutic efficacy of MMP sensitive liposomes

Marieke Olsman, Viktoria Sereti, Kristine Andreassen, Sofie Snipstad, Annemieke van Wamel, Rasmus Eliasen, Sigrid Berg, Andrew James Urquhart, Thomas Lars Andresen, Catharina de Lange Davies

Journal of Controlled Release | 2020

Journal of Controlled Release 325 (2020) 121–134

Contents lists available at ScienceDirect

Journal of Controlled Release

journal homepage: www.elsevier.com/locate/jconrel

Monograph

Ultrasound-mediated delivery enhances therapeutic efficacy of MMP sensitive liposomes

Marieke Olsman[a,*], Viktoria Sereti[b], Kristine Andreassen[a], Sofie Snipstad[a,c,f], Annemieke van Wamel[a], Rasmus Eliasen[b], Sigrid Berg[d,e,f], Andrew J. Urquhart[b], Thomas L. Andresen[b], Catharina de Lange Davies[a]

[a] Department of Physics, Norwegian University of Science and Technology, Trondheim, Norway
[b] Department of Health Technology, Center for Nanomedicine and Theranostics, Technical University Denmark, DTU Healthtech, Lyngby, Denmark
[c] Department of Biotechnology and Nanomedicine, SINTEF Industry, Trondheim, Norway
[d] Department of Circulation and Medical Imaging, Norwegian University of Science and Technology, Trondheim, Norway
[e] Department of Health Research, SINTEF Digital, Trondheim, Norway
[f] Cancer Clinic, St. Olavs Hospital, Trondheim, Norway

ARTICLE INFO

Keywords:
Drug delivery system
Ultrasound-mediated delivery
MMP sensitive liposomes
Doxorubicin
Sonopermeation

ABSTRACT

To improve therapeutic efficacy of nanocarrier drug delivery systems, it is essential to improve their uptake and penetration in tumour tissue, enhance cellular uptake and ensure efficient drug release at the tumour site. Here we introduce a tumour targeting drug delivery system based on the ultrasound-mediated delivery of enzyme sensitive liposomes. These enzyme sensitive liposomes are coated with cleavable poly(ethylene glycol) (PEG) which will be cleaved by two members of the enzyme matrix metalloproteinase family (MMP-2 and MMP-9). Cleavage of the PEG coat can increase cellular uptake and will destabilize the liposomal membrane which can result in accelerated drug release. The main aim of the work was to study the effect of focused ultrasound and microbubbles on the delivery and therapeutic efficacy of the MMP sensitive liposome. The performance of the MMP sensitive liposome was compared to a non-MMP sensitive version and Doxil-like liposomes. *In vitro,* the cellular uptake and cytotoxicity of the liposomes were studied, while *in vivo* the effect of ultrasound and microbubbles on the tumour accumulation, biodistribution, microdistribution, and therapeutic efficacy were investigated. For all tested liposomes, ultrasound and microbubble treatment resulted in an improved tumour accumulation, increased extravasation, and increased penetration of the liposomes from blood vessels into the extracellular matrix. Surprisingly, penetration depth was independent of the ultrasound intensity used. Ultrasound-mediated delivery of free doxorubicin and the Doxil-like and MMP sensitive liposome resulted in a significant reduction in tumour volume 28 days post the first treatment and increased median survival. The MMP sensitive liposome showed better therapeutic efficacy than the non-MMP sensitive version indicating that cleaving the PEG-layer is important. However, the Doxil-like liposome outcompeted the MMP and non-MMP sensitive liposome, both with and without the use of ultrasound and microbubbles.

1. Introduction

Successful treatment of cancer remains a challenge for many solid tumour types. Conventional chemotherapy is used alone or in combination with other treatment modalities and is based on systemic administration of drugs which often lacks cancer specificity, causing severe side-effects. Furthermore, because of high accumulation in healthy tissue and fast clearance rate of the small drug molecules, only a small fraction of the injected dose (0.001–0.01%) reaches the tumour site [1,2]. Therefore, new strategies are needed to obtain successful therapeutic response.

Drug loaded nanoparticles (NPs) have shown great potential as a more specific anti-tumour treatment being able to exploit the enhanced permeability and retention (EPR) effect in cancerous tissue and thereby improving the delivery of drugs to tumours and reducing toxic effects towards normal tissue [3,4]. Tumour tissue lacks lymphatic drainage and due to uncontrolled growth of tumours, endothelial cells are poorly aligned and have large fenestrations, resulting in leaky vasculature. These anatomical irregularities result in leakage and accumulation of components from the blood plasma into tumour tissue, which makes the

* Corresponding author.
E-mail address: marieke.olsman@ntnu.no (M. Olsman).

https://doi.org/10.1016/j.jconrel.2020.06.024
Received 10 February 2020; Received in revised form 18 June 2020; Accepted 22 June 2020
Available online 02 July 2020

EPR an interesting target for a more tumour specific therapy strategy [3,5]. NPs have numerous other advantages over conventional therapeutics such as less accumulation in healthy tissue and the possibility for actively targeted delivery by adding targeting ligands to the NP surface, in addition to protecting the drug from premature degradation, reviving potentially poorly soluble drugs, controlled and sustained drug release, and different pharmacokinetics and biodistribution compared to small molecule drugs [6]. However, despite these promising features, their therapeutic effect has been limited, partly by inadequate delivery due to the heterogeneous EPR-effect, dense extracellular matrix, and high interstitial fluid pressure in tumours [7–10].

Several preclinical studies have shown that ultrasound in combination with microbubbles improves the delivery, intratumoural distribution and therapeutic efficacy of drug loaded NPs in tumours [11–16]. The improved therapeutic efficacy of chemotherapeutics after ultrasound-mediated delivery has also been demonstrated in patients with non-resectable pancreatic tumours and patients suffering from glioblastoma [17,18]. In the acoustic field, the microbubbles expand and compress during the low and high pressure phases, respectively. This cavitation behaviour is known to increase the vascular permeability since the oscillating and collapsing microbubbles form mechanical stresses on the blood vessel wall which can create both transient and permanent pores or even more extensive vascular damage [19–21]. Furthermore, it has been shown that the use of focused ultrasound in combination with microbubbles can enhance endocytosis *in vitro* [19,22]. All these ultrasound-mediated effects, also known as sonopermeation, will increase vascular permeability and thereby increase extravasation and potentially improve penetration through the extracellular matrix which could result in enhanced accumulation and distribution of NPs and drug in tumour tissue [23].

Several NP-based drug delivery systems have been developed including polymeric, liposomal, viral and inorganic NPs [6]. These NPs are often coated with polyethylene glycol (PEG) to shield them from the immune system and thereby extending their circulation half-life significantly compared to non-PEGylated NPs and small drug molecules, resulting in an increased accumulation in tumour tissue [24]. In addition, PEGylation prevents aggregation of the NPs, and can have a charge shielding effect resulting in a more neutral charge of the NP, which may improve penetration through the extracellular matrix due to reduced electrostatic interactions with extracellular matrix components [25–27]. However, the presence of PEG on the surface of the NPs will also affect the NP-cell interaction, resulting in reduced cellular uptake and thereby potentially reducing the therapeutic efficacy [28,29].

To improve therapeutic outcome of current drug delivery systems, it is essential to improve the delivery of drug carriers to and throughout tumour tissue, enhance cellular uptake and ensure secure and efficient drug release at the tumour site. In the present work, we introduce a dual tumour targeting drug delivery system based on ultrasound-mediated delivery of matrix metalloproteinase (MMP) sensitive liposomes coated with PEG. Once delivered to the extracellular matrix of the tumour, the PEG coat will be cleaved by two members of the enzyme MMP family (MMP-2 and MMP-9) which are overexpressed in several cancer types [30]. The cleaving is expected to improve the interaction between liposomes and tumour cells compared to PEGylated liposomes [28,29]. Furthermore, removal of the PEG coating can result in accelerated drug release [29]. Based on the MMP sensitive liposome characteristics and the potentially improved delivery to the tumour site using ultrasound in the presence of microbubbles, it is hypothesized that this combination will enhance therapeutic efficacy.

The main aim of the work was to study the effect of focused ultrasound in combination with microbubbles on the delivery and therapeutic efficacy of the MMP sensitive liposome. The performance of the MMP sensitive liposome (Cleavable) was compared to a non-MMP sensitive version (NonCleavable) and a liposomal formulation the same as the clinically used formulation Doxil®/Caelyx® (Doxil-like). First, cellular uptake and cytotoxicity were studied *in vitro* by flow cytometry and a cell viability assay, respectively. Secondly, the effect of different ultrasound settings on liposome uptake in tumours and normal organs in mice was studied using a small animal optical imager, and the effect on microdistribution in tumours was evaluated with confocal laser scanning microscopy. Thirdly, the therapeutic efficacy of the drug loaded liposomes was evaluated by measuring the growth of subcutaneous tumours.

2. Material and methods

2.1. Peptide synthesis

The PEGylated cleavable lipopeptide (PCL) was synthesized as follows: The peptide H-Gly-Trp(Boc)-Ile-Pro-Val-Ser(tBu)-Leu-Arg-(Pbf)-Ser(tBu)-Gly-Glu(tBu)-Glu(tBu)-Glu(tBu)-Glu(tBu)-PEG_{2000} was synthesized on an Initiator Alstra peptide synthesizer (Biotage, Sweden) using a TentaGel PAP_{2000} resin. The resin was swelled in dichloromethane (DCM) for 1 hour. In general, couplings were carried out for 5 minutes at 75 °C using 4 equiv. amino acid, 3.92 equiv. HATU and 8 equiv. 2,4,6-collidine in N,N-Dimethylmethanamide (DMF). Ile and Leu were coupled twice to ensure conversion. The second coupling was carried out for 30 minutes at room temperature. Also, Arg was coupled for 30 minutes at room temperature. Ile, Val and Leu were coupled in N-methylpyrrolidone (NMP). Fmoc deprotection was performed using 20% piperidine in DMF for 10 minutes. The peptide was cleaved for 3 hours using 95:2.5:2.5 trifluoroacetic acid (TFA)/triisopropyl silane/water after which the cleavage solvent was removed under reduced pressure and the peptide precipitated in diethyl ether. The cleaved peptide was dissolved in 500:500:1 water/acetonitrile/triethylamine (TEA) and lyophilized. The peptide was hereafter dissolved in NMP and dried over molecular sieves in 3 mM concentration. 1.2 equiv. cholesteryl chloroformate and 20 equiv. diisopropylethylamine were added to the dissolved peptide and the solution was stirred. After 30 min the concentration was diluted to 10% NMP with water and purified using semipreparative high performance liquid chromatography (HPLC), which was operated using a Waters 600 pump and controller, a Waters 2489 UV/Vis detector and a Waters XTerra C18 5 μm column (30 × 250 mm). For lipopeptide elution, the following eluents were used: Eluent (A) 5% acetonitrile, 0.1% TEA in water, Eluent (B) 0.1% TEA in acetonitrile. A linear gradient was used for elution of the lipopeptide as a narrow peak with retention time (Rt) from 18-20 min was obtained. The lipopeptide was lyophilized to give a white powder. The purity of the compound was monitored by analytical HPLC using a Waters XTerra C8 (4.6 × 150 mm) column. Eluent (A) was 5% acetonitrile, 0.1% TFA and Eluent (B) 0.1% TFA in acetonitrile. A linear gradient from 0 to 100% eluent (B) over 15 min with flow rate 1 ml/min was used. The purity was >96% and Rt 11.8 min. Molecular weight was confirmed by use of MALDI-TOF MS (Bruker Reflex, Bruker Daltonics, USA) observed ($M+H^+$) 3983.9.

2.2. Liposome formulation and characterization

1-palmitoyl-2-oleoyl-glycero-3-phosphocholine (POPC) and ovine cholesterol (Chol) were purchased from Avanti Polar Lipids Inc. (USA). Methoxy(polyethylene glycol)-2000-Cholesterol (mPEG2000-Chol) was from Creative PEGWorks (USA). Stealth premix consisting of hydrogenated Soy-L-α-phosphatidylcholine (HSPC), hydrogenated 1,2-distearoyl-sn-glycero-3-phosphoethanolamine-N-[methoxy(polyethylene glycol)-2000] (mPEG2000-DSPE) and cholesterol in a weight ratio of 3:1:1: was purchased from Lipoid GmbH (Germany). To fluorescently label the liposomes, 1,2-dioleoyl-*sn*-glycero-3-phospho-ethanolamine-Atto488 (DOPE-Atto488) and 1,2-dipalmitoyl-*sn*-glycero-3-phosphoethanolamine-Atto700 (DPPE-Atto700) were used (ATTO-TEC GmbH, Germany). The PEGylated cleavable lipopeptide was fabricated in house as described in the previous section.

Liposomes were prepared using the molar compositions outlined in

Table 1
Molar compositions [%] of the three different liposomes.

	Fluorophore labelled liposomes			Drug loaded liposomes		
	Doxil-like	NonCleavable	Cleavable	Doxil-like	NonCleavable	Cleavable
POPC		59.6	59.6		60	60
HSPC	56.2			56.5		
Chol	38.1	35	35	38.2	35	35
MPEG2000-DSPE	5.3			5.3		
MPEG2000-CHOL		5			5	
PCL			5			5
DOPE-Atto488	0.2	0.2	0.2			
DPPE-Atto700	0.2	0.2	0.2			

Abbreviations: POPC – 1-palmitoyl-2-oleoyl-*sn*-glycero-3-phosphocoline, HSPC – Hydrogenated soy 3-phosphocoline, CHOL – Cholesterol, DSPE – 1,2-Distearoyl-*sn*-glycero-3phosphoetanolamine, PEG2k – Polyethylene glycol, PCL – PEGylated cleavable lipopeptide, DOPE-Atto488 – 1,2-Dioleoyl-*sn*-glycero-3-phosphoethanolamine-Atto488, DPPE-Atto700 – 1,2-Dipalmitoyl-*sn*-glycero-3-phosphoethanolamine-Atto700.

Table 1. Appropriate amounts of the phospholipids were dissolved in a mixture of t-Butanol:water (9:1), which was snap-frozen in liquid nitrogen and lyophilized overnight. The following day the thin lipid layer was hydrated in a 10 mM HEPES 140 mM NaCl buffer or 250 mM ammonium sulfate buffer (fluorophore labelled liposomes or doxorubicin loaded liposomes respectively) and extruded by passing the multilamellar vesicles through 100 nm polycarbonate filters to form unilamellar vesicles. The temperature was kept at 40 °C for unsaturated formulations (NonCleavable and Cleavable) and 65 °C for saturated formulations (Doxil-like) throughout the hydration and extrusion process. Liposomes hydrated with ammonium sulfate were dialyzed using Slize-A-Lyzer cassettes (ThermoFisher, USA), pore size 10 kD versus a 10 mM HEPES 140 mM NaCl buffer. Subsequently, the dialyzed liposomes were remote loaded with doxorubicin HCl (Lianyungang Guivuan Chempharm Co., China) for 3 hours at 45 °C (unsaturated liposomes) or 60 °C (saturated liposomes), at a drug-to-lipid ratio of 1:5. Unencapsulated doxorubicin was removed by dialyzing the liposomes using Slide-A-Lyzer dialysis cassettes (MWCO 10kD) versus HEPES saline buffer (10 mM HEPES, 140 mM NaCl, pH7.4). The PEG cleavable lipopeptide was post inserted to the corresponding formulations at 40 °C for 45 min.

The phosphor content of the liposomes was quantified using Inductive Coupled Plasma Mass Spectroscopy (ICP-MS), employing gallium as internal standard, while the doxorubicin content of the liposomes was quantified spectrophotometrically by measuring sample absorption at 496 nm (Tecan Spark plate reader, Tecan Trading, Switzerland). The hydrodynamic radius, polydispersity index (PDI) and zeta potential of the liposomes were investigated using a Zetasizer ZS (Malvern Panalytical Ltd., UK). The liposomes were diluted to 100 μM using HEPES saline buffer (10 mM HEPES, 140 mM NaCl) for DLS measurements and 10 mM HEPES 5% w/v glucose for zeta potential measurements.

Phospholipids labelled with Atto488 and Atto700 (see Table 1) were incorporated in the liposomes to measure the microdistribution and tissue uptake of liposomes, respectively. The fluorescence intensity of the three liposomes was compared by measuring the fluorescence intensity of Atto488 and Atto700 in dilution series of the liposomes using a spectrofluorometer (SpectraMax i3x, Molecular Devices, USA) and a small animal optical imager (Pearl Impulse imager, LI-COR Biosciences Ltd., USA). Results from the dilution series measured by the small animal optical imager were compared to *in vivo* fluorescence intensity measurements. For the spectrofluorometer experiments, the liposome solutions were excited with 480 ± 9 nm and 680 ± 9 nm and emissions were detected at 505 ± 20 nm and 705 ± 20 nm, for respectively Atto488 and Atto700. For experiments with the small animal optical imager, the Atto700-liposomal solutions were excited with 685 nm and fluorescence emission was detected at 720 nm.

2.3. In vitro cleavage of the MMP sensitive liposomes

The protease thermolysin has the same substrate specificity as MMP-2 and MMP-9, and is therefore suitable for cleavage of the liposomes *in vitro* [31]. 20 μl of liposomes were mixed with 6 μg/ml thermolysin in 180 μl of enzyme activation buffer which consists of HEPES-buffered saline (50 mM HEPES, 100 mM NaCl, pH 7.4) supplemented with 1 mM $CaCL_2$ and 2 μM $ZnCl_2$. All chemicals were purchased at Sigma-Aldrich (USA). The cleavage was performed over night at 37 °C.

2.4. Cell culture

Prostate adenocarcinoma cells (PC3, ATCC, USA) were cultured in Dulbecco's modified Eagle medium (Sigma-Aldrich, USA) with 10% fetal bovine serum (Sigma-Aldrich, USA). Cells were kept at 37 °C and 5% CO_2 and maintained in exponential growth. 1% penicillin/streptomycin (Sigma-Aldrich, USA) was added to the growth medium of cells implanted in mice and the *in vitro* cytotoxicity study.

2.5. Cellular uptake of liposomes

50 000 PC3 cells/well were seeded in 24-well plates (VWR, USA). Seventy-two hours post seeding, cells were incubated with 50 μg/ml of doxorubicin loaded liposomes (Doxil-like, NonCleavable, Cleavable) for 4 hours at 37 °C and 5% CO_2 before washing 3 times with PBS, trypsinizing (Sigma-Aldrich, USA) and placing the cell suspension on ice until flow cytometry analysis. To study the effect of cleavage of the Cleavable liposome on the cellular uptake, both the intact and cleaved version (thermolysin treated) of the Cleavable liposome were included. To evaluate if any dye leakage (doxorubicin) occurred, cells were incubated with 50 μg/ml of doxorubicin loaded liposome solution for 4 hours at 4 °C. No endocytosis is expected at this temperature such that stained cells are most likely stained due to free drug [32].

Liposomal uptake was evaluated by flow cytometry (Gallios, Beckman Coulter, USA). A 488 nm laser was used for excitation of doxorubicin and emission was detected at 585 ± 15 nm. Gating on the side versus forward scatter plot was applied to exclude dead cells, debris and cell aggregates. Kaluza Flow Cytometry analysis software v1.3 (Beckman Coulter, USA) was used to determine the percentage of fluorescent cells and mean fluorescence intensity corresponding to cellular uptake of liposomes.

2.6. In vitro cytotoxicity study

The metabolic assay based on AlamarBlue was used to measure cell viability. 10 000 PC3 cells/well were seeded in a black 96 well plate with transparent bottom (Corning Inc., Sigma-Aldrich, USA). Twenty-four hours after seeding, cells were incubated with either the drug loaded liposomes or free doxorubicin (Accord Healthcare, UK) for 24

hours at 37 °C with 5% CO_2. For both free and encapsulated doxorubicin, concentrations between 0.001 μg/ml and 100 μg/ml, were used. After treatment, cells were rinsed 3 times with growth medium. The growth medium was replaced by 100 μl of AlamarBlue (1:10 dilution in growth medium) (Thermo Fisher Scientific, USA) 24 hours later, and incubated for 3 hours. Fluorescence was measured with a spectrofluorometer (SpectraMax i3x, Molecular Devices, USA) with excitation at 560 nm and detection of emission at 590 nm. Cell viability was calculated by dividing the fluorescence intensity of the treated wells by the fluorescence intensity of wells with untreated cells. A four-parameter logistic curve was fitted to the datapoints with SigmaPlot (v14.0, Systat Software Inc., USA).

2.7. Animals and tumour inoculation

Female Balb/c nude mice (Janvier labs, France) were purchased at 8 weeks of age. Mice were housed in groups of 5 in individually ventilated cages under conditions free of specific pathogens at a 12-hour night/day cycle. Cages were kept in a controlled environment (20–23 °C, humidity of 50–60%) and the mice had free access to food and sterile water. They were fed RM1 expanded pellets (Special Diets Services, UK), and the cages were enriched with housing, nesting material and gnaw sticks. All experimental procedures were approved by the Norwegian Food Safety Authority.

Before tumour implantation, mice were anesthetized with 2–3% isoflurane. 50 μl of medium containing $3x10^6$ PC3 cells was slowly injected subcutaneously between the hip and the knee on the lateral side of the left hind leg. Tumours were measured with a calliper 3 times per week and the weight of the animals was closely monitored. Tumour volume was calculated by $l * w^2 * \frac{\pi}{6}$, where l and w are the length and width of the tumour, respectively.

Before ultrasound experiments, mice were anesthetized by a subcutaneous injection (0.1 ml/10 g of bodyweight) of fentanyl (0.05 mg/kg, Actavis Group, USA), medetomidine (0.5 mg/kg, Orion Pharma, Finland), midazolam (5 mg/kg, Accord Healthcare, UK) and water (2:1:2:5). Thereafter a catheter was placed in the lateral tail vein. In case needed, a subcutaneous injection (0.1 ml/10 g of body weight) of atipemazol (2.5 mg/kg, Orion Pharma, Finland), flumazenil (0.5 mg/kg, Fresenius Kab, USA) and water (1:1:8) was used as antidote. The mice received a subcutaneous injection of 0.5 ml saline before waking up to counteract the incurred dehydration. Body temperature was maintained by external heating and eyes were kept moist with Viscotears Liquid Gel (Alcon, USA). After treatment, the animals were placed in a recovery rack (28 °C) until the next morning to recover from the anaesthesia and avoid hypothermia. At the end of experiments, the anesthetized mice were euthanized by cervical dislocation.

2.8. Ultrasound set-up, microbubbles and passive cavitation detection

A custom-made single element focused transducer (Imasonic, France) with a centre frequency of 1.0 MHz was mounted on the bottom of a water tank (see Fig. 1). The transducer had a diameter of 50 mm and a focal distance of 125 mm. Signals were generated with a signal generator (33500B, Agilent Technologies, USA) and amplified with a 50 dB RF amplifier (2100L, E&I, USA).

Animals were placed on top of the lid of the tank and the tumour bearing leg was positioned through a circular hole in the lid and in the far field of the ultrasound transducer at a distance of approximately 190 mm. The 3 dB and 6 dB beam widths at 190 mm distance are 6 and 10 mm, respectively, thereby exposing the whole tumour. The waterside of the lid was covered with acoustic absorber material to avoid standing waves. To avoid hypothermia of the animal, water in the tank was heated to 32 °C and a heating lamp was placed above the mouse. Animals exposed to ultrasound received a 100 μl bolus injection of SonoVue™ microbubbles (Bracco Imaging, Italy) directly after an intravenous bolus injection of liposomes, after which ultrasound treatment was started within 5 seconds.

The *in vivo* cavitation behaviour of the SonoVue™ microbubbles was detected with a 5.0 MHz unfocused transducer (Harisonic, 0.75 inch diameter, 17-0512-P, Olympus, USA) which was placed in a custom-made holder in the corner of the tank facing the tumour leg. The detected backscatter signal was recorded by an oscilloscope (LeCroy WaveRunner 44Xs, LeCroy corporation, USA) with a sampling frequency of 100 MS/s and transferred to a PC for processing in Matlab (version R2018A, Mathworks Inc, USA). The frequency content of the signals was calculated and displayed real time, enabling visual inspection of an expected increase in harmonic signals (stable cavitation) and broadband level rise (inertial cavitation).

2.9. Ultrasound-mediated delivery of the three liposomes

Subcutaneous prostate cancer tumours were grown in 40 mice, and mice were included when the tumours had reached an average size of 200–300 mm^3. For each type of liposome, the animals were randomly divided into 3 treatment groups (Table 2).

Each animal received an 100 μl intravenous bolus injection of 6 mM of liposome solution. Mice exposed to ultrasound, received 100 μl of SonoVue™ microbubbles followed with 2 minutes of ultrasound with either a mechanical index (MI) of 0.4 or 0.8 (0.4 or 0.8 MPa peak negative pressure), with ultrasound pulses of 10 000 cycles and pulse repetition frequency of 0.5 Hz.

Three hours post injection of liposomes, functional blood vessels were stained by injecting 100 μl of lectin (*Ulex europaeus*-Atto 594 conjugate, Sigma-Aldrich, USA) which was allowed to circulate for 5 min before euthanizing the animal.

2.10. Tumour accumulation and biodistribution of liposomes – Small animal optical imager

Tumour accumulation of the liposomes was obtained by imaging animals with a small animal optical imager (Pearl Impulse imager, LI-COR Biosciences Ltd., USA) at different timepoints post treatment. The Atto700 dye in the liposomes was excited at 685 nm and emission was detected at 720 nm. In addition to the fluorescence image, a bright field

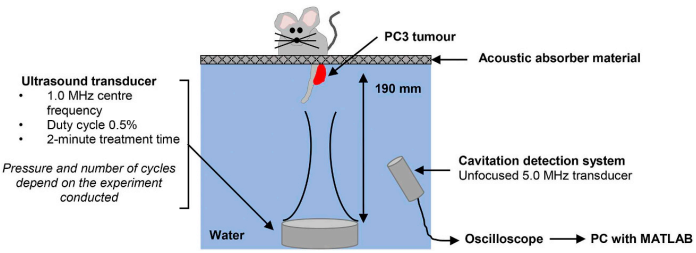

Fig. 1. Schematic illustration of the ultrasound set up.

Table 2
Treatment groups to study the effect of ultrasound and microbubbles on tumour accumulation, biodistribution and microdistribution of the three liposomes. (D = Doxil-like, NC = NonCleavable, C = Cleavable).

Group	Liposome	Mechanical index	Number of cycles	Pulse repetition frequency [Hz]	Treatment time [min]	Number of mice
1	D	–	–	–	–	3
2	D	0.4	10 000	0.5	2.0	5
3	D	0.8	10 000	0.5	2.0	5
4	NC	–	–	–	–	3
5	NC	0.4	10 000	0.5	2.0	5
6	NC	0.8	10 000	0.5	2.0	5
7	C	–	–	–	–	4
8	C	0.4	10 000	0.5	2.0	5
9	C	0.8	10 000	0.5	2.0	5

image of the animal was recorded. At each timepoint, a region of interest (ROI) around the tumour was drawn on the bright field image, transferred to the fluorescence image and the average fluorescence intensity of the ROI was obtained. The tumour fluorescence intensity as a function of time was normalized to the fluorescence intensity at t = 0 (first recorded image approximately 5 minutes after injection of the liposomes).

The biodistribution of NPs was obtained by excising the spleen, kidneys, liver, lungs, heart and tumour. Both a fluorescence and a bright field image of the organs were obtained. An ROI was drawn around each organ and the total fluorescence intensity was normalized by the wet weight of the organ or tumour. The fluorescence intensity per gram of tissue was plotted per liposome and treatment group. Fluorescence intensity values for the biodistribution were corrected based on the observed differences in fluorescence intensity of the Atto700 between the three liposomes.

2.11. Microdistribution – Confocal imaging of tumour sections

Excised tumours were cut along the coronal plane. One half was mounted with the cutting plane down on a piece of cork and covered with OCT Tissue Tek (Sakura, The Netherlands) before submerging the sample in liquid nitrogen and storing at −80 °C. The other half was fixed in 4% paraformaldehyde for histological evaluation.

Of the frozen tissue samples, the first 1000 μm was removed after which 4 sections of 25 μm thickness for confocal imaging and 1 section of 4 μm thickness for histological evaluation were taken. These 5 sections were made at 5 different levels in the tumour, separated by 300 μm.

Microdistribution of the liposomes was imaged by confocal laser scanning microscopy (CLSM). Prior to imaging, the section was thawed at room temperature, mounted with Vectashield containing DAPI (Vector Laboratories, USA), covered with a cover glass and sealed with nail polish. The DAPI staining was used to distinguish between tumour and healthy tissue. All sections were imaged with a Leica TCS SP8 confocal microscope equipped with a white light laser (Leica Microsystems, Germany) and a multiphoton laser (Chameleon Vision-S, Coherent, USA) and using a 40X/1.10 water objective. DAPI was excited with the multiphoton laser at 730 nm and emission was detected at 400–450 nm. Sequentially, the Atto488 in the liposomes and the Atto594 from the blood vessel staining were excited with a white light laser at 500 and 600 nm, respectively. Fluorescence of these two dyes was detected at 515–555 nm and 615–655 nm, respectively. An optical section of 4 μm was used and the laser intensity and detector gain were kept the same for all sections.

Sections were inspected through the ocular by viewing only the blood vessel channel and images were taken whenever stained blood vessels were found without knowing whether liposomes were present or not. From each treatment group, sections at three different levels from the tumour of three animals per treatment group were imaged resulting in 80–110 images per treatment group (approximately 7–14 images per section).

2.12. Microdistribution – Quantification of extravasation

Images taken with the CLSM (see Supplementary Fig. S1A) were processed and analysed in ImageJ and MATLAB (version R2018A, Mathworks Inc, USA). The blood vessel and liposome images were thresholded based on the ImageJ built-in threshold 'Triangle' (see Supplementary Fig. S1B). From the thresholded blood vessel channel, a distance map image was calculated in which the intensity of each pixel represents the distance of that specific pixel to the nearest blood vessel pixel in number of pixels (see Fig. S1C). This distance map image was multiplied pixel by pixel with the thresholded binary liposome image resulting in a distance map image for just the pixels representing extravascular liposomes (see Fig. S1D). From each image a histogram was created to assess the distance travelled by the liposomes and the distance travelled was converted from number of pixels to micrometre (1 pixel = 0.6 μm) (see Fig. S1E).

Several histograms showed small but clear peaks at distances far from the blood vessel wall. It is expected that these peaks are caused by liposomes from blood vessels that were above or below the imaged plane or blood vessels that were not functional at the time the lectin was circulating, and these peaks were excluded. Thereafter, the average number of pixels at each distance from the blood vessel of the whole dataset was calculated and plotted per liposome and treatment group.

2.13. Therapeutic efficacy study

Mice were included in the therapeutic efficacy study once the tumours had reached a size of 100–200 mm^3, 3–4 weeks after inoculation. A total of 55 mice were randomly distributed in the nine different treatment groups (see Table 3).

Untreated control animals received a sham saline injection of 200 μl. Mice getting treatment received a doxorubicin dose of 6 mg/kg by intravenously injecting either the doxorubicin loaded liposomes or the free drug doxorubicin (Doxorubicin Hydrochloride, Accord

Table 3
The nine treatment groups during the therapeutic efficacy study. (FUS = Focused ultrasound treatment in the presence of microbubbles).

	Abbreviation		Number of mice	
Treatment	**−FUS**	**+FUS**	**−FUS**	**+FUS**
Saline	Saline	–	7	–
Doxil-like	D	D + FUS	7	5
NonCleavable	NC	NC + FUS	6	6
Cleavable	C	C + FUS	5	6
Doxorubicin	DOX	DOX + FUS	6	7

Healthcare, UK). Groups not exposed to ultrasound and microbubbles (-FUS), received a 100 μl sham saline injection while groups exposed to ultrasound received 100 μl SonoVue™ microbubbles followed by an ultrasound treatment with an MI of 0.8 and pulses with 10 000 cycles (+FUS). Animals received this treatment once a week for three consecutive weeks (day 0, 7 and 14).

Tumour sizes were measured with a calliper three times a week and the weight of the animals was closely monitored. Mice were euthanized when the tumour length exceeded 15 mm. Animals that showed a reduced tumour growth with respect to the saline group for at least 7 consecutive days were defined as responders.

2.14. Statistical analysis

Statistical analysis on all datasets was performed with Sigmaplot (v14.0, Systat Software Inc., USA). Datasets were first tested for normality and equal variance with the Shapiro-Wilk test and Brown-Forsythe test, respectively. If the dataset passed for both tests, a t-test was performed to test for statistical significance between two treatment groups. Otherwise a Mann-Whitney rank sum test was used to assess statistical significance between datasets. A p-value smaller than 0.05 was considered to indicate statistical significance.

3. Results

3.1. Characterization of liposomes

Characteristics such as size, polydispersity index (PDI), zeta potential and loading of doxorubicin are shown in Table 4. A circulation half-life time of 2.9, 4.0 and 3.2 hours were observed for the Doxil-like, NonCleavable and Cleavable liposome, respectively (see Table S1 and Fig. S2). Different batches of the liposomes were used for the *in vitro* and *in vivo* experiments.

The effect of thermolysin on size, PDI and zeta potential of the three liposomes has been studied (Supplementary Fig. S3). Small differences in size or zeta potential between the liposomes were found.

The fluorescence intensity of the Atto700 dye were measured by the small animal optical imager of liposomes in solution and *in vivo* in the non-tumour bearing leg, and shown in Supplementary Fig. S4A and B, respectively. A large difference in fluorescence intensity between the three types of liposomes was observed. The NonCleavable liposomes showed fluorescence intensities that were approximately 3.7x and 1.9x higher than those of the Doxil-like and Cleavable liposomes, respectively. The differences observed in solution corresponded well with the *in vivo* data obtained 5 minutes after injection of the liposomes. The fluorescence intensity of the Atto488 and Atto700 was also measured with a spectrofluorometer (Supplementary Fig. S5) and corresponded to Fig. S4.

3.2. Cellular uptake and in vitro cytotoxicity of doxorubicin loaded liposomes

The uptake of the liposomes by PC3 cells after 4 hours of incubation at 37 °C was evaluated by flow cytometry and the results are shown in Fig. 2A. 90% of the cells had taken up the NonCleavable liposome, followed by the Cleavable and Doxil-like liposomes with 68% and 26% of cellular uptake, respectively. The mean fluorescence intensity of the cells incubated with liposomes increased by a factor of 3.9x to 5.5x with respect to untreated autofluorescence values (see Fig. 2B). Both the cellular uptake (%) and the mean fluorescence intensity increase were significantly different from autofluorescence and between the different liposomes. Incubating at 4 °C for 4 hours did not result in any cellular uptake of the liposomes while free drug doxorubicin showed clear uptake. This indicates that there was no free drug (doxorubicin) in the liposomal solutions (data not shown).

The *in vitro* toxicity of the three doxorubicin loaded liposomes and free doxorubicin are shown in Fig. 2C. A reduction in cell viability was observed for increasing concentrations of encapsulated and free drug. For most of the concentrations tested, the NonCleavable and Cleavable liposomes showed a similar effect on the cell viability as free doxorubicin. A higher concentration of the Doxil-like liposome was needed to reduce cell viability.

The effect of cleavage of the PEG-layer of the Cleavable liposome on the cellular uptake has been studied (Supplementary Fig. S6). The figure shows that the enzyme activation buffer without the enzyme added to the growth medium reduced the cellular uptake from 68% for the Cleavable liposome in just growth medium to 38%. Adding the enzyme thermolysin significantly increased the cellular uptake to 55%. A reduced cellular uptake of the NonCleavable liposome was observed after adding the activation buffer without the enzyme. Adding the enzyme had no effect on the cellular uptake. The cellular uptake of the Doxil-like was not affected by neither adding the buffer nor the buffer and the enzyme.

3.3. Ultrasound-mediated tumour accumulation of fluorophore labelled liposomes

The effect of ultrasound and microbubbles on tumour accumulation of the three fluorophore labelled liposomes is shown in Fig. 3. Ultrasound settings used were based on the previous obtained results showing large tumour accumulation of the liposomes using an MI of 0.8 with pulses of 10 000 cycles and intermediate tumour accumulation of

Table 4
The average diameter, ς-potential and PDI for the fluorophore labelled and doxorubicin loaded liposomes. Different batches of the liposomes were used for the *in vitro*, *in vivo* tumour accumulation and therapeutic efficacy study.

Doxorubicin Loaded - *Cellular uptake + cytotoxicity*	**Diameter [nm]**	**ς-potential [mV]**	**PDI**	**Dox to lipid ratio [μmol dox/μmol lipid]**
Doxil-like	128	−14.6 ± 0.9	0.063 ± 0.009	0.23
NonCleavable	123	−11.4 ± 0.4	0.054 ± 0.008	0.24
Cleavable	140	−17.6 ± 0.6	0.059 ± 0.025	0.24
Fluorophore Labelled - *Microdistribution + Biodistribution*				
Doxil-like	126	−13.4 ± 0.5	0.035 ± 0.007	-
NonCleavable	155	−3.8 ± 1.2	0.102 ± 0.020	-
Cleavable	160	−13.7 ± 1.2	0.044 ± 0.015	-
Doxorubicin Loaded - *Therapeutic efficacy study*				
Doxil-like	105	−5.4 ± 0.5	0.055 ± 0.019	0.20
NonCleavable	94	−5.5 ± 0.1	0.081 ± 0.007	0.24
Cleavable	127	−12.7 ± 0.2	0.068 ± 0.020	0.27

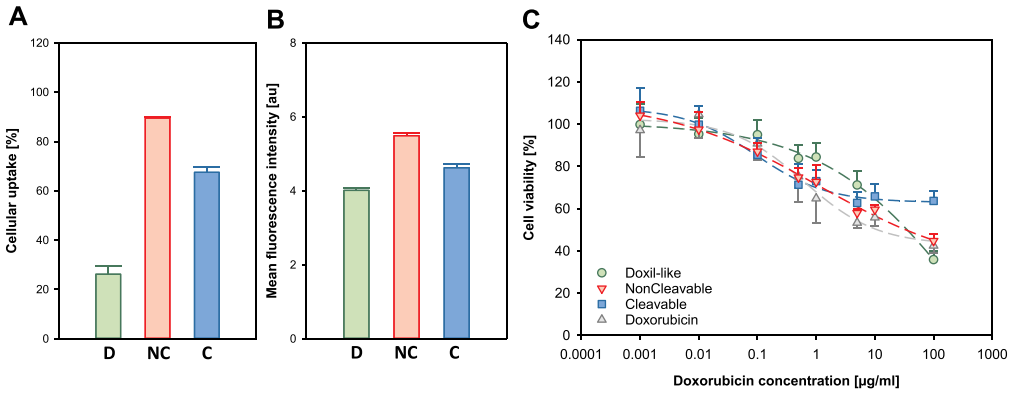

Fig. 2. (A) Cellular uptake of liposomes in percentage and (B) mean fluorescence intensity normalized to autofluorescence after 4 hours of incubation. Mean and standard deviation are based on the averages of n = 3 experiments (three replicates each). (D = Doxil-like, NC = NonCleavable, C = Cleavable) (C) Cytotoxicity of the drug loaded liposomes and free drug doxorubicin for PC3 cells after incubation of 24 hours at 37 °C and a recovery time of 24 hours before applying the AlamarBlue assay. A four-parameter logistic curve was fitted to the datapoints. Mean and standard deviation are based on the averages of n = 3 experiments (three replicates each).

the liposomes using MI = 0.4 with 10 000 cycles (Supplementary Fig. S7).

Representative images taken at t = 0 (approx. 5 minutes after treatment) and t = 3 hours post injection of the Cleavable liposomes with and without ultrasound treatment are shown in Fig. 3A. The fluorescence intensity relative to fluorescence intensity at t = 0 of the tumour ROI as function of time are shown in Fig. 3B–D. Ultrasound and microbubbles increased the tumour uptake of all liposomes, but to different extents. A statistically significant increase in relative fluorescence intensity could be observed at all timepoints (t > 0). All ultrasound-treated groups reached their maximum intensity at 0.5 hours post injection of the liposomes. The increase in relative fluorescence intensity was most profound for the NonCleavable liposome of which the groups treated with an MI of 0.4 and 0.8 reached average peak values of 1.7 and 2.2, respectively. The Doxil-like and Cleavable liposome responded similarly and the MI = 0.4 and MI = 0.8 ultrasound treatment groups reached a maximum relative fluorescence intensity of 1.2–1.3 and 1.5, respectively.

Three hours post injection, the tumour accumulation of all liposomes was reduced (Fig. 3D), but the ultrasound treated groups still had higher fluorescence intensity than the corresponding groups without ultrasound treatment (Only-LPs). Even though the NonCleavable liposome showed the highest increase of relative fluorescence intensity at 0.5 hours post injection, at 3 hours post injection, the relative fluorescence intensity values of the MI = 0.8 group differed minimally from the other two MI = 0.8 groups. The Only-LPs and MI = 0.4 group of the NonCleavable liposome showed lower values than the Doxil-like and Cleavable liposome. The relative fluorescence intensity readings of the groups treated with ultrasound in combination with the Doxil-like or Cleavable liposome reached similar values at 3 hours post injection and treatment. The decrease of fluorescence intensity over time is expected to be due to elimination of the liposomes from the circulation and by liposome clearance in the tumour.

3.4. Biodistribution of liposomes

Fig. 4 shows the biodistribution of the three liposomes in the different treatment groups. Fluorescence intensity per gram of tissue is displayed for the various organs and tumour. Here, the fluorescence intensity has been corrected based on fluorescence intensity differences of the Atto700 dye between the three different types of liposomes.

The Doxil-like and Cleavable liposome showed a similar biodistribution profile in the various organs, while the NonCleavable liposome showed lower fluorescence intensity values for most organs. Furthermore, highest fluorescence intensities for all three liposomes were observed in the lungs followed by the spleen, liver, kidneys and heart.

An increase in fluorescence intensity in the tumour could be observed when ultrasound and microbubbles were used in combination with the liposomes. The effect of ultrasound and microbubbles seemed to be minimal for the Doxil-like liposome. Only the MI = 0.8 group of the NonCleavable liposome showed a statistically significant increase with respect to the Only-LPs treatment group ($p < 0.05$). For most organs, ultrasound and microbubbles did not change the biodistribution profile. Only the MI = 0.4 group of the Doxil-like and NonCleavable liposome showed a significant reduction in fluorescence intensity with respect to the Only-LPs treatment group in the liver and kidneys, respectively ($p < 0.05$).

3.5. Microdistribution of liposomes

The microdistribution of liposomes was imaged by CLSM of frozen tumour sections. Representative images from a tumour in the control group and a tumour treated with MI = 0.8 ultrasound and microbubbles are shown in Fig. 5A-B, respectively. An increased prevalence of permeation of the liposomes into the extracellular matrix of the tumour can be observed.

A more quantitative analysis of the CLSM images revealed more details regarding the extravasation and distance travelled by the liposomes into the extracellular matrix of the tumour. From the CLSM images, the number of pixels representing extravasated liposomes was summed per image and plotted per treatment group and liposome as a boxplot (see Fig. 5C). The number of pixels representing extravascular liposomes increased when ultrasound and microbubbles were used. For all liposomes, the increase in number of pixels representing extravasated liposomes was minimal for the MI = 0.4 group but was more profound for the MI = 0.8 group. In case of the Doxil-like liposome, amount of extravasation in both ultrasound treatment groups was statistically significant with respect to the Only-LPs treatment group. This was only the case for the MI = 0.8 group of the NonCleavable and Cleavable liposome.

Comparing the three liposomes, mice treated with the Cleavable liposome showed higher number of pixels representing extravasated liposomes in both the Only-LPs treatment group and both ultrasound treatment groups than mice receiving the Doxil-like or NonCleavable liposome.

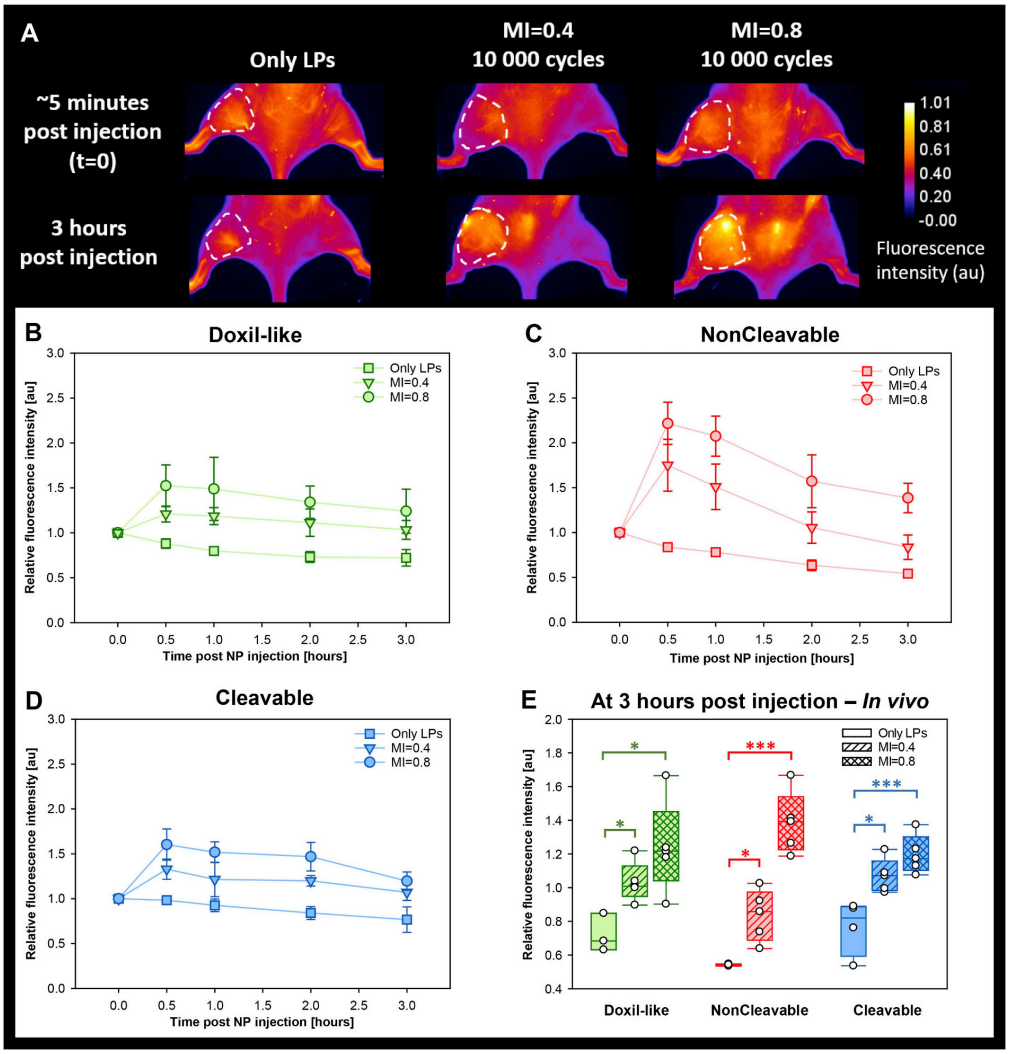

Fig. 3. (A) Representative images taken at t = 0 (~5 minutes) and 3 hours post injection of the liposomes of animals treated with and without ultrasound. White dashed line depicts the tumour ROI. (B-D) The mean relative fluorescence intensity of tumour ROI as function of time for the Doxil-like, NonCleavable and Cleavable liposome, respectively. Normalization was done relative to values at t = 0. Mean and standard deviation are based on 3–5 animals. (E) Boxplot of the *in vivo* mean relative fluorescence intensity in the tumour ROI at 3 hours post liposome injection. The circular symbols depict different animals. Statistically significance is indicated with asterisks (*$p < 0.05$, ***$p < 0.001$).

The effect of ultrasound and microbubbles on the displacement of liposomes from the blood vessels are shown in Fig. 5D–F for the Doxil-like, NonCleavable and Cleavable liposome, respectively. When ultrasound was used, liposomes were observed up to approximately 65 μm away from the blood vessel, independently of which MI and liposome were used. In the case of the Doxil-like and NonCleavable liposome, a doubling of distance travelled could be observed after exposure to ultrasound in the presence of microbubbles. The Cleavable liposomes seemed to extravasate and penetrate well without help of ultrasound and microbubbles compared to the Doxil-like and NonCleavable liposome, since in the Only-LPs treatment group, liposomes were observed up to approximately 60 μm distance from the blood vessel.

3.6. Therapeutic efficacy

A treatment study was performed to assess whether the improved delivery of liposomes by ultrasound could improve the therapeutic response. Tumours were treated with ultrasound of MI = 0.8 in the presence of microbubble as this treatment showed highest tumour uptake of liposomes. The relative tumour growth curves of individual animals treated with the Doxil-like, NonCleavable, Cleavable liposome and free doxorubicin are shown in Supplementary Fig. S8A–D, respectively. Animals that showed a reduced tumour growth with respect to the saline group for at least 7 consecutive days were defined as responders. Mice were euthanized when the tumour length exceeded 15 mm. The tumour growth, number of responders and median survival of the different treatment groups are summarized in Table 5. No significant

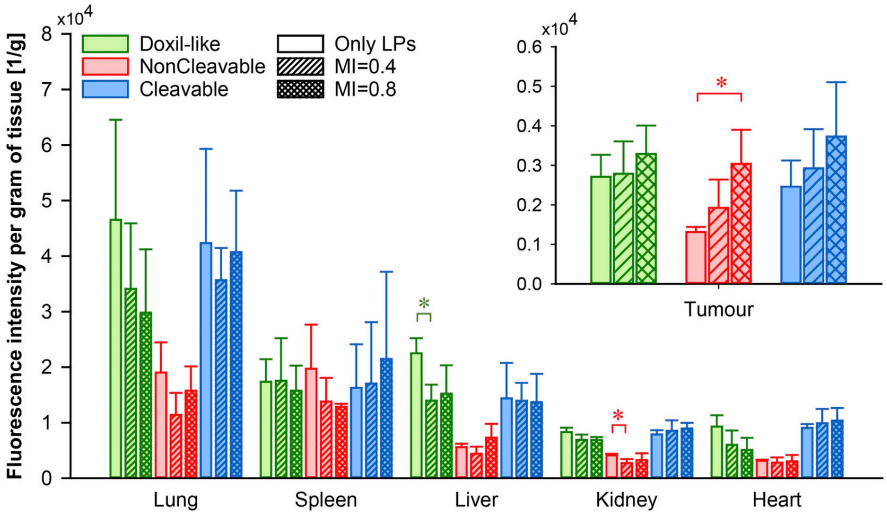

Fig. 4. Biodistribution in organs and tumours visualized as fluorescence intensity per gram of tissue for the three liposomes 3 hours post injection. Group means are shown, and error bars indicate the standard deviation. Statistical significance is shown with an asterisk. (*$p < 0.05$). Mean and standard deviation are based on 3–5 animals.

weight loss, which is a common side effect of cytostatic drugs, was observed for any of the treatments (see Supplementary Fig. S9).

Except for one animal in the control group, most control animals were euthanized between day 28 and 35. Therefore, the mean tumour growth for the first 28 days are shown in Fig. 6A. Solid lines indicate the Only-LPs or free drug treated groups, while the dashed lines indicate ultrasound treated groups. Comparing the control group (saline) with the Doxil-like + FUS, Cleavable + FUS and DOX + FUS treatment groups, a statistically significant reduction in tumour growth was found (58%, 39% and 21%, respectively). Surprisingly, the mice given the free drug had statistically larger tumours with respect to the control animals (+37%) at day 28. When comparing the Only-LPs or free drug treatment with the corresponding ultrasound treatment (-FUS vs +FUS), a statistically significant difference in tumour volume at day 28 was observed for the Doxil-like liposome and free drug treatment.

Of the Only-LPs and only free drug treatment groups, animals treated with the Doxil-like liposome showed the highest number of responders (4/7) followed by the Cleavable (2/5), NonCleavable (2/6) and Free Doxorubicin group (0/6). Using ultrasound and microbubbles in addition resulted in an increased number of responders in all treatment groups with again the highest number of responders for the Doxil-like liposome, i.e. 4 out of 5 of which 2 survived until the end of the study (100 days after first treatment) of which 1 was in full remission. The number of responders for the Cleavable, NonCleavable and Free doxorubicin treatment group increased to 4/6, 4/6 and 3/7, respectively.

The Kaplan-Meier plot in Fig. 6B represents the survival of the animals. Ultrasound and microbubbles combined with injection of the liposomes or free drug, resulted in a prolonged median survival but to different extents. Doxil-like + FUS (51 days, $p = 0.003$), Cleavable + FUS (40.5 days, $p = 0.029$) and DOX + FUS (42 days, $p = 0.037$) resulted in a significantly prolonged survival compared to the control group (32 days, saline). Of the Only-LPs treatment groups, only the Doxil-like liposome resulted in statistically significant increase (39 days, $p = 0.05$) in survival with respect to the control group (32 days, saline). In case of Doxil-like liposomes, there was a borderline significance between the Only-LPs and ultrasound treatment group ($p = 0.055$).

4. Discussion

4.1. Cellular uptake and cytotoxicity

Successful therapeutic response requires efficient cellular uptake and cytotoxicity of the drug-loaded liposomes. The three liposomes were taken up by the cells to various degrees, where NonCleavable performed best, followed by the Cleavable and Doxil-like liposome. The cytotoxicity study showed that both the encapsulated and free drug reduced cell viability, demonstrating the sensitivity of the PC3 cell line to the drug.

Both cellular uptake and cytotoxicity of the liposomes depend on cell-liposome interactions which are based on liposome properties like size and charge [33]. The liposomes used showed only minimal differences in size and charge which therefore cannot fully explain the results obtained. A possible explanation for the obtained differences in cellular uptake and cytotoxicity can be the differences in lipid compositions of the liposomal formulations. Both the Cleavable and NonCleavable liposomes contain unsaturated lipids which have reduced alignment due to the tail being kinked and thereby pack less tightly whilst saturated lipid tails can readily align and pack tightly. The reduced alignment of the unsaturated lipid tails leads to unsaturated bilayers having less rigidity than saturated bilayers (Doxil-like) leading to a faster rate of drug release [34]. This could have caused higher cellular doxorubicin fluorescence compared to the Doxil-like liposome as well as similar cytotoxicity profiles of the NonCleavable and Cleavable liposomes and the free drug.

Enzymatic removal of PEG increased the cellular uptake of the Cleavable liposomes compared to Cleavable liposomes treated with the same activation buffer without thermolysin, demonstrating that the PEG layer can prevent cellular uptake which has also been reported by others [28,29]. Thermolysin had no effect on the cellular uptake of the NonCleavable or Doxil-like liposomes, showing that the thermolysin specifically cleaved the PEGylated cleavable lipopeptide. Incubating PC3 cells with either the NonCleavable or Cleavable liposome in growth medium containing the enzyme activation buffer without thermolysin resulted in a reduced cellular uptake which indicates that adding the enzyme activation buffer to the growth medium potentially changed the metabolic activity and/or cellular uptake mechanisms of the PC3 cells. Most likely due to dilution of the growth medium or the composition of the enzyme activation buffer.

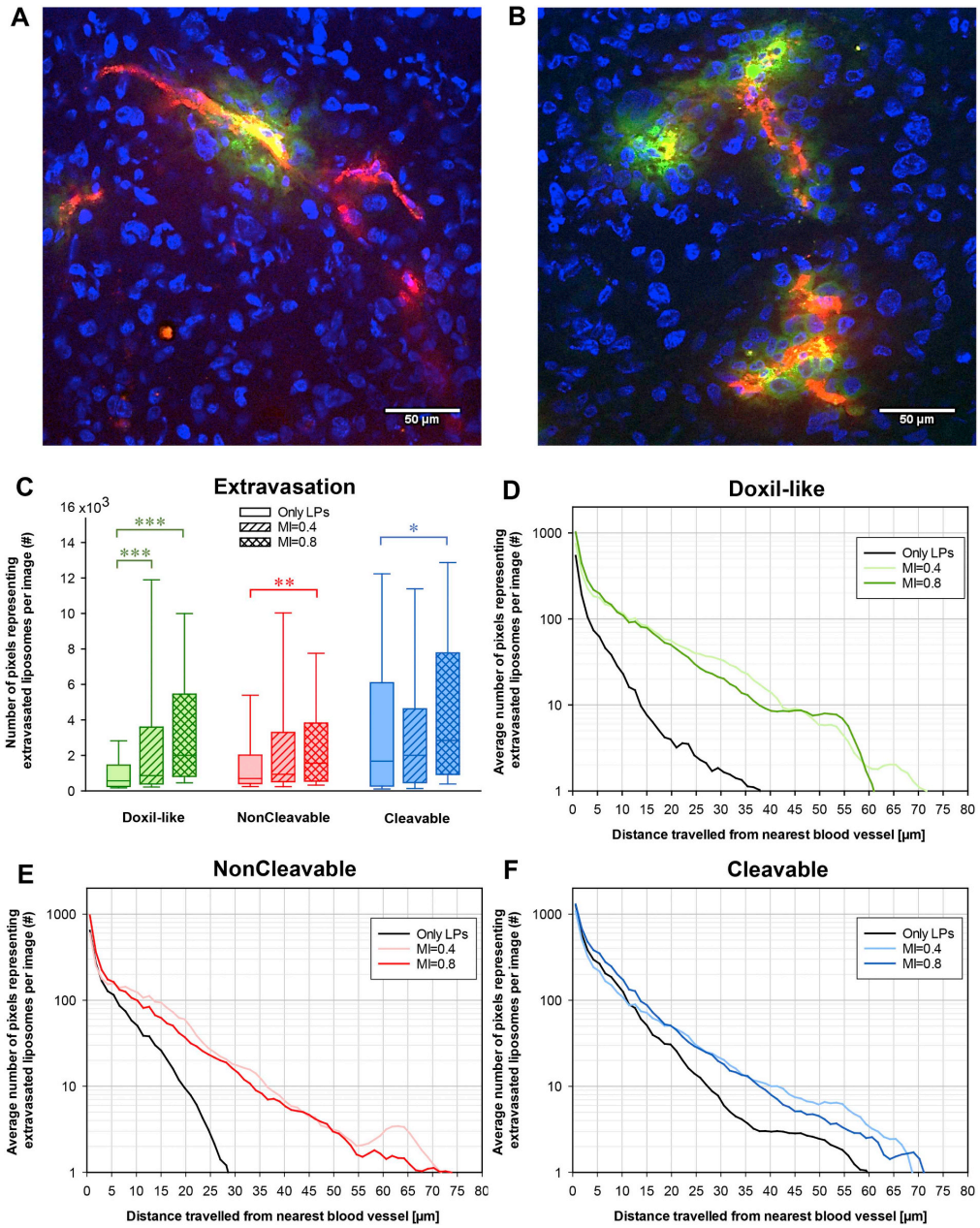

Fig. 5. Representative images of animals treated with (A) only LPs and (B) LPs in combination with MI = 0.8 ultrasound and microbubbles. LPs are shown in green, blood vessels in red and cell nuclei in blue. Scale bar is 50 µm. (C) The average number of pixels representing extravasated liposomes per image per treatment group and liposome. Results are based on 80 to 110 images per treatment group. Solid line in the boxplot and error bars represent the median and standard deviation, respectively. Statistically significance is shown with an asterisk (*$p < 0.05$, **$p < 0.01$, ***$p < 0.001$) (D-F) The average number of liposomes as a function of the distance travelled from the blood vessels, for the Doxil-like, NonCleavable and Cleavable liposomes, respectively.

4.2. Effect of ultrasound and microbubbles on the tumour accumulation of liposomes

Ultrasound in the presence of microbubbles resulted in a significant increase in accumulation of all three liposomes in tumours compared to the Only-LPs treatment groups. The Doxil-like and Cleavable liposome showed similar relative accumulation kinetics, while the NonCleavable liposome showed higher accumulation. 3 hours post treatment the NonCleavable liposome showed similar relative accumulation compared to the other two liposomes.

Table 5
The mean tumour volume at day 28, number of responders and median survival of the different treatment groups. Asterisks indicate statistical significance with respect to the saline group (D = Doxil-like, NC = NonCleavable, C = Cleavable, DOX = Free doxorubicin) (*p < 0.05, **p < 0.01, ***p < 0.001).

Treatment	Mean tumour volume at day 28 [mm^3]		Tumour volume w.r.t. saline at day 28 [%]		Nr. Responders		Median survival [Days]	
	−FUS	+FUS	−FUS	+FUS	−FUS	+FUS	−FUS	+FUS
Saline	888 ± 136	–	–	–	–	–	32	–
D	741 ± 403	372 ± 150 ***	−17%	−58%	4/7	4/5	39 *	51 **
NC	781 ± 98	701 ± 216	−12%	−21%	2/6	4/6	32.5	35
C	832 ± 93	539 ± 225 *	−6%	−39%	2/5	4/6	35	40.5 *
DOX	1236 ± 207 *	698 ± 117 *	+39%	−21%	0/6	3/7	31	42 *

The fluorescence in the tumour ROI will originate from both liposomes still in circulation and liposomes that have extravasated. Assuming that the ultrasound treatment does not change the circulation properties of the liposomes, the increase in relative fluorescence intensity can be attributed to sonopermeation effects.

Microbubbles are constrained to the blood vessels, and their *in* vivo behaviour depends on the ultrasound parameters (frequency, pressure, pulse duration, pulse repetition), microbubble properties (size, shell properties, concentration) and *in vivo* conditions like vessel diameter, vascular structure and viscosity of the blood [21,35–37]. Microbubbles exposed to ultrasound can undergo stable volumetric oscillations, also known as stable cavitation, or more radical oscillations resulting in a violent collapse of the bubble which is known as inertial cavitation. It has been shown that stable cavitation causes microstreaming, improves vascular permeability and stimulates endocytosis, and inertial cavitation might result in shock waves and microjets, which when close to a membrane, can result in transient or permanent pores in the vascular wall or even to more extensive vascular damage [20,23,38,39].

The effect of a wide range of ultrasound parameters on the cavitation behaviour of SonoVue^{TM} microbubbles has been studied mainly in an *in vitro* setting. Based on *in vitro* studies, inertial cavitation was observed above an MI of 0.5 [40,41], while *in vivo* inertial cavitation became observable at MI > 0.62 [41]. Thus, it is expected that in the case of the MI = 0.4 treatment groups mainly stable cavitation occurs and when using an MI of 0.8, more inertial cavitation is expected. This was confirmed when detecting the cavitation behaviour of SonoVue^{TM} (see Supplementary Fig. S10), both more stable and inertial cavitation was observed in the MI = 0.8 group compared to the MI = 0.4 group. The difference in microbubble behaviour and the corresponding biomechanical effects are likely to be the reason for the higher uptake of liposomes and improved extravasation in the MI = 0.8 groups.

Ultrasound in the presence of microbubbles can change the perfusion. Both vascular shutdown and increased perfusion by opening of non-perfused microvessels, have been reported [42,43]. An increased perfusion of the tumour could partly explain the observed increase in tumour fluorescence intensity in the ultrasound treatment groups.

If cavitation and perfusion do not differ between the three liposomes, the observed increased tumour uptake of the NonCleavable liposome with respect to the other two liposomes, should be due to an interplay of liposome properties (formulation, size, charge, PEGylation, etc.), tumour characteristics (vascularization, EPR-effect, etc.) and interaction with blood components. In both the NonCleavable and Cleavable liposome, cholesterol is used as the lipid anchor of the PEG. Cholesterol is known to partition out which could result in the liposomes losing their PEG-layer over time thereby altering their *in vivo* behaviour. That this happens cannot be completely ruled out, but it is expected that the effect will be minimal and similar across the NonCleavable and Cleavable liposome because of the similar amount of Chol-PEG used in both formulations. The size of the Cleavable and NonCleavable liposome did not differ while the Doxil-like liposome exhibited a slightly smaller size which can be beneficial with respect to extravasation. The NonCleavable liposome had a higher zeta potential (-3.8 mV) compared to the Doxil-like and Cleavable liposome (-13.4 mV and -13.7 mV, respectively) and it has been shown that a more neutral charge of the particles could result in less interactions with the negatively charged endothelial cell membrane and extracellular matrix components and thereby increase the extravasation and diffusion rate [26,44,45]. In addition, neutral liposomes show less interaction with charged blood components whereas more negatively or positively charged liposomes will undergo more and different protein adsorption

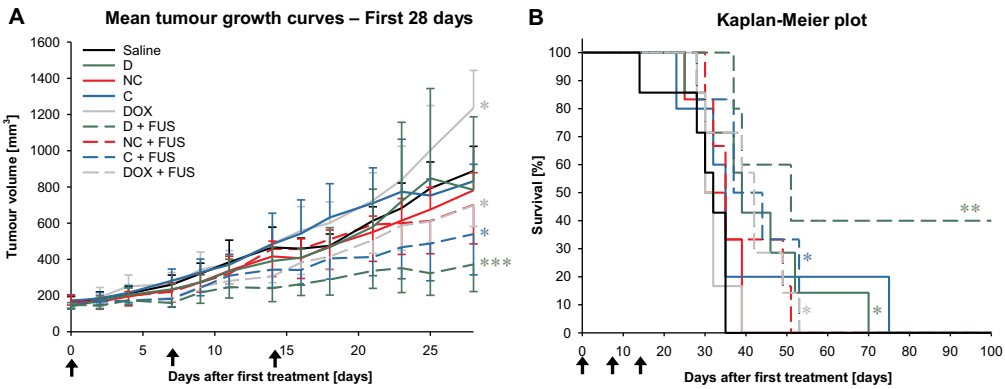

Fig. 6. (A) Tumour growth curves of the first 28 days after the first treatment. Line plot and error bars represent the mean of 5–7 mice and standard deviation, respectively. Asterisks show significant tumour reductions with respect to the saline treatment group (*p < 0.05, ***p < 0.001) (B) Kaplan-Meier plot. Different colours indicate the different LPs or drug used. Solid lines indicate only LPs or drug treatment groups. Dashed lines indicate the ultrasound treatment groups (+FUS). Treatments took place on day 0, 7 and 14 and are indicated with a black arrow. (*p < 0.05, **p < 0.01) (D = Doxil-like, NC = NonCleavable, C = Cleavable, DOX = Free doxorubicin, FUS = Focused ultrasound and microbubbles).

hence altering their properties, i.e. size, shape, charge, etc., which will affect their extravasation and tumour accumulation [46,47]. The more neutral charge of the NonCleavable liposome could therefore potentially have been beneficially for tumour accumulation rate.

4.3. Biodistribution of liposomes in tumour and normal organs

Imaging of the excised tumour showed increased tumour accumulation of the liposomes after ultrasound which is consistent with the *in vivo* measurements done 3 hours post treatment. However, most of the statistical significance between the Only-LPs and ultrasound treatment groups found in the *in vivo* dataset was lost after excising the tumour. This is most likely due to the correction for the weight of the tumour in the *ex vivo* biodistribution dataset.

The biodistribution of normal organs showed that ultrasound and microbubbles did not alter the biodistribution profiles of the organs. Organs were excised three hours after ultrasound treatment and based on the circulation half-life time of 3 to 4 hours (see Table S1 and Fig. S2), the measured fluorescence intensity will originate both from liposomes still in circulation and liposomal uptake by the organs. The relative high uptake by the lungs, especially for the Cleavable and Doxil-like liposome, is interesting. A possible explanation could be that the lung capillaries are the first capillaries the liposomes encounter after injection in the lateral tail vein such that aggregates get stuck in the microvasculature of the lungs. In addition, the lungs of mice have the largest mean blood volume per gram of wet tissue (0.49 ml) followed by liver (0.36 ml), kidneys (0.34 ml) and spleen (0.17 ml) which could be one of the reasons of the relatively high fluorescence intensity originating from the lungs for all three liposomes [48]. High fluorescence intensities of the spleen and liver are expected since macrophages, which are responsible for clearing liposomes and other substances from the blood, are residing in those organs [49].

4.4. Microdistribution – Extravasation and penetration depth of liposomes

After recording tumour accumulation of the liposomes, the intra tumoural microdistribution of the liposomes in frozen tumour tissues was imaged by CLSM. The Cleavable liposome was found to extravasate to a larger extent than the other two liposomes. For all liposomes, the exposure to ultrasound and microbubbles increased the extravasation significantly and most profoundly after MI = 0.8. Many have reported on enhanced extravasation of liposomes in tumours after exposure to ultrasound and microbubbles, which is most likely caused by cavitating microbubbles increasing the vascular permeability in the tumour [11–15]. Here an MI of 0.4 and 0.8 were used, and improved extravasation was observed for increasing MI and for both ultrasound treatment groups with respect to the Only-LPs group, which agrees well with what have been reported [13,37].

Physiochemical properties and tumour characteristics will determine the *in vivo* fate of the liposomes including their extravasation and tumour penetration [9,50,51]. When no ultrasound is used, penetration of liposomes through the extracellular matrix will be mainly diffusion driven due to the high interstitial fluid pressure, which favours the use of liposomes with a smaller hydrodynamic diameter [52,53]. Interestingly, the Cleavable liposome showed almost a doubled penetration depth with respect to the other two liposomes when no ultrasound was used. A potential reason could be the enzyme sensitive properties of the liposome. The animals were euthanized 3 hours post treatment and within those 3 hours, the extravasated liposomes will come in contact with MMPs causing cleavage of the PEG layer. The presence and activity of the MMPs in the used tumour model has been shown by *in situ* zymography (see Supplementary Fig. S11). MMPs of interest are located at the basement membranes along collagen type IV fibres, thus PEG cleavage can take place immediately after extravasation [54]. How fast and to what extent the PEG layer will be cleaved will depend on several factors including liposome concentration, enzyme concentrations and accessibility of the peptide for the enzymes. PEG cleavage by MMPs reveals a negatively charged residue which could facilitate electrostatic interactions with the ECM, enhancing liposome retention.

Ultrasound increased the penetration of all liposomes into the ECM, and the effect was the smallest for the Cleavable liposome. Interestingly, even though the amount of extravasation was different for the three liposomes, the distance travelled from the nearest blood vessel was rather similar between the liposomes in the two ultrasound groups, and in accordance with penetration depths reported by others [55]. The observed improved penetration depth could indicate that sonopermeation also causes extravascular effects such as acoustic streaming, shockwave generation, jet formation and possible structural changes in the extracellular matrix and creation of pores [23,56]. Even though the microbubbles showed a clear increase in cavitation behaviour at the higher MI (Supplementary Fig. S10), surprisingly, a similar penetration depth was observed in the studied time window. Both our observations and reports from others might indicate that there is a maximum penetration depth of liposomes from the blood vessels [55].

4.5. Therapeutic efficacy study

The tumours exposed to the Doxil-like liposome combined with ultrasound and microbubbles showed the best therapeutic response. A tumour volume reduction up to ~60% with respect to the control group (saline) was obtained, the number of responders increased, and median survival was prolonged. Also for the Cleavable liposome and the free drug doxorubicin, an improved therapeutic response was observed after ultrasound-mediated delivery, but to a lower extent. The ultrasound treatments used are not expected to have any therapeutic effect on their own. This assumption is supported by studies in [57,58].

When comparing the observed microdistribution of the liposomes with the obtained therapeutic efficacy of the liposomes, it should be kept in mind that both experiments have been performed with different batches of liposomes. For each of the liposomes, the variability in size and zeta potential between the different batches used for both the *in vitro* and *in vivo* experiments are small and within acceptable values, but could indicate for example differences in PEG coverages. This could have affected the *in vivo* behaviour of the liposomes, also with respect to the observed *in vitro* behaviour. Due to the relatively small differences in zeta potential and size between the different batches used, a large impact on the *in vivo* behaviour of the liposomes is not expected, but small alterations in *in vivo* behaviour cannot be ruled out. Due to the expected minor effect, it is assumed that the obtained microdistribution data is representative for the *in vivo* behaviour of the liposomes when discussing the therapeutic efficacy.

Even though the Cleavable liposome already extravasated and penetrated the extracellular matrix well by itself compared to the other two liposomes, no effect on the therapeutic efficacy of the Only-LPs treatment was observed. One possible explanation could be that although many liposomes penetrated far into the extracellular matrix, the number was not sufficient for any therapeutic effect. It is possible that cleaving of the PEG increased the uptake of the liposomes by macrophages and other non-tumour cells. The majority of nanoparticles is reported to either being trapped in the extracellular matrix or taken up by perivascular cells and other macrophages resulting in 0.0014% of administered nanoparticles being internalized by the tumour cells [59]. So even though the Cleavable liposome seemed to extravasate the best of the three liposomes, the final number reaching the tumour cells was not sufficient for any therapeutic effect. Adding ultrasound and microbubbles to the treatment resulted in an improved extravasation of the Cleavable liposome, but the penetration depth was only minimally affected. This reduced the tumour growth with almost a factor 6.5 (39%/6%) 28 days after the first treatment.

The difference in therapeutic efficacy between the NonCleavable and Cleavable liposome is interesting since the differences in liposome

properties (lipid formulation, size, charge) were minimal. Nevertheless, the Cleavable liposome extravasated and penetrated the extracellular matrix better than the NonCleavable liposome. Even though the extravasation and penetration of the NonCleavable liposome was similar to the successful Doxil-like liposome and the number of responders was similar to the Cleavable liposome, no effect on therapeutic efficacy was observed. This could indicate that the MMP sensitive property of the Cleavable liposome has positively affected the therapeutic efficacy as well.

Interestingly, the group of animals receiving only free doxorubicin showed increased tumour growth with respect to the control group. It has been reported that low doses of doxorubicin can induce drug resistance which could explain the observed induced tumour growth [60]. In case of the ultrasound treatment group, the animals showed a significant reduced tumour growth, which is interesting since the drug molecule should be able to diffuse easily by itself into the tumour tissue. Nevertheless, sonopermeation potentially resulted in an increased local delivery to tumour tissue such that free doxorubicin became more efficient. Improved ultrasound-mediated therapeutic response of small drugs has also been observed in a clinical trial on inoperable pancreatic cancer [17].

The promising preclinical studies demonstrating that ultrasound and microbubbles improve delivery of nanomedicine and enhance the therapeutic response, have led to several clinical studies ([17], NCT03477019, NCT00245869 and more). When using ultrasound-mediated delivery of drugs and liposomes in the clinic, stratification of patients to determine which patients will benefit from the treatment is important. It has been shown preclinically that tumours with low EPR effect, such as the PC3 tumour model used in the present study, benefits more from the use of ultrasound-mediated delivery of liposomes compared to tumours that are well vascularized and have a high EPR effect [55].

The current study showed that combined with ultrasound and microbubbles, the Cleavable liposome had a better therapeutic efficacy compared to the NonCleavable liposome indicating that cleaving of the PEG-layer can be important. However, the Doxil-like liposome outcompeted the NonCleavable and Cleavable liposomes and free drug doxorubicin treatment groups both with and without the use of ultrasound and microbubbles.

5. Conclusion

Focused ultrasound in the presence of microbubbles resulted in an improved tumour accumulation, increased extravasation and increased penetration depth of liposomes into the extracellular matrix compared to mice receiving just an injection of liposomes. The Cleavable liposome performed better than the NonCleavable both in terms of extravasation, microdistribution and therapeutic efficacy. Both for Doxil-like and Cleavable liposomes, the ultrasound-mediated delivery resulted in an improved therapeutic efficacy.

Declaration of Competing Interest

The authors declare that they have no known competing financial interests or personal relationships that could have appeared to influence the work reported in this paper.

Acknowledgements

Kristin Grendstad from NTNU is thanked for technical assistance with cell culturing and flow cytometry. Lars Ringgaard Petersen and Gael Clergeaud Veiga from DTU are acknowledged for their technical support. Housing of the animals was provided by the Comparative Medicine Core Facility (CoMed, NTNU). Tissue sections were prepared by the Cellular and Molecular Imaging Core Facility (CMIC, NTNU). Astrid Bjørkøy and the Centre for Molecular Imaging at the Faculty of Natural Sciences (MINT, NTNU) are thanked for technical assistance with CLSM. The project was internally funded by the Norwegian University of Science and Technology (NTNU, Trondheim, Norway). Additional funding from the Central Norway Regional Health Authorities and the Norwegian Research Council (project 262228) is acknowledged.

Appendix A. Supplementary data

Supplementary data to this article can be found online at https://doi.org/10.1016/j.jconrel.2020.06.024.

References

[1] A.A. Epenetos, D. Snook, H. Durbin, P.M. Johnson, J. Taylor-Papadimitriou, Limitations of radiolabeled monoclonal antibodies for localization of human neoplasms, Cancer Res. 46 (1986) 3183–3191.
[2] H.-P. Gerber, P.D. Senter, I.S. Grewal, Antibody drug-conjugates targeting the tumor vasculature: current and future developments, MAbs, Taylor & Francis, 2009, pp. 247–253.
[3] A.K. Iyer, G. Khaled, J. Fang, H. Maeda, Exploiting the enhanced permeability and retention effect for tumor targeting, Drug Discov. Today 11 (2006) 812–818.
[4] H. Maeda, J. Wu, T. Sawa, Y. Matsumura, K. Hori, Tumor vascular permeability and the EPR effect in macromolecular therapeutics: a review, J. Control. Release 65 (2000) 271–284.
[5] J. Fang, H. Nakamura, H. Maeda, The EPR effect: unique features of tumor blood vessels for drug delivery, factors involved, and limitations and augmentation of the effect, Adv. Drug Deliv. Rev. 63 (2011) 136–151.
[6] D. Peer, J.M. Karp, S. Hong, O.C. Farokhzad, R. Margalit, R. Langer, Nanocarriers as an emerging platform for cancer therapy, Nat Nano 2 (2007) 751–760.
[7] S. Torosean, B. Flynn, J. Axelsson, J. Gunn, K.S. Samkoe, T. Hasan, M.M. Doyley, B.W. Pogue, Nanoparticle uptake in tumors is mediated by the interplay of vascular and collagen density with interstitial pressure, Nanomedicine: Nanotechnology, Biol. Med. 9 (2013) 151–158.
[8] A.A. Manzoor, L.H. Lindner, C.D. Landon, J.-Y. Park, A.J. Simnick, M.R. Dreher, S. Das, G. Hanna, W. Park, A. Chilkoti, Overcoming limitations in nanoparticle drug delivery: triggered, intravascular release to improve drug penetration into tumors, Cancer Res. 72 (2012) 5566–5575.
[9] R.K. Jain, T. Stylianopoulos, Delivering nanomedicine to solid tumors, Nat. Rev. Clin. Oncol. 7 (2010) 653–664.
[10] L. Eikenes, I. Tufto, E.A. Schnell, A. Bjørkøy, C.D.L. Davies, Effect of collagenase and hyaluronidase on free and anomalous diffusion in multicellular spheroids and xenografts, Anticancer Res. 30 (2010) 359–368.
[11] S. Eggen, M. Afadzi, E.A. Nilssen, S.B. Haugstad, B. Angelsen, C.D.L. Davies, Ultrasound improves the uptake and distribution of liposomal Doxorubicin in prostate cancer xenografts, Ultrasound Med. Biol. 39 (2013) 1255–1266.
[12] S. Eggen, S.-M. Fagerland, Ý. Mørch, R. Hansen, K. Søvik, S. Berg, H. Furu, A.D. Bøhn, M.B. Lilledahl, A. Angelsen, Ultrasound-enhanced drug delivery in prostate cancer xenografts by nanoparticles stabilizing microbubbles, J. Control. Release 187 (2014) 39–49.
[13] S. Snipstad, S. Berg, Ý. Mørch, A. Bjørkøy, E. Sulheim, R. Hansen, I. Grimstad, A. van Wamel, A.F. Maaland, S.H. Torp, Ultrasound improves the delivery and therapeutic effect of nanoparticle-stabilized microbubbles in breast cancer xenografts, Ultrasound Med. Biol. 43 (2017) 2651–2669.
[14] S. Kotopoulis, A. Delalande, M. Popa, V. Mamaeva, G. Dimcevski, O.H. Gilja, M. Postema, B.T. Gjertsen, E. McCormack, Sonoporation-enhanced chemotherapy significantly reduces primary tumour burden in an orthotopic pancreatic cancer xenograft, Mol. Imag. Biol. 16 (2014) 53–62.
[15] C.-Y. Lin, J.-R. Li, H.-C. Tseng, M.-F. Wu, W.-L. Lin, Enhancement of focused ultrasound with microbubbles on the treatments of anticancer nanodrug in mouse tumors, Nanomedicine: Nanotechnology, Biol. Med. 8 (2012) 900–907.
[16] M. Aryal, N. Vykhodtseva, Y.-Z. Zhang, J. Park, N. McDannold, Multiple treatments with liposomal doxorubicin and ultrasound-induced disruption of blood–tumor and blood–brain barriers improve outcomes in a rat glioma model, J. Control. Release 169 (2013) 103–111.
[17] G. Dimcevski, S. Kotopoulis, T. Bjånes, D. Hoem, J. Schjøtt, B.T. Gjertsen, M. Biermann, A. Molven, H. Sorbye, E. McCormack, A human clinical trial using ultrasound and microbubbles to enhance gemcitabine treatment of inoperable pancreatic cancer, J. Control. Release 243 (2016) 172–181.
[18] A. Carpentier, M. Canney, A. Vignot, V. Reina, K. Beccaria, C. Horodyckid, C. Karachi, D. Leclercq, C. Lafon, J.Y. Chapelon, Clinical trial of blood-brain barrier disruption by pulsed ultrasound, Sci. Transl. Med. 8 (2016) 343re342-343re342.
[19] I. De Cock, E. Zagato, K. Braeckmans, Y. Luan, N. de Jong, S.C. De Smedt, I. Lentacker, Ultrasound and microbubble mediated drug delivery: acoustic pressure as determinant for uptake via membrane pores or endocytosis, J. Control. Release 197 (2015) 20–28.
[20] I. Lentacker, I. De Cock, R. Deckers, S. De Smedt, C. Moonen, Understanding ultrasound induced sonoporation: definitions and underlying mechanisms, Adv. Drug Deliv. Rev. 72 (2014) 49–64.
[21] K. Kooiman, H.J. Vos, M. Versluis, N. de Jong, Acoustic behavior of microbubbles

and implications for drug delivery, Adv. Drug Deliv. Rev. 72 (2014) 28–48.
[22] M. Afadzi, S.P. Strand, E.A. Nilssen, S.-E. Masøy, T.F. Johansen, R. Hansen, B.A. Angelsen, C.D.L. Davies, Mechanisms of the ultrasound-mediated intracellular delivery of liposomes and dextrans, IEEE Trans. Ultrason. Ferroelectr. Frequency Control 60 (2012) 21–33.
[23] S. Snipstad, E. Sulheim, C. de Lange Davies, C. Moonen, G. Storm, F. Kiessling, R. Schmid, T. Lammers, Sonopermeation to improve drug delivery to tumors: from fundamental understanding to clinical translation, Exp. Opin. Drug Deliv. 15 (2018) 1249–1261.
[24] A. Gabizon, F. Martin, Polyethylene glycol-coated (pegylated) liposomal doxorubicin, Drugs 54 (1997) 15–21.
[25] M.J. Ernsting, M. Murakami, A. Roy, S.-D. Li, Factors controlling the pharmacokinetics, biodistribution and intratumoral penetration of nanoparticles, J. Control. Release 172 (2013) 782–794.
[26] T. Stylianopoulos, M.-Z. Poh, N. Insin, M.G. Bawendi, D. Fukumura, L.L. Munn, R.K. Jain, Diffusion of particles in the extracellular matrix: the effect of repulsive electrostatic interactions, Biophys. J. 99 (2010) 1342–1349.
[27] S. Lélu, S.P. Strand, J. Steine, C.D.L. Davies, Effect of PEGylation on the diffusion and stability of chitosan–DNA polyplexes in collagen gels, Biomacromolecules 12 (2011) 3656–3665.
[28] S. Mishra, P. Webster, M.E. Davis, PEGylation significantly affects cellular uptake and intracellular trafficking of non-viral gene delivery particles, Eur. J. Cell Biol. 83 (2004) 97–111.
[29] B. Romberg, W.E. Hennink, G. Storm, Sheddable coatings for long-circulating nanoparticles, Pharm. Res. 25 (2008) 55–71.
[30] M. Roomi, J. Monterrey, T. Kalinovsky, M. Rath, A. Niedzwiecki, Patterns of MMP-2 and MMP-9 expression in human cancer cell lines, Oncol. Rep. 21 (2009) 1323–1333.
[31] J. Bruun, T.B. Larsen, R.I. Jølck, R. Eliasen, R. Holm, T. Gjetting, T.L. Andresen, Investigation of enzyme-sensitive lipid nanoparticles for delivery of siRNA to blood-brain barrier and glioma cells, Int. J. Nanomed. 10 (2015) 5995–6008.
[32] S. Snipstad, S. Hak, H. Baghirov, E. Sulheim, Ý. Mørch, S. Lélu, E. von Haartman, M. Bäck, K.P.R. Nilsson, A.S. Klymchenko, Labeling nanoparticles: Dye leakage and altered cellular uptake, Cytometry Part A 91 (2017) 760–766.
[33] A. Verma, F. Stellacci, Effect of surface properties on nanoparticle–cell interactions, Small 6 (2010) 12–21.
[34] T. Lian, R.J. Ho, Trends and developments in liposome drug delivery systems, J. Pharm. Sci. 90 (2001) 667–680.
[35] N. Hosseinkhah, K. Hynynen, A three-dimensional model of an ultrasound contrast agent gas bubble and its mechanical effects on microvessels, Phys. Med. Biol. 57 (2012) 785–808.
[36] X. Guo, Q. Li, Z. Zhang, D. Zhang, J. Tu, Investigation on the inertial cavitation threshold and shell properties of commercialized ultrasound contrast agent microbubbles, J. Acoust. Soc. Am. 134 (2013) 1622–1631.
[37] P.T. Yemane, A.K. Åslund, S. Snipstad, A. Bjørkøy, K. Grendstad, S. Berg, Y. Mørch, S.H. Torp, R. Hansen, C. de Lange Davies, Effect of Ultrasound on the Vasculature and Extravasation of Nanoscale Particles Imaged in Real Time, Ultrasound Med. Biol. 45 (2019) 3028–3041.
[38] V. Frenkel, Ultrasound-mediated delivery of drugs and genes to solid tumors, Adv. Drug Deliv. Rev. 60 (2008) 1193–1208.
[39] Y. Hu, J.M. Wan, C. Alfred, Membrane perforation and recovery dynamics in microbubble-mediated sonoporation, Ultrasound Med. Biol. 39 (2013) 2393–2405.
[40] Y. Lin, L. Lin, M. Cheng, L. Jin, L. Du, T. Han, L. Xu, C. Alfred, P. Qin, Effect of acoustic parameters on the cavitation behavior of SonoVue microbubbles induced by pulsed ultrasound, Ultrason. Sonochem. 35 (2017) 176–184.
[41] S.-K. Wu, P.-C. Chu, W.-Y. Chai, S.-T. Kang, C.-H. Tsai, C.-H. Fan, C.-K. Yeh, H.-L. Liu, Characterization of different microbubbles in assisting focused ultrasound-induced blood-brain barrier opening, Sci. Rep. 7 (2017) 46689.
[42] C.P. Keravnou, I. De Cock, I. Lentacker, M.-L. Izamis, M.A. Averkiou, Microvascular injury and perfusion changes induced by ultrasound and microbubbles in a machine-perfused pig liver, Ultrasound Med. Biol. 42 (2016) 2676–2686.
[43] X. Hu, A. Kheirolomoom, L.M. Mahakian, J.R. Beegle, D.E. Kruse, K.S. Lam, K.W. Ferrara, Insonation of targeted microbubbles produces regions of reduced blood flow within tumor vasculature, Invest. Radiol. 47 (2012) 398.
[44] S. Krasnici, A. Werner, M.E. Eichhorn, M. Schmitt-Sody, S.A. Pahernik, B. Sauer, B. Schulze, M. Teifel, U. Michaelis, K. Naujoks, Effect of the surface charge of liposomes on their uptake by angiogenic tumor vessels, Int. J. Cancer 105 (2003) 561–567.
[45] O. Lieleg, R.M. Baumgärtel, A.R. Bausch, Selective filtering of particles by the extracellular matrix: an electrostatic bandpass, Biophys. J. 97 (2009) 1569–1577.
[46] J. Lazarovits, Y.Y. Chen, E.A. Sykes, W.C. Chan, Nanoparticle–blood interactions: the implications on solid tumour targeting, Chem. Commun. 51 (2015) 2756–2767.
[47] S.M. Ahsan, C.M. Rao, M.F. Ahmad, Nanoparticle-protein interaction: the significance and role of protein corona, Cellular and Molecular Toxicology of Nanoparticles, Springer, 2018, pp. 175–198.
[48] N. Kaliss, D. Pressman, Plasma and blood volumes of mouse organs, as determined with radioactive iodoproteins, Proc. Soc. Exp. Biol. Med. 75 (1950) 16–20.
[49] S.-D. Li, L. Huang, Pharmacokinetics and biodistribution of nanoparticles, Mol. Pharm. 5 (2008) 496–504.
[50] Q. Sun, T. Ojha, F. Kiessling, T. Lammers, Y. Shi, Enhancing tumor penetration of nanomedicines, Biomacromolecules 18 (2017) 1449–1459.
[51] Y.R. Zhang, R. Lin, H.J. Li, W.L. He, J.Z. Du, J. Wang, Strategies to improve tumor penetration of nanomedicines through nanoparticle design, Wiley Interdiscip. Rev. Nanomed. Nanobiotechnol. 11 (2019) 1519.
[52] R.K. Jain, L.T. Baxter, Mechanisms of heterogeneous distribution of monoclonal antibodies and other macromolecules in tumors: significance of elevated interstitial pressure, Cancer Res. 48 (1988) 7022–7032.
[53] H. Cabral, Y. Matsumoto, K. Mizuno, Q. Chen, M. Murakami, M. Kimura, Y. Terada, M. Kano, K. Miyazono, M. Uesaka, Accumulation of sub-100 nm polymeric micelles in poorly permeable tumours depends on size, Nat. Nanotechnol. 6 (2011) 815.
[54] O.R. Mook, C.V. Overbeek, E.G. Ackema, F.V. Maldegem, W.M. Frederiks, In situ localization of gelatinolytic activity in the extracellular matrix of metastases of colon cancer in rat liver using quenched fluorogenic DQ-gelatin, J. Histochem. Cytochem. 51 (2003) 821–829.
[55] B. Theek, M. Baues, T. Ojha, D. Möckel, S.K. Veettil, J. Steitz, L. van Bloois, G. Storm, F. Kiessling, T. Lammers, Sonoporation enhances liposome accumulation and penetration in tumors with low EPR, J. Control. Release 231 (2016) 77–85.
[56] S. Lee, H. Han, H. Koo, J.H. Na, H.Y. Yoon, K.E. Lee, H. Lee, H. Kim, I.C. Kwon, K. Kim, Extracellular matrix remodeling in vivo for enhancing tumor-targeting efficiency of nanoparticle drug carriers using the pulsed high intensity focused ultrasound, J. Control. Release 263 (2017) 68–78.
[57] R. Carlisle, J. Choi, M. Bazan-Peregrino, R. Laga, V. Subr, L. Kostka, K. Ulbrich, C.-C. Coussios, L.W. Seymour, Enhanced Tumor Uptake and Penetration of Virotherapy Using Polymer Stealthing and Focused Ultrasound, JNCI: J. Nat. Cancer Inst. 105 (2013) 1701–1710.
[58] A. van Wamel, P.C. Sontum, A. Healey, S. Kvåle, N. Bush, J. Bamber, C. de Lange Davies, Acoustic Cluster Therapy (ACT) enhances the therapeutic efficacy of paclitaxel and Abraxane® for treatment of human prostate adenocarcinoma in mice, J. Control. Release 236 (2016) 15–21.
[59] Q. Dai, S. Wilhelm, D. Ding, A.M. Syed, S. Sindhwani, Y. Zhang, Y.Y. Chen, P. MacMillan, W.C. Chan, Quantifying the ligand-coated nanoparticle delivery to cancer cells in solid tumors, ACS Nano 12 (2018) 8423–8435.
[60] C. Christowitz, T. Davis, A. Isaacs, G. Van Niekerk, S. Hattingh, A.-M. Engelbrecht, Mechanisms of doxorubicin-induced drug resistance and drug resistant tumour growth in a murine breast tumour model, BMC cancer 19 (2019) 757.

Supplementary Information for

ULTRASOUND-MEDIATED DELIVERY ENHANCES THERAPEUTIC EFFICACY OF MMP SENSITIVE LIPOSOMES

Marieke Olsman[1], Viktoria Sereti[2], Kristine Andreassen[1], Sofie Snipstad[1,3,6], Annemieke van Wamel[1], Rasmus Eliasen[2], Sigrid Berg[4,5,6], Andrew J. Urquhart[2], Thomas L. Andresen[2], Catharina de Lange Davies[1]

[1] Department of Physics, Norwegian University of Science and Technology, Trondheim, Norway
[2] Department of Health Technology, Center for Nanomedicine and Theranostics, Technical University Denmark, DTU Healthtech, Lyngby, Denmark
[3] Department of Biotechnology and Nanomedicine, SINTEF Industry, Trondheim, Norway
[4] Department of Circulation and Medical Imaging, Norwegian University of Science and Technology, Trondheim, Norway
[5] Department of Health Research, SINTEF Digital, Trondheim, Norway
[6] Cancer Clinic, St. Olavs Hospital, Trondheim, Norway

Corresponding author
Marieke Olsman, marieke.olsman@ntnu.no

Confocal laser scanning microscopy image post processing

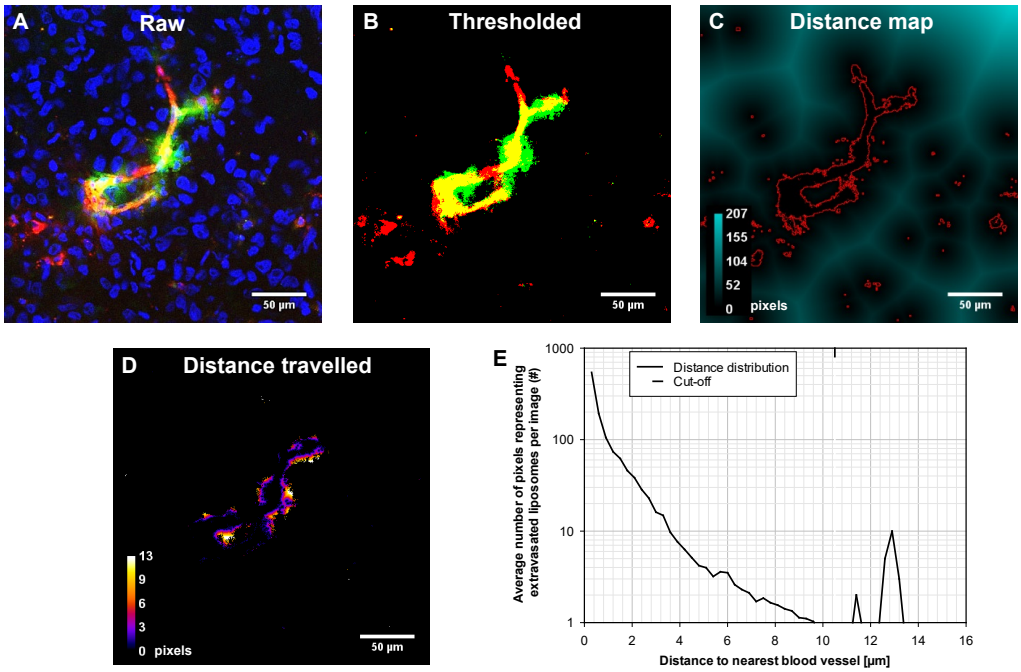

Figure S1: CLSM image post processing. (A) Raw CLSM image showing blood vessel (red), liposomes (green) and cell nuclei (blue). (B) Overlay of the thresholded image from the blood vessel (red) and nanoparticle (green) channel. Yellow represents intravascular liposomes while green represents extravascular liposomes. (C) Distance map created based on the thresholded blood vessel image. Red represents the outline of the blood vessel. Brightness of the cyan coloured pixels indicate the distance in number of pixels towards the nearest blood vessel pixel. (D) Thresholded nanoparticle channel multiplied pixel by pixel with the distance map. Colour of the pixel in the resulting image indicates the distance to the nearest blood vessel pixel in number of pixels for only the pixels representing extravascular liposomes. (E) Illustrative example of a histogram representing the distribution of the distance travelled by liposomes. On the y-axis the number of pixels representing extravascular liposomes at a certain distance to the nearest blood vessel pixel in µm (1 pixel = 0.6 µm) (x-axis). Peaks of fluorescent pixels after the curve had decayed were excluded from the analysis.

In vivo circulation half-life time liposomes

For each liposome, 5 mice were injected with 100µl of 6.0 mM liposome solution of which the characteristics are shown in Table S1. Blood samples (10-20µl) were drawn from the saphenous vein pre injection and at 5 minutes, 1, 2, 4, 8, 24 and 48 hours post injection. Blood samples were diluted in vials holding 40 µl of 10 IU/ml heparin and vortexed. Samples were protected from light during the entire procedure. Before centrifuging at 3000 rpm for 7 minutes, the samples were vortexed again. 20ul of the supernatant was pipetted into wells of a black 384 well plate (Corning Inc., Sigma-Aldrich, USA) and the fluorescence was measured with a spectrofluorometer (SpectraMax i3x, Molecular Devices, Sunnyvale, CA, USA) by exciting at 500nm and detecting emission at 525nm. Fluorescence intensity per volume of blood diluted in heparin, was plotted against the corresponding timepoint. SigmaPlot (v14.0, Systat Software Inc., USA) was used to fit a bi-exponential decay curve to the datapoints from which a circulation half-life time was calculated.

A bi-exponential decay curve was fitted to the datapoints (see Figure S2). For the Doxil-like, NonCleavable and Cleavable liposome a circulation half-life time $T_{1/2}$ of 2.9, 4.0 and 3.2 hours was obtained, respectively. The R^2 values of the fit were 0.69, 0.70 and 0.94, respectively.

Table S1: The average diameter, Ç-potential, PDI, circulation half-life time $T_{1/2}$ and R^2 squared values of the bi-exponential fit for the fluorophore labelled liposomes used for the blood circulation study.

LIPOSOME	Diameter [nm]	Ç-potential [mV]	PDI	$T_{1/2}$	R^2
Doxil-like	108	-10.9±0.7	0.028±0.011	2.9	0.69
NonCleavable	116	-3.2±0.5	0.083±0	4.0	0.70
Cleavable	155	-15.7±0.2	0.065±0.015	3.2	0.94

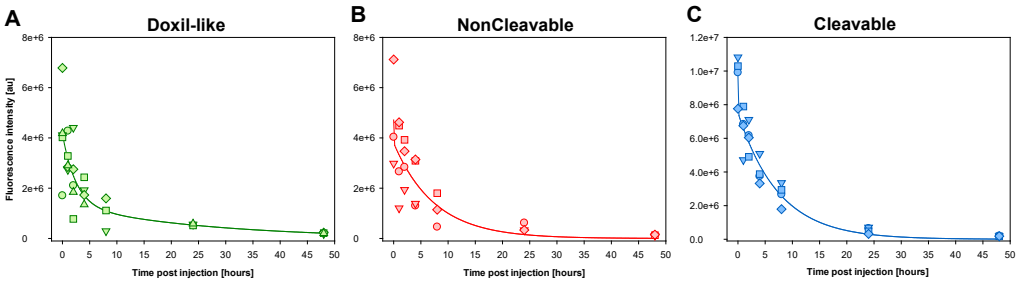

Figure S2: Fluorescence intensity of blood samples as function of time describing the in vivo circulation behaviour of the (A) Doxil-like, (B) NonCleavable and (C) Cleavable liposome. The different symbols depict different animals. (n=5 for each group).

Effect of the enzyme thermolysin on the liposome characteristics

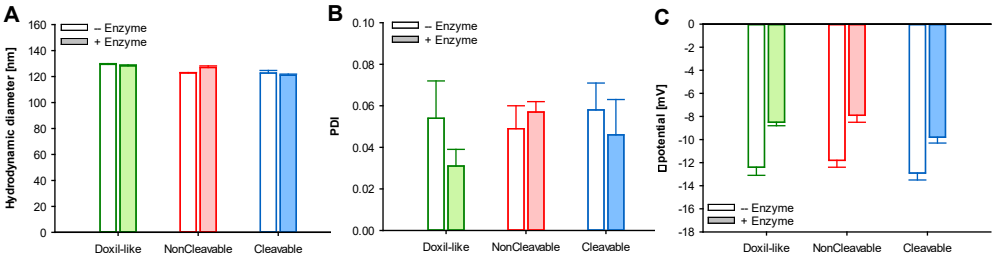

Figure S3: Effect of the addition of the enzyme thermolysin on they (A) Hydrodynamic radius, (B) PDI and (C) Zeta potential of the three liposomes. These experiments have been performed with a different batch of the liposomes.

Fluorescence intensity measured by the small animal optical imager

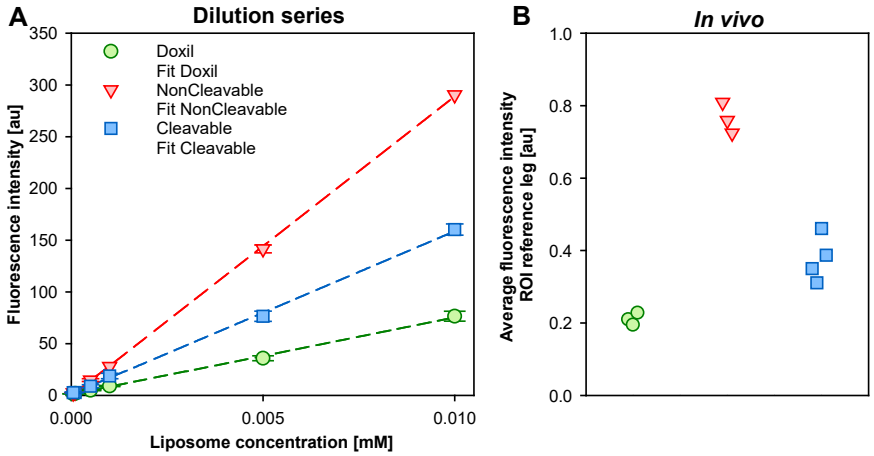

Figure S4: (A) Fluorescence intensity of the Atto700 dye in a dilution series of the fluorophore labelled liposomes measured with the small animal optical imager. Mean and standard deviation are based on the average of n=3. (B) The average fluorescence intensity of an ROI on the non-tumour bearing leg of animals only injected with liposomes approximately 5 minutes after injection confirming the previous observed differences in fluorescence intensity between the liposomes obtained in solution.

Fluorescence intensity measured by a spectrofluorometer

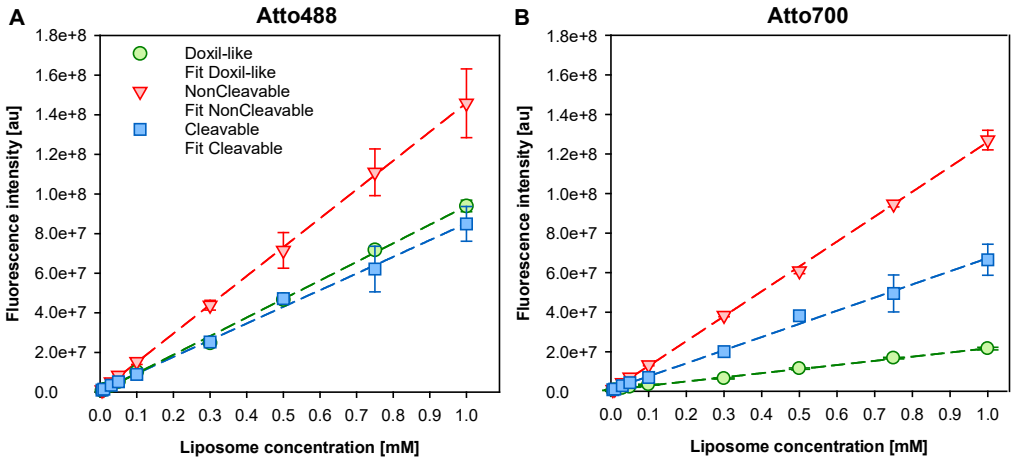

Figure S5: Fluorescence intensity of the (A) Atto488 and (B) Atto700 dye in dilution series of the three liposomes used during the tumour accumulation, biodistribution and microdistribution study measured by a spectrofluorometer. Results on the Atto700 dye agree with the differences obtained from the dilution series and in vivo experiments measured with the small animal imager.

Effect of the enzyme activation buffer and enzyme on the cellular uptake of the liposomes

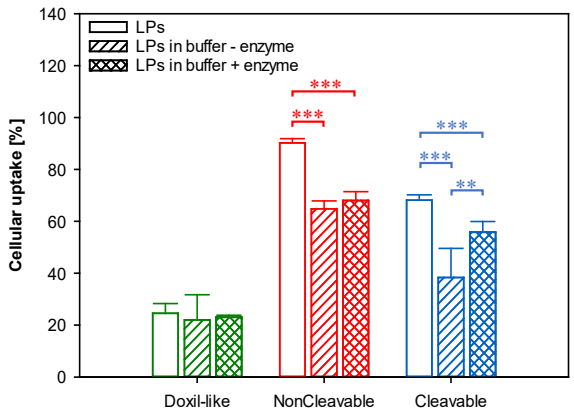

Figure S6: Cellular uptake by PC3 cells of the Doxil-like, NonCleavable and Cleavable liposome when incubated for four hours in growth medium (LPs), growth medium containing the activation buffer for the enzyme (LPs in buffer – enzyme) and growth medium containing the activation buffer supplemented with the enzyme thermolysin (LPs

Selecting ultrasound parameters for optimizing tumour accumulation

The effect of 4 different ultrasound settings (group 2-4, see Table S2) on the tumour accumulation of the Cleavable liposomes was studied. Results of this sub study (see Supplementary Figure S7) were used to choose appropriate ultrasound settings when studying the microdistribution and therapeutic efficacy of the three different liposomes.

Subcutaneous prostate cancer tumours were grown in 32 mice and included in the study when the tumours had reached an average size of 200-300 mm^3. Animals received a 100 µl intravenous bolus injection of 6 mM of Cleavable liposome solution. Mice exposed to ultrasound received 100 µl of SonoVue™ microbubbles followed by 2 minutes of ultrasound towards the tumour bearing leg. Accumulation of liposomes in tumours was measured using a small animal optical imager.

TABLE S2: FIVE DIFFERENT TREATMENT GROUPS FOR SELECTING BEST ULTRASOUND SETTINGS FOR OPTIMIZING TUMOUR ACCUMULATION.

GROUP	Mechanical Index	Number of cycles	Pulse repetition Frequency [Hz]	Treatment time [min]	Number of mice
1	-	-	-	-	6
2	0.4	1 000	0.5	2	6
3	0.4	10 000			7
4	0.8	1 000			6
5	0.8	10 000			7

Selecting ultrasound parameters for optimizing tumour accumulation

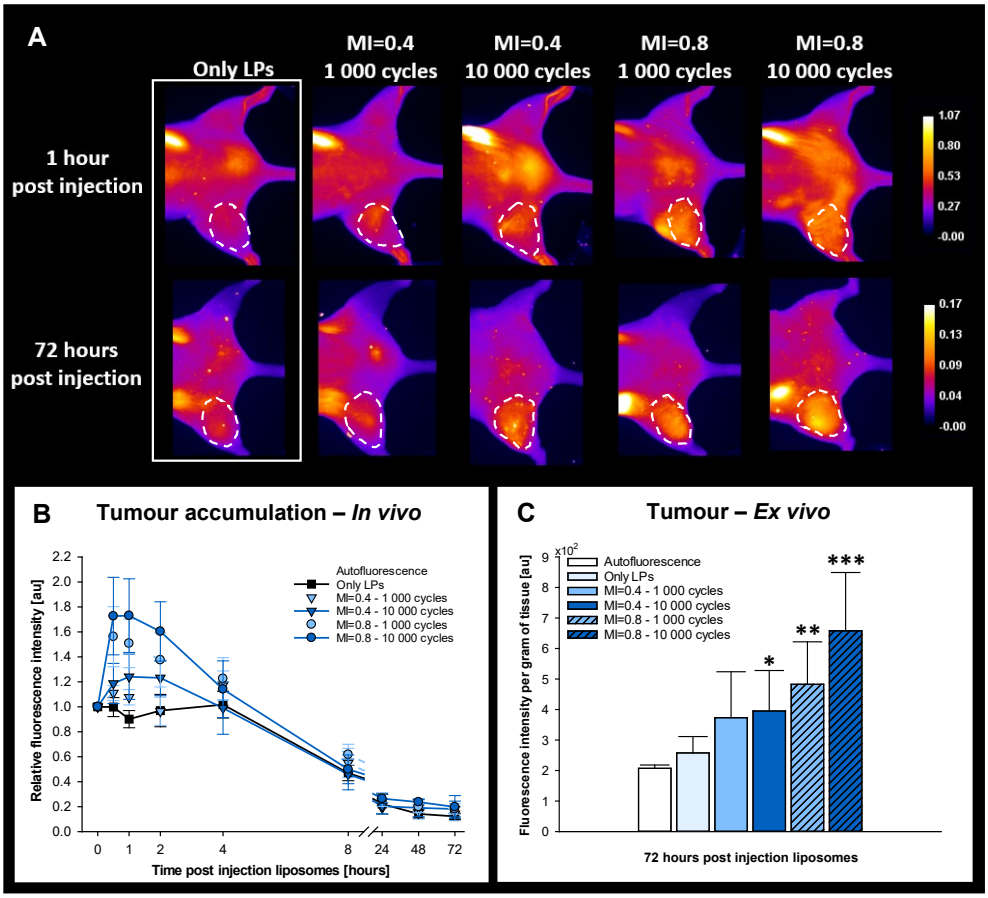

Figure S7: (A) Representative images 1 and 72 hours post injection of the liposomes (LPs) of animals treated with and without ultrasound treatment. Note the difference in colour bar intensities for the top and bottom row of the images. White dashed line shows the tumour ROI. (B) Relative fluorescence intensity in tumour ROI at different timepoints post injection of LPs with and without ultrasound treatment. Grey area represents autofluorescence values based on images taken before injection of the LPs. All ultrasound treatment groups showed statistically significant increase in fluorescence intensity at t=0.5, 1.0 and 2.0 hours. The observed increase was different for the different ultrasound settings used. Mean and standard deviation based on n=6-7 animals. (C) Fluorescence intensity per gram of ex vivo tumour tissue for the different treatment groups at 72 hours post liposome injection. Asterisks show statistically significance with respect to the Only-LPs treatment group. (* $p<0.05$, ** $p<0.01$, *** $p<0.001$)

Relative tumour growth curves of the individual animals

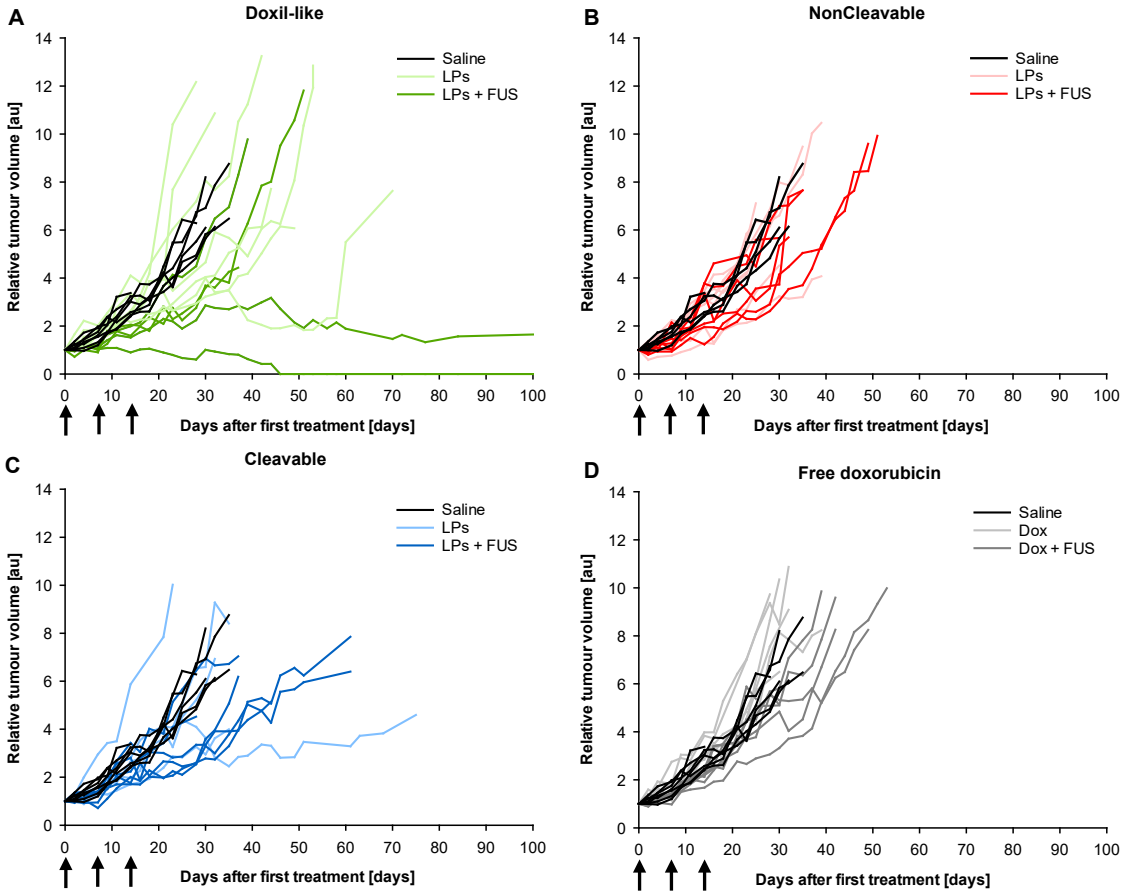

Figure S8: The relative tumour growth curves of the individual animals treated with the (A) Doxil, (B) NonCleavable, (C) Cleavable liposomes and (D) Free doxorubicin. Black solid lines indicate the tumour growth curves of mice that only received an intravenous injection of saline. The bright and dark coloured line indicate the only liposomes (LPs) or free drug group and the MI=0.8 ultrasound treatment group (LPs+FUS), respectively. Treatments took place on day 0, 7 and 14 and are indicated with a black arrow. (*p<0.05, **p<0.01) (D=Doxil-like, NC=NonCleavable, C=Cleavable, DOX=Free doxorubicin, FUS=Focused ultrasound and microbubbles)

Weight curves per treatment group

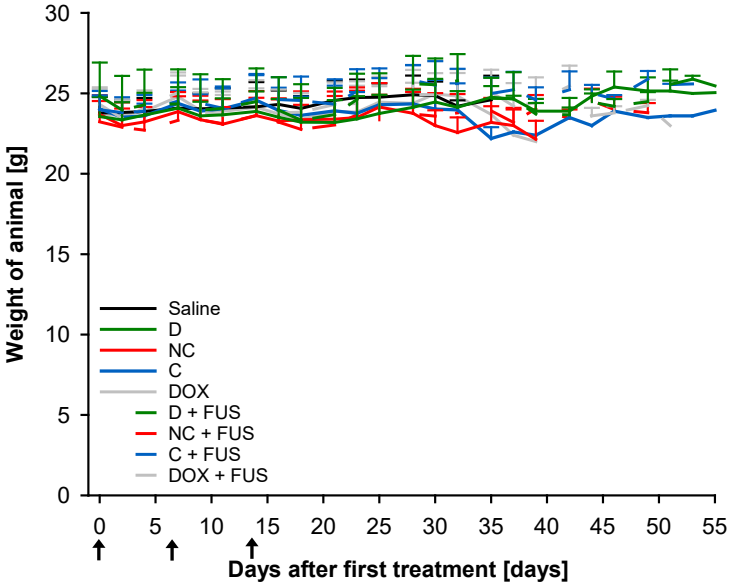

Figure S9: Weight of the animals shown for the first 55 days after the first treatment. Treatments were performed at day 0, 7 and 14 (black arrows). Data are shown as mean and standard deviation. Each group contains 5-7 animals up to day 28 after which animals were euthanized and thereby affecting the mean curve. (D=Doxil-like, NC=NonCleavable, C=Cleavable, DOX=Doxorubicin, FUS=Focused Ultrasound and microbubbles).

Cavitation detection data during detected during ultrasound treatment

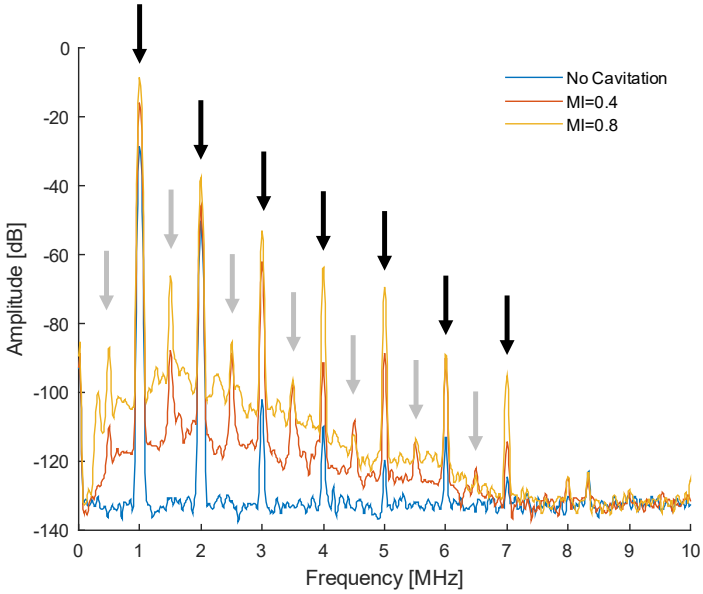

Figure S10: Representative frequency content of the scattered and emission signals from the Sonovue™ microbubbles of time signals detected 10 seconds after start of ultrasound treatment. When no cavitation behaviour is observed (blue), mainly harmonic frequencies (black arrows) dominate the frequency spectrum. The use of MI=0.4 results in an increase in observed sub- and ultra harmonics (grey arrows) and baseline rise. Using MI=0.8 resulted even in higher observed amplitudes for the sub- and ultra harmonics and baseline rise indicating increased cavitation behaviour by the microbubbles. After all microbubbles are cleared from the bloodstream, the noise level of the frequency spectrum will go back to baseline and the harmonic signals will dominate the frequency spectrum again (no cavitation, blue).

In situ zymography – gelatinolytic activity

In situ zymography was used to show the presence of MMP-2 and MMP-9 (gelatinases) in the PC3 xenograft model used. PC3 tumours of untreated animals were excised and submerged in liquid nitrogen and stored at -80 °C freezer prior to sectioning. The first 3000 µm was removed after which 4 sections of 10 µm thick were taken from 5 different levels with 500 µm between each level.

The sections were overlaid with a solution containing 0.1 mg/ml DQ gelatine (ThermoFisher, USA) and 0.5 µg/ml To-Pro-3 iodine solution (ThermoFisher, USA) and incubated for 4 hours at room temperature. DQ-gelatine contains quenched FITC molecules which start to fluoresce on degradation of the DQ-gelatine due to gelatinolytic activity (MMP-2 and MMP-9)[1]. After incubation, sections were rinsed with PBS, mounted with mounting medium and covered with object glass. To test whether the observed fluorescence was due to gelatinolytic activity, control sections were preincubated with 20 mM EDTA (general MMP inhibitor) before adding the DQ Gelatin/To-Pro-3 iodine solution. An Olympus IX83 microscope was used to image the slides, with detection at 525 nm for DQ Gelatine and 666 nm for To-Pro 3.

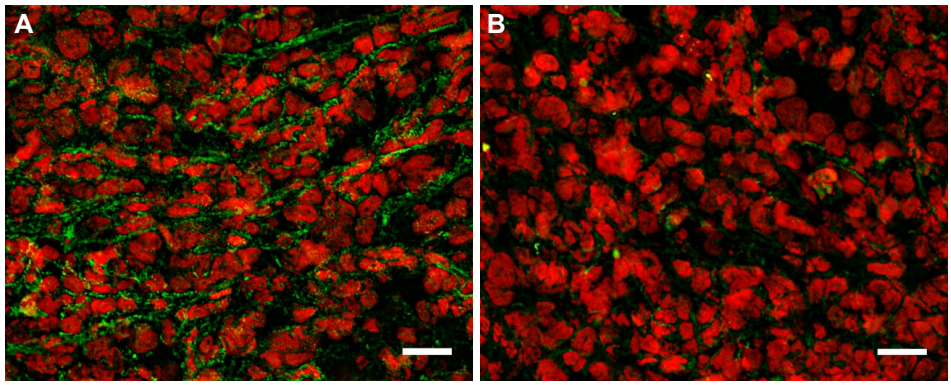

Figure S11: In situ zymography of MMP-2 and MMP-9 activity in prostate cancer xenograft tumour (A) without MMP inhibitor and (B) with MMP-inhibitor. Fluorescence (green) is generated due to gelatinolytic activity (MMP-2 and MMP-9) in the presence of the DQ-gelatine. Adding the MMP inhibitor resulted in reduced fluorescence indicating that the observed fluorescence is due to the presence of the gelatinases MMP-2 and MMP-9. Cell nuclei are shown in red. Scalebar is 20 µm.

Reference

[1] O.R. Mook, C.V. Overbeek, E.G. Ackema, F.V. Maldegem, W.M. Frederiks, In situ localization of gelatinolytic activity in the extracellular matrix of metastases of colon cancer in rat liver using quenched fluorogenic DQ-gelatin, Journal of Histochemistry & Cytochemistry, 51 (2003) 821-829.

PAPER II

Focused ultrasound and microbubble treatment increases delivery of transferrin receptor-targeting liposomes to the brain

Marieke Olsman, Viktoria Sereti, Melina Mühlenpfordt, Kasper Bendix Johnsen, Thomas Lars Andresen, Andrew James Urquhart, Catharina de Lange Davies

Ultrasound in Medicine and Biology | 2021

Ultrasound in Med. & Biol., Vol. 00, No. 00, pp. 1–13, 2021

0301-5629/$ - see front matter

https://doi.org/10.1016/j.ultrasmedbio.2021.01.014

● *Original Contribution*

FOCUSED ULTRASOUND AND MICROBUBBLE TREATMENT INCREASES DELIVERY OF TRANSFERRIN RECEPTOR-TARGETING LIPOSOMES TO THE BRAIN

MARIEKE OLSMAN,* VIKTORIA SERETI,† MELINA MÜHLENPFORDT,* KASPER BENDIX JOHNSEN,† THOMAS LARS ANDRESEN,† ANDREW JAMES URQUHART,† and CATHARINA DE LANGE DAVIES*

* Department of Physics, Norwegian University of Science and Technology, Trondheim, Norway; and † Department of Health Technology, Technical University Denmark, Kongens Lyngby, Denmark

(*Received* 2 *October* 2020; *revised* 6 *January* 2021; *in final from* 13 *January* 2021)

Abstract—The blood-brain barrier (BBB) is a major obstacle to treating several brain disorders. Focused ultrasound (FUS) in combination with intravascular microbubbles increases BBB permeability by opening tight junctions, creating endothelial cell openings, improving endocytosis and increasing transcytosis. Here we investigated whether combining FUS and microbubbles with transferrin receptor-targeting liposomes would result in enhanced delivery to the brain of post-natal rats compared with liposomes lacking the BBB-targeting moiety. For all animals, increased BBB permeability was observed after FUS treatment. A 40% increase in accumulation of transferrin receptor-targeting liposomes was observed in the FUS-treated hemisphere, whereas the isotype immunoglobulin G liposomes showed no increased accumulation. Confocal laser scanning microscopy of brain sections revealed that both types of liposomes were mainly observed in endothelial cells in the FUS-treated hemisphere. The results demonstrate that FUS and microbubble treatment combined with BBB-targeting liposomes could be a promising approach to enhance drug delivery to the brain. (E-mail: marieke.olsman@ntnu.no) **© 2021 The Author(s). Published by Elsevier Inc. on behalf of World Federation for Ultrasound in Medicine & Biology. This is an open access article under the CC BY license (http://creativecommons.org/licenses/by/4.0/).**

Key Words: **Transferrin receptor-targeting, Blood–brain barrier disruption, Ultrasound, Liposomes, Microbubbles.**

INTRODUCTION

The blood-brain barrier (BBB) strictly controls the transport of substances into the brain, impeding the access of most drugs to the brain and preventing efficient treatment of many brain diseases (Abbott et al. 2010; Pardridge 2012). Several approaches for circumventing the BBB (*e.g.,* intranasal delivery, intracerebral/intraventricular injections, chemical mediation) have been proposed, but each of these approaches has several limitations, including low delivery efficiency, damage of healthy tissue and cytotoxic or adverse systemic effects (Rapoport 2000; Dhuria et al. 2010; White et al. 2011; Lochhead and Thorne 2012). To overcome these limitations, non-invasive approaches are highly needed for controlled transient and safe increase in BBB permeability to enable passage of large therapeutics into the brain.

Extensive research has been done on the use of focused ultrasound (FUS) in combination with intravascular microbubbles (MBs) for a transient and safe increase in BBB permeability (Hynynen et al. 2001; Meairs and Alonso 2007; McDannold et al., 2008a; McDannold et al., 2008b; Ting et al. 2012; Burgess and Hynynen 2013; Liu et al. 2014; Burgess et al. 2015; Poon et al. 2016). Successful delivery of chemotherapeutics, nanocarriers, antibodies and stem cells across the BBB after FUS-induced increase in BBB permeability have been reported (Liu et al. 2010; Burgess et al. 2011; Etame et al. 2012; Alkins et al. 2013; Åslund et al. 2015; Kobus et al. 2016; Poon et al. 2016). The exact mechanisms have still not been fully elucidated, but in the presence of ultrasound (US), MBs oscillate and apply biomechanical forces on the blood vessel wall, which potentially facilitate both trans- and paracellular transport across the capillary wall (Sheikov et al.

Address correspondence to: Marieke Olsman, Department of Physics, Norwegian University of Science and Technology, Høgskoleringen 5, 7491 Trondheim, Norway. E-mail: marieke.olsman@ntnu.no

2004; Alonso et al. 2010; Cho et al. 2011; Burgess and Hynynen 2013; Nhan et al. 2013). The resulting increased permeability of the BBB can lead to improved extravasation, distribution in the brain parenchyma and therapeutic efficacy of the drug (Liu et al. 2010; Treat et al. 2012).

To exploit the FUS-induced transport pathways to the fullest, a high concentration of the drug at the site of BBB disruption (BBBD) is favorable. This is often achieved by performing the happened by accident, no comments. FUS treatment directly after intravenous administration of the drug. Another approach is to use drug-loaded MBs, either with or without additional targeting to the BBB, which release the drug locally when sonicated (Ting et al. 2012; Fan et al. 2013, 2015, 2016). In the present study, we combined an FUS-induced increase in BBB permeability with intravenous administration of transferrin receptor (TfR)-targeting liposomes. The TfR has received special interest because its expression is restricted to the brain capillary endothelial cells (BCECs) compared with other endothelial cells (Jefferies et al. 1984). We hypothesize that this combined approach will improve the delivery of the drug nanocarrier across the BBB compared with a drug nanocarrier lacking the targeting moiety.

To study this, TfR-targeting and isotype immunoglobulin G (IgG) liposomes were loaded with cisplatin and labeled with a fluorophore. As a model system, postnatal rats were used because of their high TfR expression in the BBB (Taylor and Morgan 1990; Moos et al. 1998). Magnetic resonance imaging (MRI)-guided FUS was used to increase the permeability of the BBB, and the extent of permeability was evaluated by contrast-enhanced MRI. The amount of cisplatin (a model drug acting as a surrogate marker of the liposomes) entering the brain tissue was quantified by inductively coupled plasma mass spectrometry (ICP-MS). The distribution of liposomes in brain tissue was imaged by confocal laser scanning microscopy (CLSM).

MATERIALS AND METHODS

Materials

Ovine cholesterol, 1,2-distearoyl-*sn*-glycero-3-phosphocholine (DSPC), 2-distearoyl-*sn*-glycero-3-phosphoethanolamine-N-[methoxy(polyethylene glycol)-2000] (DSPE-PEG2000) and 1,2-distearoyl-*sn*-glycero-3-phosphoethanolamine-N-[maleimide(polyethylene glycol)-2000] (ammonium salt; DSPE-PEG2000-maleimide) were purchased from Avanti Polar Lipids, Inc. (Alabaster, USA); 1,1′-dioctadecyl-3,3,3′,3′-tetramethylindodicarbocyanine, 4-chlorobenzenesulfonate salt (DiD), 2-iminothiolane (Traut's reagent), the Micro BCA Protein Assay Kit and mouse IgG2a were from Thermo Fisher Scientific (Hvidovre, Denmark); phosphor, platinum, gallium and iridium elemental standards were from Fluka; and cisplatin (*cis*-diamminedichloroplatinum) and all other chemicals were from Sigma-Aldrich (Brøndby, Denmark). The mouse anti-rat TfR antibody (OX26) was a kind gift from Professor Torben Moos (Aalborg University, Denmark).

Table 1. Molar composition (%) of the liposomes

Lipid	Isotype IgG	Anti-TfR batch 1	Anti-TfR batch 2
DSPC	56.1	56.1	56.3
Chol	38.2	38.2	38.2
DSPE-PEG2000	5	5	5
DSPE-PEG2000-maleimide	0.5	0.5	0.5
DiD	0.2	0.2	—

DSPC=1,2-distearoyl-sn-glycero-3-phosphocholine; Chol = cholesterol; DSPE-PEG2000 = 2-distearoyl-*sn*-glycero-3-phosphoethanolamine-N-[methoxy(polyethylene glycol)-2000]; DSPE-PEG2000-maleimide = 1,2-distearoyl-*sn*-glycero-3-phosphoethanolamine-N-[maleimide(polyethylene glycol)-2000]; DiD = 1,1′-dioctadecyl-3,3,3′,3′-tetramethylindodicarbocyanine, 4-chlorobenzenesulfonate salt; IgG = immunoglobulin G; TfR = transferrin receptor.

Liposome formulation

The molar concentrations of the lipids used in the formulations are listed in Table 1. Lipids and DiD, in case of the fluorophore-labeled formulations, were dissolved in a mixture of *tert*-butanol and Milli-Q purified water (9:1), snap frozen in liquid nitrogen and freeze-dried overnight. The following day, an 8 mg/mL solution of cisplatin was heated to 70°C and used to hydrate the thin lipid layers. During the hydration process the temperature was kept at 70°C and the samples were under constant stirring. Next, the samples were extruded using a high-pressure extruder at 70°C through a 100 nm filter to form small unilamellar vesicles. Thereafter, the formulations were dialyzed twice with phosphate-buffered saline (PBS) for 12 h each to remove un-encapsulated cisplatin.

Antibody thiolation

The liposomes were functionalized with an antibody against either the rat TfR (OX26) or an isotype IgG. The buffer of the antibodies was exchanged to 0.1 M borate and 2 mM dipotassium ethylenediaminetetraacetic acid (pH 8; K_2EDTA) by two rounds of spin filtration using Amicon Ultra-4 Centrifugal Filter Units (molecular-weight cutoff, 30 kDa; Sigma-Aldrich, Brøndby, Denmark) at 4000 *g* and 4°C. Afterwards, the concentration of the antibody was measured using the absorbance at 280 nm of the solution using a NanoDrop 2000c spectrophotometer (Thermo Fisher Scientific, Hvidovre, Denmark) and the extinction coefficient of mouse IgGs (1.37). Traut's reagent was prepared by dissolving it in a borate buffer at a concentration of 2 mg/mL. OX26 or IgG antibodies and Traut's reagent

were mixed with a molar ratio of 1:40. The thiolation reaction was allowed to proceed for 1 h at room temperature under mild agitation. Afterward, the thiolated antibodies were purified from the residual Traut's reagent by spin filtration using Amicon Ultra-4 Centrifugal Filter Units (molecular-weight cutoff, 30 kDa) and PBS at 4000 *g* and 4˚C, twice.

Liposome preparation and purification

Liposomes containing DSPE-PEG2000-maleimide were mixed with thiolated OX26 or IgG antibodies at a molar ratio of 5:1 (as defined by available maleimide groups), the air phase of the container was replaced with N_2 and the antibodies were allowed to conjugate to the liposomes overnight in the dark under mild agitation. The following day, the liposomes were separated from unconjugated antibodies by size-exclusion chromatography, using a Sepharose CL-4B column (1.5 × 20 cm; Sigma-Aldrich, Brøndby, Denmark), PBS as an elution buffer and a flow rate of 1 mL/min. The absorbance at 280 nm of the resulting fractions was measured, and fractions with high absorbance were pooled and up-concentrated using Amicon Ultra-15 Centrifugal Filter Units (molecular-weight cutoff, 100 kDa) centrifuged at 4000 *g* and 4˚C. The fluorescence of the up-concentrated fractions was measured using a microplate reader (Spark, Tecan Trading, Männedorf, Switzerland) and used for pooling liposome-containing fractions.

Liposome characterization

The hydrodynamic radius, polydispersity index and zeta potential of the liposomes were measured using a Zetasizer ZS (Malvern Panalytical Ltd., Malvern, UK), by dilution in PBS for size and polydispersity index measurements and 4-(2-hydroxyethyl)-1-piperazineethanesulfonic acid (HEPES) 5% glucose buffer for zeta potential measurements. Phosphor and platinum concentrations were measured in the final liposome formulations using ICP-MS (see later). The Micro BCA Assay was used to confirm the presence of antibodies in final liposome samples, following the test tube manufacturer's protocol adjusted for microplate volumes.

Animals

Two pregnant Sprague Dawley rats were purchased (Janvier Labs, Le Genest-Saint-Isle, France) and housed separately in individually ventilated cages under conditions free of specific pathogens. Cages were kept in a controlled environment (20−23˚C; humidity, 50%−60%) on a 12 h night/day cycle and the animals had free access to food and sterile water. Housing, nesting material and gnaw sticks were used to enrich the cage. The study included 17 pups with a post-natal age of 14−17 days: 13 for ICP-MS analysis and 4 for confocal microscopy. All experimental procedures were approved by the Norwegian Food Safety Authority.

Magnetic resonance imaging

MRI was performed on a 7.05 T horizontal bore magnet (Biospec 70/20 Avance III, Bruker, Billerica, USA) with an 86 mm volume resonator for radio-frequency transmission and a phased-array rat-brain surface coil for reception.

Before, after and 24 h after BBBD, a T1 fast low-angle shot (FLASH) sequence was acquired to verify the increased BBB permeability by the detection of extravasated gadolinium-based MRI contrast agent (1 mL/kg, 0.5 mmol/mL, Omniscan; GE Healthcare, Chicago, USA), using the following acquisition properties: echo time (TE), 3.5 ms; repetition time (TR), 200 ms; flip angle, 40˚; 12 averages; slice thickness, 0.8 mm. A T2-weighted rapid acquisition with relaxation enhancement image was acquired to detect hemorrhages and edema, with the following acquisition properties: TE, 54 ms; TR, 2000 ms; 14 averages; slice thickness, 0.8 mm. All sequences had a field of view of 20 × 20 mm, with a matrix size of 200 × 200, and 12 slices spaced at 1 mm. MRI acquisition parameters were set using Bruker ParaVision 6.0.1.

BBBD treatment

The timeline of the experimental procedure is presented in Figure 1a. Animals were anesthetized using ~2% isoflurane in medical air (78%) and oxygen (20%), after which they were cannulated in the lateral tail vein. The head was shaved with a hair trimmer and the remaining hair was removed with depilatory cream. Animals were randomly divided into two groups and received an injection of either Anti-TfR or isotype IgG liposomes (Anti-TfR batch 1 and isotype IgG: cisplatin 154 μg/kg; Anti-TfR batch 2, cisplatin 340 μg/kg). The liposomes were allowed to circulate for 1.5 h to give the Anti-TfR liposomes enough time to bind to the BCECs (Kucharz et al. 2020) before the animals were positioned in supine position on the MRI compatible animal bed, received a bolus injection of a gadolinium-based contrast agent and underwent a pre-BBBD MRI scan. During MRI imaging and US experiments, oxygen was excluded from the anesthesia mixture to extend the lifetime of the MBs (Mullin et al. 2011). Respiration rate was closely monitored using a pressure-sensitive probe (SA Instruments, Stony Brook, USA), and body temperature was maintained with a heater during MRI and a heating lamp during US experiments.

The FUS treatment was planned based on the pre-BBBD MRI scan. A 6 × 3 grid of treatment spots—with a spot diameter of 1.6 mm, corresponding to the -3 dB US beam width—was placed on the right hemisphere on

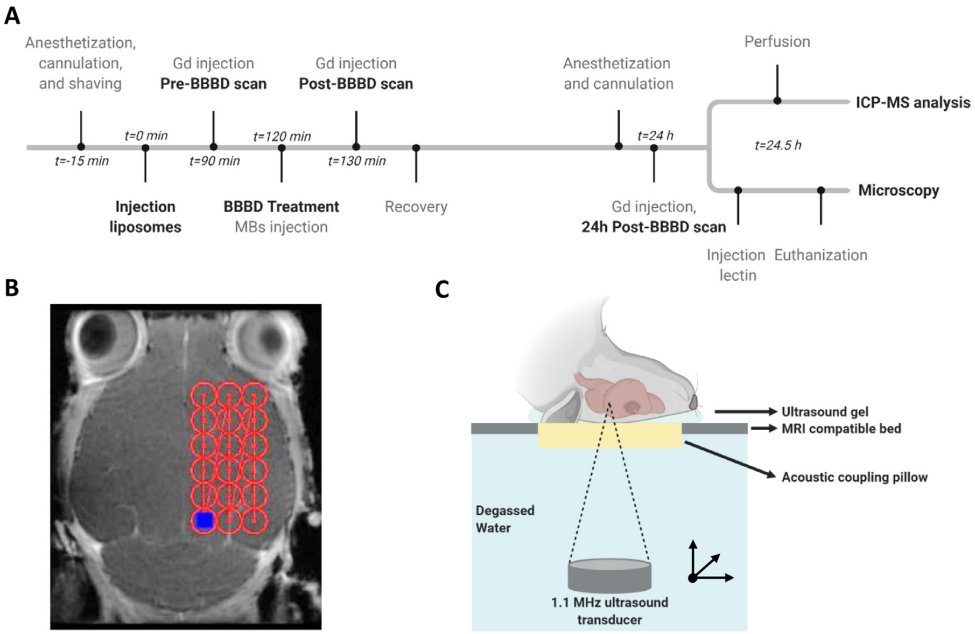

Fig. 1. Treatment timeline, planning and ultrasound setup. (a) Treatment timeline from anesthetization through treatment to ex vivo tissue analysis. (b) Treatment planning. The ultrasound beam scanned a 6 × 3 grid of spots (*red circle*) covering most of the right hemisphere. The blue spot indicates the current location of the ultrasound focus. (c) Ultrasound setup used for BBBD experiment. BBBD = blood-brain barrier disruption; Gd = gadolinium-based contrast agent; MB=microbubbles; ICP-MS=Inductively coupled plasma mass spectrometry; MRI=Magnetic resonance imaging.

an axial image at eye height in the rat's brain (Figure 1b). After the pre-BBBD MRI scan, the MRI bed with the animal was placed in the US setup (RK100, FUS Instruments, Toronto, Canada). The RK100 system consists of an arbitrary function generator, a 53 dB power amplifier, a 1.1 MHz US transducer with a focus at 60 mm and a computer with custom software for treatment planning. The experimental US setup is illustrated in Figure 1c. At 2 h after liposome injection, the animal received a bolus injection of SonoVue MBs (2 mL/kg; Bracco Imaging, Milan, Italy), and 10 s after the injection, the FUS treatment started.

The acoustic pressure was measured to be attenuated by the rat skull with approximately 27% ± 9% (see supplementary information p2), such that an *in situ* peak negative pressure of 0.22−0.29 MPa (corresponding to a mechanical index of 0.21−0.27) was obtained. A burst length of 10 000 cycles, repetition frequency of 0.25 Hz and total treatment time of 3 min were used. After FUS treatment, animals received another bolus injection of gadolinium-based contrast agent, and the MRI bed with the animal was placed back in the scanner and a post-BBBD scan was performed to detect BBBD, edema and hemorrhages.

After the post-BBBD MRI scan, the cannula was removed, the head was cleaned and the animal was taken off anesthesia and placed back in the cage with its dam and other pups. To study whether the permeability of the BBB was still increased at 24 h after BBBD, animals were anesthetized as already described and given an intravenous injection of gadolinium containing contrast agent before undergoing another MR scan (24 h post-BBBD). Thereafter, animals were euthanized with an intraperitoneal injection of pentobarbital (200 μL; concentration, 100 mg/mL) and kept under anesthesia until their breathing halted.

Animals used for measurement of the accumulation of liposomes in the brain by ICP-MS were transcardially perfused with PBS, after which the brain was excised. Animals whose brains were used for CLSM were injected with 50 μL of fluorescein-labeled *Lycopersicon esculentum* tomato lectin (2 mg/mL; Vector Laboratories, Peterborough, UK) to label functional blood vessels. The lectin was allowed to circulate for 5 min, after which the animal was euthanized and the brain excised. All samples were kept frozen until further analysis.

Analysis of BBBD

The degree of BBBD was evaluated by measuring the signal intensity in the T1 MR images using ImageJ (version 1.51j; USA). A square region of interest was drawn around six treatment spots and reused in four consecutive images all at eye height. Large brain structures were avoided. The same region of interest was used on the contralateral hemisphere (control). The ratio of the average intensity between the FUS-treated and control hemisphere was calculated to quantify the degree of BBBD. Visual examination of the T2 images was performed to assess hemorrhages (dark spots).

Inductively coupled plasma mass spectrometry

ICP-MS was used to quantify the amount of cisplatin found in the collected tissue samples. Tissue samples (maximum 100 mg) were digested in aqua regia overnight at 65˚C. Thereafter, samples were diluted in Milli-Q water containing 0.5 ppb iridium, followed by dilution in 2% hydrochloric acid containing 0.5 ppb iridium. Analysis was performed with an iCAP Q ICP-MS system (Thermo Fisher Scientific, Hvidovre, Denmark) fitted with an ASX-520 Autosampler and a ThermoFlex 2500 chiller. Before sample analysis, a TUNE B iCAP Q element mixture (Thermo Fisher Scientific, Hvidovre, Denmark) was used to calibrate the instrument. Serial dilution of an analytical standard platinum solution was used to generate a standard curve with data points in the 0.08−10 ppb range. In addition, the iridium content in each sample was measured as an internal standard. The same procedure was used to quantify the cisplatin content in the liposome formulations.

The phosphor content in the liposome formulation, which is an indicator of phospholipid concentration, was measured by diluting a sample of liposomes in 2% hydrochloric acid containing 0.5 ppb gallium. A standard curve with data points in the range of 25−100 ppm was generated based on serial dilution of an analytical standard phosphor solution.

Brain sectioning for CLSM

Excised brains were mounted transversely on a piece of cork with Tissue-Tek O.C.T. (Sakura, Alphen aan den Rijn, the Netherlands) before samples were submerged in liquid nitrogen.

Of the frozen brain samples, the first 1000 μm from the top was removed, after which three slices of 25 μm thick and two slices of 4 μm thick were taken. The latter two were stained with hematoxylin, erythrosine and saffron for histologic evaluation. This sectioning process was repeated every 900 μm until the whole brain was sectioned.

Confocal laser scanning microscopy

FUS-mediated delivery of the liposomes across the BBB was verified by imaging frozen brain sections with CLSM (LSM 800; Zeiss, Oberkochen, Germany). Before imaging, sections were thawed at room temperature and mounted with Vectashield (Vector Laboratories, Peterborough, UK). Tile scans of the whole brain section were acquired using a 20 × /0.8 Plan-Apochromat air objective lens (image properties: 512 × 512, 16 bit, pixel size 624 nm, 10% overlap between tiles). Lectin was excited with a 488 nm diode laser and emission was detected between 490 and 600 nm. The DiD was excited with a 640 nm laser diode and fluorescence was detected between and 700 nm. A 40 × /1.2 C-Apochromat water objective lens was used to obtain z-stacks of areas in both the FUS-treated and the untreated (control) hemisphere (image properties: 1024 × 1024, 16 bit, pixel size 156 nm, Airy scan, optical slice thickness 1.0 μm). A z-projection image (sum of slices) and 3-D rendering of the z-stack were acquired and used for presentation.

Statistical analysis

Statistical analysis on all data sets was performed with SigmaPlot (version 14.0; Systat Software Inc., San Jose, USA). Depending on the type and number of data sets compared, a paired *t*-test, unpaired *t*-test or one-way analysis of variance with Dunnett's multiple-comparison *post hoc* test was performed. The statistical test used will be specified in the caption of the corresponding figure. A *p* value smaller than 0.05 was considered to indicate statistical significance.

RESULTS

Increased BBB permeability after FUS treatment

FUS exposure in the presence of MBs resulted in a gadolinium-induced increase of the signal intensity, demonstrating that the BBB permeability was increased. Representative T1-weighted FLASH and corresponding T2 MR images before and after (10 min) FUS exposure are shown in Figure 2a. The observed intensity pattern of BBBD corresponded with the 6 × 3 grid of spots used during the FUS treatment and was observed along the coronal and sagittal planes of the brain (Supplementary Figure S1a). In all animals, the corresponding T2 images showed an increased signal intensity throughout the FUS-treated hemisphere (Supplementary Figure S1b), indicating the presence of edema. No clear spots representing hemorrhages were detected in either the T1 FLASH or T2 images, but the presence of hemorrhages could not be fully ruled out.

The extent of BBBD was evaluated based on the MR image intensity in the FUS-treated hemisphere relative to the control hemisphere (Fig. 2b). The permeability of the

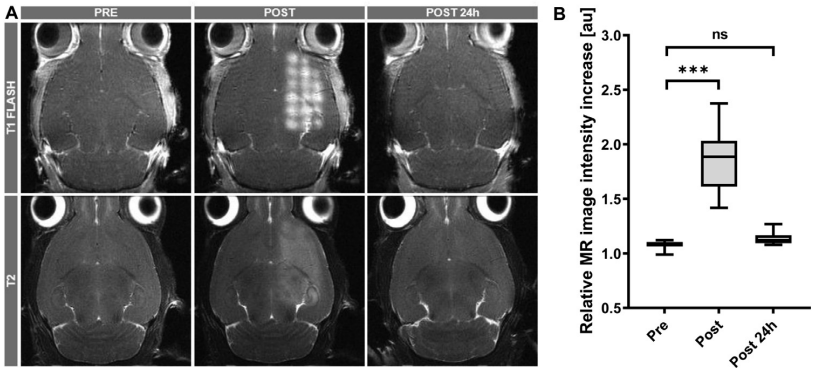

Fig. 2. (a) Representative T1 fast low-angle shot (FLASH) and T2 images of an animal pre, post and 24 h post focused ultrasound (FUS) treatment. Clear enhanced signal intensity is observed in the T1 FLASH and T2 images taken after FUS treatment, indicating successful disruption of the blood-brain barrier and the presence of edema, respectively. No clear hemorrhage spots can be observed in the T2 images. (b) Magnetic resonance image intensity increase in the FUS-treated hemisphere relative to the control hemisphere in the T1 FLASH images at the three time points. Asterisks show statistical significance (***$p < 0.001$, ns=not significant). The p values were derived from a one-way analysis of variance with Dunnett's multiple-comparison *post hoc* test, comparing the values of the post and post 24 h data sets to the pre-BBBD data set. Boxplot based on n = 17 animals.

BBB was successfully enhanced in all animals, but to different extents (Supplementary Figure S2). Between the animals treated with either the isotype IgG or the Anti-TfR liposomes, no difference in degree of BBBD was observed (Supplementary Figure S3). An increase in MR image intensity of approximately 1.7 times between the two hemispheres was observed in T1 images taken after FUS treatment, which was a statistically significant difference relative to the pre-BBBD scan. At 24 h after FUS treatment, the relative MR image-intensity increase had returned to pre-BBBD values.

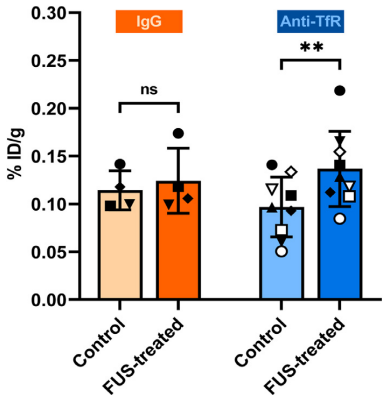

Fig. 3. Accumulation of cisplatin in the control and focused ultrasound (FUS)-treated hemispheres after injection with either the isotype immunoglobulin G (IgG) (*orange*) or the transferrin receptor-targeting liposome (Anti-TfR) (*blue*). Each symbol depicts an animal. In case of the Anti-TfR treatment group, black and white symbols indicate animals treated with batch 1 or batch 2 of the Anti-TfR liposome, respectively. The bar plot is presented as mean with standard deviations. Asterisks show statistical significance (**$p < 0.01$, ns=not significant). The p values are derived from a paired t-test; $n = 4$ and $n = 9$ for the isotype IgG and Anti-TfR treatment groups, respectively. %ID/g indicates percentage of injected dose per gram of tissue.

Increased accumulation of Anti-TfR liposomes in FUS-treated hemisphere measured by ICP-MS

FUS and MBs increased the accumulation of Anti-TfR liposomes by approximately 40%, whereas animals treated with the isotype IgG liposomes showed comparable accumulation in both hemispheres at 24 h after treatment (Figure 3). This time point was chosen to give the liposomes sufficient time to cross the BBB and diffuse into the brain parenchyma. Animals were perfused before tissue samples of each hemisphere were extracted, to remove cisplatin-loaded liposomes in circulation and avoid contamination of samples. Two batches of Anti-TfR liposomes were prepared, to have enough liposomes to inject the animals. The different formulations and batches showed similar liposomal characteristics (*e.g.,* diameter, Zeta potential; Table 2).

Liposomes in the FUS-treated hemisphere mainly observed in BCECs

Building upon the findings that FUS treatment increased the delivery of the Anti-TfR liposomes, a couple of brains from treated animals ($n = 2$ per liposome) were sectioned and imaged with CLSM to verify the presence of liposomes in the brain tissue. Sections from

Table 2. Characteristics of the cisplatin-loaded liposomes.

Liposome	Diameter, nm	Zeta potential, mV	PDI	CisPt concentration, mg/mL
Isotype IgG	178 ± 1.5	−11.7 ± 0.5	0.145 ± 0.02	0.054
Anti-TfR batch 1	180 ± 2.0	−10.6 ± 0.6	0.125 ± 0.01	0.054
Anti-TfR batch 2	181 ± 0.7	−13.5 ± 0.4	0.133 ± 0.018	0.093

PDI=polydispersity index; CisPt = cisplatin; IgG = immunoglobulin G; Anti-TfR = transferrin receptor-targeting.

different depths of the brain were imaged by CLSM and compared with the corresponding T1 FLASH MR images. In sections whose corresponding MR image showed clear gadolinium-enhanced contrast, the liposomes in the FUS-treated hemisphere seemed to be located in clusters (Figure 4a, 4e) corresponding to the grid of spots used during the FUS treatment (Figure 1b) and the gadolinium-enhanced contrast observed in the post-BBBD MRI scan (Figure 4d, 4h). Superimposing the liposome channel of the CLSM image with the corresponding MR image illustrated this more clearly (Supplementary Figure S4). Different extents of BBBD were observed at different levels of the brain. In MR images with low gadolinium-enhanced contrast, no clear pattern or increase in liposomal accumulation could be visually observed in the corresponding CLSM tile scan (Supplementary Fig. S5).

To determine whether the brain accumulation observed was owing to transport across the BBB and presence of the liposomes in the brain parenchyma, high-magnification CLSM was performed. In the control hemisphere, both liposomes were located in the blood vessels and no liposomes were observed in the brain parenchyma (Figure 5). In the FUS-treated hemisphere, both liposomes were observed either as diffusively staining BCECs or as a spotted structure aligned with the lectin staining. Representative CLSM images are shown in Figures 6 and 7 for animals treated with the isotype IgG and the Anti-TfR liposome, respectively. The corresponding 3-D renderings showed the location of the liposomes with respect to the lectin staining more clearly (Figsure 6b and 7b). In a few cases, a small number of

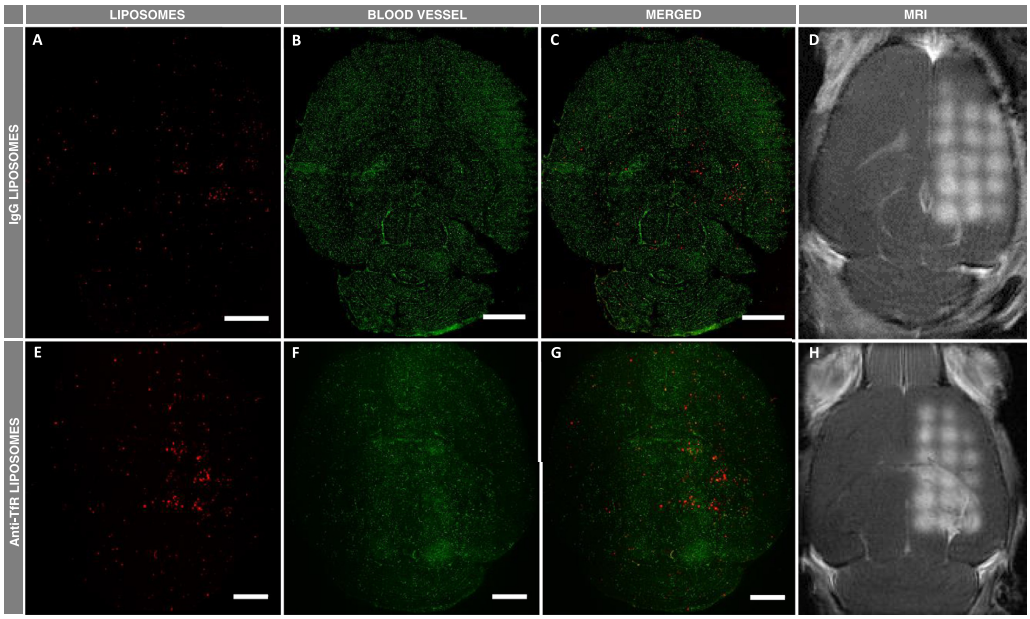

Fig. 4. Confocal laser scanning microscopy tile scans and corresponding magnetic resonance images of animals treated with the isotype immunoglobulin (IgG) (upper panel) and transferrin receptor-targeting (Anti-TfR) (lower panel) liposomes. (a, e) Liposomes (*red*) and (b, f) blood vessels (*green*) are shown separately and (c, g) merged. (d, h) Corresponding magnetic resonance images have been selected based on the brain structures observed in the tile scan. Scale bar is 2000 μm. MRI=magnetic resonance imaging.

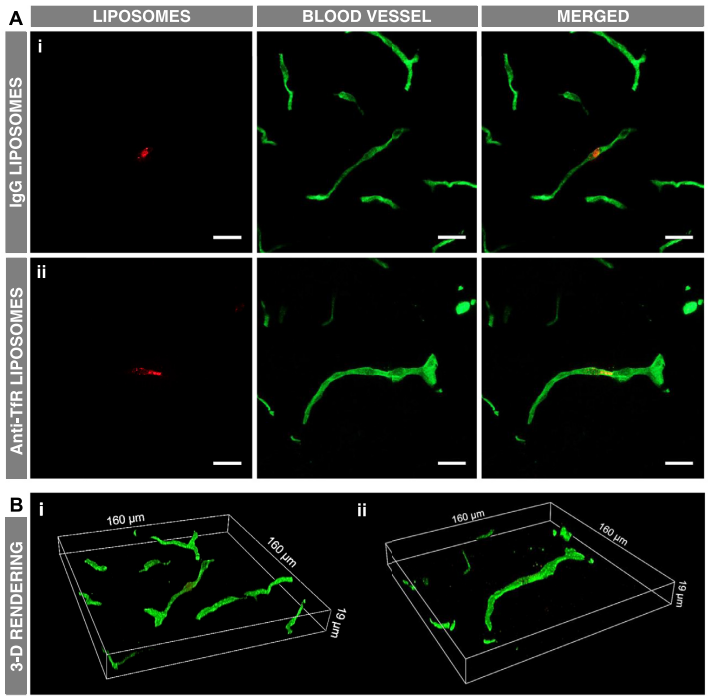

Fig. 5. (a) Representative confocal laser scanning microscopy images acquired in the control hemisphere of animals treated with the (i) isotype immunoglobulin G (IgG) and (ii) transferrin receptor-targeting (Anti-TfR) liposomes. Liposomes (*red*) and blood vessels (*green*) are shown separately and merged. Scale bar is 20 μm. (b) 3-D renderings of the z-stacks of the images shown in (a), verifying the intravascular location of both liposomes. Images were obtained with a 40 × /1.2 water objective lens.

both types of liposomes were observed in the brain parenchyma (Supplementary Figsure S6 and S7).

DISCUSSION

Even after decades of research, the BBB continues to be a major obstacle in treating several brain disorders (Abbott et al. 2010). Nanomedicine shows potential to enable targeted delivery to the brain by decorating drug-loaded nanoparticles with BBB-targeting ligands, resulting in receptor-mediated uptake and transport across the BBB (Sharma et al. 2019). Here we used liposomes functionalized with OX26, a well-known antibody against the rat TfR, which does not compete with endogenous transferrin (Pardridge 2015). In previous work, the OX26 antibody has shown good specificity toward the rat TfR both *in vitro* and *in vivo*, and liposomes conjugated with the OX26 antibody have shown good targeting ability toward the brain microvasculature in post-natal rats (Johnsen et al. 2017; Thomsen et al. 2019). In the present work, we have combined intravenous injection of Anti-TfR liposomes with FUS-induced increase of BBB permeability to investigate if this approach enhanced the delivery of the Anti-TfR liposomes across the BBB compared with liposomes lacking the targeting moiety.

The liposomes were given 2 h to circulate and attach to the BBB before MBs were injected and FUS was applied. Previous studies have shown good accumulation of TfR-targeted liposomes at the BBB at this time point, and shown comparable amounts of the isotype IgG liposomes and TfR-targeted liposomes still in circulation (Johnsen et al. 2017; Kucharz et al. 2020). US settings used were in the same range as those published by others who achieved safe, local and transient BBBD (McDannold et al. 2008a). In MR images obtained directly after FUS treatment, clear extravasation of the gadolinium contrast agent into the brain parenchyma was observed, showing successful FUS-induced increase of the BBB permeability.

Delivery of the cisplatin-containing liposomes to the brain was quantified by ICP-MS, and the analysis showed a statistically significant increase in brain uptake

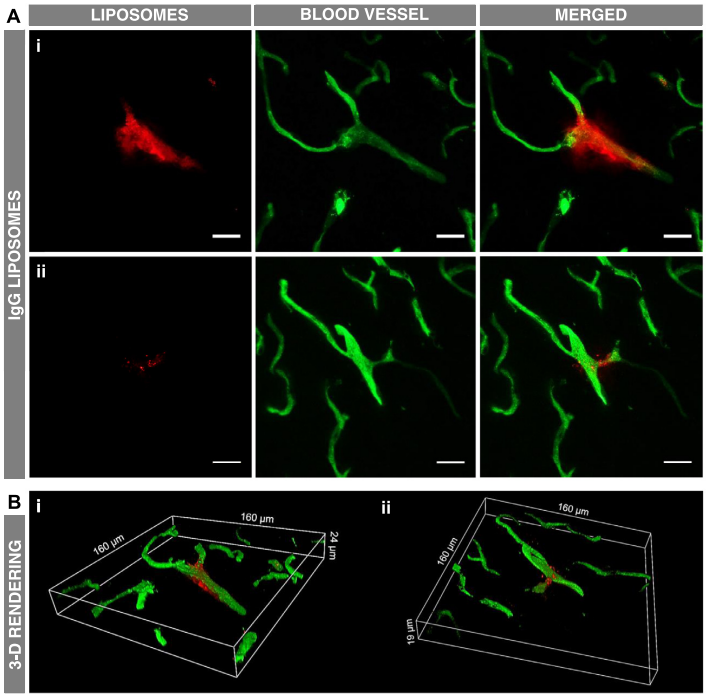

Fig. 6. (a) Representative confocal laser scanning microscopy images acquired in the focused ultrasound-treated hemisphere of animals treated with the isotype immunoglobulin G (IgG) liposome. Liposomes (*red*) and blood vessels (*green*) are shown separately and merged. Liposomes were found to either (i) diffusively stain endothelial cells or (ii) appear as spots aligned with the lectin staining. Scale bar is 20 μm. (b) 3-D renderings of the z-stacks of the images shown in (a), verifying the extravascular location of the liposomes. Images were obtained with a 40 × /1.2 water objective lens.

of the Anti-TfR liposomes in the FUS-treated hemisphere compared with the control hemisphere. Even though a similar degree of BBBD was obtained in animals receiving the IgG liposomes, no increased uptake of the IgG liposomes in the FUS-treated hemisphere was observed.

Possible FUS-induced routes of extravasation are opening of tight junctions, endothelial cell openings (*i.e.,* pore and channel formation), improved endocytosis and increased transcytosis (Sheikov et al. 2004, 2008). While both the isotype IgG and Anti-TfR liposomes might exploit these routes, it is expected that owing to the targeting moiety, the Anti-TfR liposome will benefit mostly from improved endocytosis and transcytosis. FUS-induced increase of clathrin-mediated endocytosis has been reported in different cell types (Hauser et al. 2009; Tardoski et al. 2015; Fekri et al. 2016), which is suggested to most likely be the internalization pathway of TfR-targeting liposomes after receptor binding (Johnsen and Moos 2016). Even though these studies were performed *in vitro*, FUS-induced increase of clathrin-mediated endocytosis could explain the observed increased brain uptake of the Anti-TfR liposomes in the FUS-treated hemisphere compared with the isotype IgG liposomes.

In the control hemisphere, both liposomes accumulated to the same degree. Surprisingly, the Anti-TfR liposome did not perform better than the IgG liposome despite its targeting moiety toward the BBB. Besides the antibody attachment, the lipid composition and physicochemical characteristics of the two liposomes are similar. A possible explanation for this comparable uptake between the isotype IgG and Anti-TfR liposomes might be that IgG liposomes are capable of fusing with the membrane of BCECs, as previously reported (Lindqvist et al. 2016; Hu et al. 2017). Another explanation could be that the 24 h time point was too late to detect any difference between the liposomes. In previous work, no difference in BCEC uptake of the isotype IgG and Anti-TfR liposomes at 24 h was observed, whereas a clear difference was observable at an earlier time point (Johnsen et al. 2017). However, in that study, a clear difference in

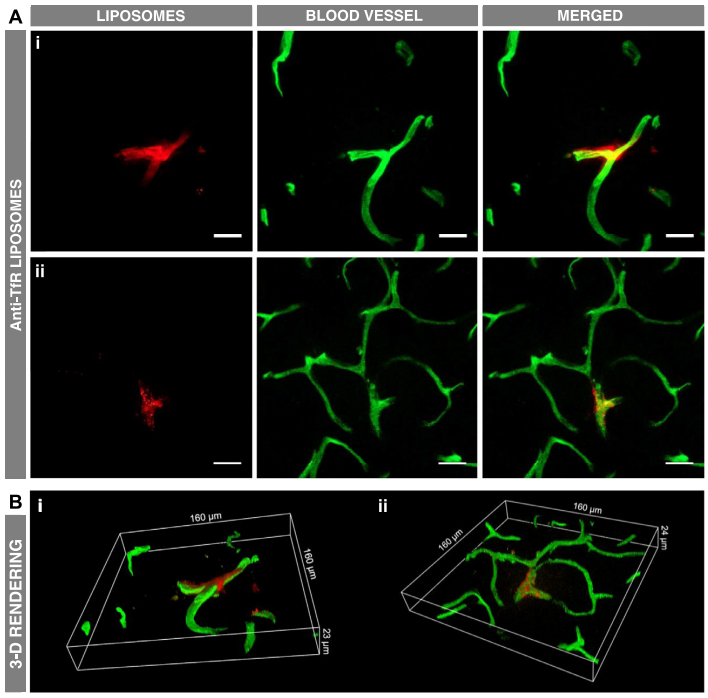

Fig. 7. (a) Representative confocal laser scanning microscopy images acquired in the focused ultrasound-treated hemisphere of animals treated with the transferrin receptor-targeting (Anti-TfR) liposome. Liposomes (*red*) and blood vessels (*green*) are shown separately and merged. Liposomes were found to either (i) diffusively stain endothelial cells or (ii) appear as a spotted structure aligned with the lectin staining. Scale bar is 20 μm. (b) 3-D renderings of the z-stacks of the images shown in (a), verifying the extravascular location of the liposomes. Images were obtained with a 40 × /1.2 water objective lens.

favor of the Anti-TfR liposomes was still observed in the brain parenchyma after 24 h.

While ICP-MS was performed to quantitatively analyze the effect of FUS treatment on the accumulation of the liposomes, CLSM was performed on brain sections to qualitatively determine the location of the liposomes within the brain tissue. From CLSM tile scans, it was observed that the distribution of liposomes corresponded to gadolinium-enhanced contrast in the MR images (*i.e.,* liposomes accumulated at the location of BBBD). In high-magnification CLSM images acquired in sections of the FUS-treated hemisphere, both liposomes were found to either diffusively stain BCECs or form spots aligned with the lectin staining. Because the displacement of the liposomal fluorescence was only minimal with respect to the lectin staining, it was believed that the observed liposomes were most likely inside the BCECs. Because this kind of staining pattern was not observed for both liposomes in the control hemisphere, it was assumed that the observed accumulation of both the IgG and Anti-TfR liposomes in BCECs was induced by the FUS treatment. The more spotted staining could represent liposomes in intracellular vesicles, and the more diffuse staining could represent intracellular degraded liposomes in the cytoplasm. Both have been observed *in vitro* for Anti-TfR liposomes (Cerletti et al. 2000). Only a small number of both liposomes were observed in the brain parenchyma of the FUS-treated hemisphere, and none in the brain parenchyma of the control hemisphere.

In case of the Anti-TfR liposomes, the mechanism of transferrin receptor-mediated uptake of the liposomes is still not fully understood. Most likely, the TfR-targeted liposomes are endocytosed into clathrin-coated vesicles, similar to the endocytosis of endogenous transferrin complex (Johnsen and Moos 2016). What exactly happens to the TfR-targeted liposomes during the intracellular sorting seems to be affected by the number of antibodies or ligands (Huwyler et al. 1996; Yuan and Zhang 2010) and size and type of the vehicle conjugated to the antibody

(Hatakeyama et al. 2004; Yuan and Zhang 2010). The affinity of the antibody to the TfR will most likely also affect the fate of the TfR-targeted liposomes, but its effect on intracellular sorting and transcytosis has mainly been studied for the use of solely antibodies (Yu et al. 2011; Bien-Ly et al. 2014). Different degrees of brain uptake, intracellular locations of the liposomes and locations of drug release have been observed when these parameters are varied.

Others have hypothesized that drug vehicles decorated with a high-affinity antibody will result in the liposome being transported back into the lumen and intracellularly degraded, with inefficient drug release on the abluminal side (Johnsen and Moos 2016). The OX26 antibody used here is known to have a high affinity toward the transferrin receptor, which could therefore be the reason for the accumulation of the Anti-TfR liposomes in BCECs.

A minimal amount of liposomal fluorescence was observed in the brain parenchyma, which indicates that only a few liposomes were transported into the brain parenchyma by transcytosis or by exploiting the opened tight junctions. However, this does not mean that delivery of cisplatin to the abluminal side was unsuccessful. It has been hypothesized that the cargo of liposomes (*i.e.,* cisplatin) might be released on the abluminal side owing to its endosomal escape during intracellular sorting (Johnsen and Moos 2016). Liposomes that manage to cross the BCEC layer will encounter the basement membrane, which can limit the passage of nanoparticles (Muldoon et al. 1999; Thomsen et al. 2017). The physicochemical characteristics (*e.g.,* charge) of the drug carrier used will most likely determine the successfulness of crossing the basement membrane (Muldoon et al. 1999; Lieleg et al. 2009). After crossing the basement membrane, the liposomes need to distribute through the brain parenchyma by a diffusion-driven process which depends on particle size (Wolak and Thorne 2013; Nance et al. 2014). A drug carrier size of around 100 nm has been suggested to be most efficient in terms of drug delivery across the BBB and diffusion through the brain parenchyma (Gao and Jiang 2006). Diffusion of the relatively large liposome (diameter ~180 nm) used in this study could explain why the liposomal fluorescence was only minimally displaced with respect to the lectin staining.

Even though the exact location of the cisplatin in the brain tissue (*i.e.,* in the endothelial cell or brain parenchyma) is unknown, the increased accumulation demonstrates that FUS and MBs in combination with TfR-targeting liposomes could be a promising approach to enhance drug delivery to the brain.

CONCLUSION

FUS in combination with MBs resulted in an increased delivery of TfR-targeted liposomes to brain tissue, whereas no increased delivery of the isotype IgG liposomes was observed. In the FUS-treated hemisphere, both the isotype IgG and Anti-TfR liposomes were found to mainly associate with BCECs, and only a minimal number of liposomes were found in the brain parenchyma.

Acknowledgments—We thank Torben Moos, Aalborg University, for providing the OX26 antibody and Sofie Snipstad and Sigrid Berg for their technical support with the FUS instrumentation. MRI was performed at the MR Core Facility, Norwegian University of Science and Technology (NTNU). We acknowledge Deborah Hill for her technical assistance with the MRI. Housing of the animals was provided by the Comparative Medicine Core Facility (NTNU). Tissue sections were prepared by the Cellular and Molecular Imaging Core Facility (NTNU). We thank Astrid Bjørkøy and the Centre for Advanced Microscopy at the Faculty of Natural Sciences (NTNU) for technical assistance with CLSM. Illustrations were created with BioRender.com. The project was internally funded by the Norwegian University of Science and Technology and the Technical University of Denmark. Thomas Lars Andresen acknowledges generous support from the Lundbeck Foundation Research Initiative on Brain Barriers and Drug Delivery (www.ribbdd.dk; grant R155-2013-14113).

Conflict of interest disclosure—The authors declare no competing interest.

SUPPLEMENTARY MATERIALS

Supplementary material associated with this article can be found in the online version at doi:10.1016/j.ultrasmedbio.2021.01.014.

REFERENCES

Abbott NJ, Patabendige AA, Dolman DE, Yusof SR, Begley DJ. Structure and function of the blood-brain barrier. Neurobiol Dis 2010;37:13–25.

Alkins R, Burgess A, Ganguly M, Francia G, Kerbel R, Wels WS, Hynynen K. Focused ultrasound delivers targeted immune cells to metastatic brain tumors. Cancer Res 2013;73:1892–1899.

Alonso A, Reinz E, Jenne JW, Fatar M, Schmidt-Glenewinkel H, Hennerici MG, Meairs S. Reorganization of gap junctions after focused ultrasound blood-brain barrier opening in the rat brain. J Cereb Blood Flow Metab 2010;30:1394–1402.

Åslund AK, Berg S, Hak S, Mørch Ý, Torp SH, Sandvig A, Widerøe M, Hansen R, de Lange Davies C. Nanoparticle delivery to the brain—by focused ultrasound and self-assembled nanoparticle-stabilized microbubbles. J Control Release 2015;220:287–294.

Bien-Ly N, Yu YJ, Bumbaca D, Elstrott J, Boswell CA, Zhang Y, Luk W, Lu Y, Dennis MS, Weimer RM, Chung I, Watts RJ. Transferrin receptor (TfR) trafficking determines brain uptake of TfR antibody affinity variants. J Exp Med 2014;211:233–244.

Burgess A, Ayala-Grosso CA, Ganguly M, Jordao JF, Aubert I, Hynynen K. Targeted delivery of neural stem cells to the brain using MRI-guided focused ultrasound to disrupt the blood-brain barrier. PLoS One 2011;6:e27877.

Burgess A, Hynynen K. Noninvasive and targeted drug delivery to the brain using focused ultrasound. ACS Chem Neurosci 2013;4:519–526.

Burgess A, Shah K, Hough O, Hynynen K. Focused ultrasound-mediated drug delivery through the blood-brain barrier. Expert Rev Neurother 2015;15:477–491.

Cerletti A, Drewe J, Fricker G, Eberle AN, Huwyler J. Endocytosis and transcytosis of an immunoliposome-based brain drug delivery system. J Drug Target 2000;8:435–446.

Cho EE, Drazic J, Ganguly M, Stefanovic B, Hynynen K. Two-photon fluorescence microscopy study of cerebrovascular dynamics in ultrasound-induced blood-brain barrier opening. J Cereb Blood Flow Metab 2011;31:1852–1862.

Dhuria SV, Hanson LR, Frey WH, II. Intranasal delivery to the central nervous system: mechanisms and experimental considerations. J Pharm Sci 2010;99:1654–1673.

Etame AB, Diaz RJ, O'Reilly MA, Smith CA, Mainprize TG, Hynynen K, Rutka JT. Enhanced delivery of gold nanoparticles with therapeutic potential into the brain using MRI-guided focused ultrasound. Nanomedicine 2012;8:1133–1142.

Fan CH, Chang EL, Ting CY, Lin YC, Liao EC, Huang CY, Chang YC, Chan HL, Wei KC, Yeh CK. Folate-conjugated gene-carrying microbubbles with focused ultrasound for concurrent blood-brain barrier opening and local gene delivery. Biomaterials 2016;106:46–57.

Fan CH, Ting CY, Chang YC, Wei KC, Liu HL, Yeh CK. Drug-loaded bubbles with matched focused ultrasound excitation for concurrent blood-brain barrier opening and brain-tumor drug delivery. Acta Biomater 2015;15:89–101.

Fan CH, Ting CY, Liu HL, Huang CY, Hsieh HY, Yen TC, Wei KC, Yeh CK. Antiangiogenic-targeting drug-loaded microbubbles combined with focused ultrasound for glioma treatment. Biomaterials 2013;34:2142–2155.

Fekri F, Delos Santos RC, Karshafian R, Antonescu CN. Ultrasound microbubble treatment enhances clathrin-mediated endocytosis and fluid-phase uptake through distinct mechanisms. PLoS One 2016;11 e0156754.

Gao K, Jiang X. Influence of particle size on transport of methotrexate across blood brain barrier by polysorbate 80-coated polybutylcyanoacrylate nanoparticles. Int J Pharm 2006;310:213–219.

Hatakeyama H, Akita H, Maruyama K, Suhara T, Harashima H. Factors governing the in vivo tissue uptake of transferrin-coupled polyethylene glycol liposomes in vivo. Int J Pharm 2004;281:25–33.

Hauser J, Ellisman M, Steinau HU, Stefan E, Dudda M, Hauser M. Ultrasound enhanced endocytotic activity of human fibroblasts. Ultrasound Med Biol 2009;35:2084–2092.

Hu Y, Rip J, Gaillard PJ, de Lange ECM, Hammarlund-Udenaes M. The impact of liposomal formulations on the release and brain delivery of methotrexate: An in vivo microdialysis study. J Pharm Sci 2017;106:2606–2613.

Huwyler J, Wu D, Pardridge WM. Brain drug delivery of small molecules using immunoliposomes. Proc Natl Acad Sci U S A 1996;93:14164–14169.

Hynynen K, McDannold N, Vykhodtseva N, Jolesz FA. Noninvasive MR imaging-guided focal opening of the blood-brain barrier in rabbits. Radiology 2001;220:640–646.

Jefferies WA, Brandon MR, Hunt SV, Williams AF, Gatter KC, Mason DY. Transferrin receptor on endothelium of brain capillaries. Nature 1984;312:162–163.

Johnsen KB, Burkhart A, Melander F, Kempen PJ, Vejlebo JB, Siupka P, Nielsen MS, Andresen TL, Moos T. Targeting transferrin receptors at the blood-brain barrier improves the uptake of immunoliposomes and subsequent cargo transport into the brain parenchyma. Sci Rep 2017;7:10396.

Johnsen KB, Moos T. Revisiting nanoparticle technology for blood-brain barrier transport: Unfolding at the endothelial gate improves the fate of transferrin receptor-targeted liposomes. J Control Release 2016;222:32–46.

Kobus T, Zervantonakis IK, Zhang Y, McDannold NJ. Growth inhibition in a brain metastasis model by antibody delivery using focused ultrasound-mediated blood-brain barrier disruption. J Control Release 2016;238:281–288.

Kucharz K, Kristensen K, Johnsen KB, Lund MA, Lønstrup M, Moos T, Andresen TL, Lauritzen MJ. Post-capillary venules is the locus for transcytosis of therapeutic nanoparticles to the brain. bioRxiv 2020; 2020.06.05.133819.

Lieleg O, Baumgartel RM, Bausch AR. Selective filtering of particles by the extracellular matrix: an electrostatic bandpass. Biophys J 2009;97:1569–1577.

Lindqvist A, Friden M, Hammarlund-Udenaes M. Pharmacokinetic considerations of nanodelivery to the brain: Using modeling and simulations to predict the outcome of liposomal formulations. Eur J Pharm Sci 2016;92:173–182.

Liu HL, Fan CH, Ting CY, Yeh CK. Combining microbubbles and ultrasound for drug delivery to brain tumors: current progress and overview. Theranostics 2014;4:432–444.

Liu HL, Hua MY, Chen PY, Chu PC, Pan CH, Yang HW, Huang CY, Wang JJ, Yen TC, Wei KC. Blood-brain barrier disruption with focused ultrasound enhances delivery of chemotherapeutic drugs for glioblastoma treatment. Radiology 2010;255:415–425.

Lochhead JJ, Thorne RG. Intranasal delivery of biologics to the central nervous system. Adv Drug Deliv Rev 2012;64:614–628.

McDannold N, Vykhodtseva N, Hynynen K. Blood-brain barrier disruption induced by focused ultrasound and circulating preformed microbubbles appears to be characterized by the mechanical index. Ultrasound Med Biol 2008a;34:834–840.

McDannold N, Vykhodtseva N, Hynynen K. Effects of acoustic parameters and ultrasound contrast agent dose on focused-ultrasound induced blood-brain barrier disruption. Ultrasound Med Biol 2008b;34:930–937.

Meairs S, Alonso A. Ultrasound, microbubbles and the blood-brain barrier. Prog Biophys Mol Biol 2007;93:354–3662.

Moos T, Oates PS, Morgan EH. Expression of the neuronal transferrin receptor is age dependent and susceptible to iron deficiency. J Comp Neurol 1998;398:420–430.

Muldoon LL, Pagel MA, Kroll RA, Roman-Goldstein S, Jones RS, Neuwelt EA. A physiological barrier distal to the anatomic blood-brain barrier in a model of transvascular delivery. AJNR Am J Neuroradiol 1999;20:217–222.

Mullin L, Gessner R, Kwan J, Kaya M, Borden MA, Dayton PA. Effect of anesthesia carrier gas on in vivo circulation times of ultrasound microbubble contrast agents in rats. Contrast Media Mol Imaging 2011;6:126–131.

Nance E, Timbie K, Miller GW, Song J, Louttit C, Klibanov AL, Shih TY, Swaminathan G, Tamargo RJ, Woodworth GF, Hanes J, Price RJ. Non-invasive delivery of stealth, brain-penetrating nanoparticles across the blood-brain barrier using MRI-guided focused ultrasound. J Control Release 2014;189:123–132.

Nhan T, Burgess A, Cho EE, Stefanovic B, Lilge L, Hynynen K. Drug delivery to the brain by focused ultrasound induced blood-brain barrier disruption: Quantitative evaluation of enhanced permeability of cerebral vasculature using two-photon microscopy. J Control Release 2013;172:274–280.

Pardridge WM. Drug transport across the blood-brain barrier. J Cereb Blood Flow Metab 2012;32:1959–1972.

Pardridge WM. Blood-brain barrier drug delivery of IgG fusion proteins with a transferrin receptor monoclonal antibody. Expert Opin Drug Deliv 2015;12:207–222.

Poon C, McMahon D, Hynynen K. Noninvasive and targeted delivery of therapeutics to the brain using focused ultrasound. Neuropharmacology 2017;120:20–37.

Rapoport SI. Osmotic opening of the blood-brain barrier: Principles, mechanism, and therapeutic applications. Cell Mol Neurobiol 2000;20:217–230.

Sharma G, Sharma AR, Lee SS, Bhattacharya M, Nam JS, Chakraborty C. Advances in nanocarriers enabled brain targeted drug delivery across blood brain barrier. Int J Pharm 2019;559:360–372.

Sheikov N, McDannold N, Sharma S, Hynynen K. Effect of focused ultrasound applied with an ultrasound contrast agent on the tight junctional integrity of the brain microvascular endothelium. Ultrasound Med Biol 2008;34:1093–1104.

Sheikov N, McDannold N, Vykhodtseva N, Jolesz F, Hynynen K. Cellular mechanisms of the blood-brain barrier opening induced by ultrasound in presence of microbubbles. Ultrasound Med Biol 2004;30:979–989.

Tardoski S, Gineyts E, Ngo J, Kocot A, Clezardin P, Melodelima D. Low-intensity ultrasound promotes clathrin-dependent endocytosis

for drug penetration into tumor cells. Ultrasound Med Biol 2015;41:2740–2754.

Taylor EM, Morgan EH. Developmental changes in transferrin and iron uptake by the brain in the rat. Brain Res Dev Brain Res 1990;55:35–42.

Thomsen LB, Linemann T, Birkelund S, Tarp GA, Moos T. Evaluation of targeted delivery to the brain using magnetic immunoliposomes and magnetic force. Materials (Basel) 2019;12:3576.

Thomsen MS, Routhe LJ, Moos T. The vascular basement membrane in the healthy and pathological brain. J Cereb Blood Flow Metab 2017;37:3300–3317.

Ting CY, Fan CH, Liu HL, Huang CY, Hsieh HY, Yen TC, Wei KC, Yeh CK. Concurrent blood-brain barrier opening and local drug delivery using drug-carrying microbubbles and focused ultrasound for brain glioma treatment. Biomaterials 2012;33:704–712.

Treat LH, McDannold N, Zhang Y, Vykhodtseva N, Hynynen K. Improved anti-tumor effect of liposomal doxorubicin after targeted blood-brain barrier disruption by MRI-guided focused ultrasound in rat glioma. Ultrasound Med Biol 2012;38:1716–1725.

White E, Woolley M, Bienemann A, Johnson DE, Wyatt M, Murray G, Taylor H, Gill SS. A robust MRI-compatible system to facilitate highly accurate stereotactic administration of therapeutic agents to targets within the brain of a large animal model. J Neurosci Methods 2011;195:78–87.

Wolak DJ, Thorne RG. Diffusion of macromolecules in the brain: implications for drug delivery. Mol Pharm 2013;10:1492–1504.

Yu YJ, Zhang Y, Kenrick M, Hoyte K, Luk W, Lu Y, Atwal J, Elliott JM, Prabhu S, Watts RJ, Dennis MS. Boosting brain uptake of a therapeutic antibody by reducing its affinity for a transcytosis target. Sci Transl Med 2011;3 84ra44.

Yuan HY, Zhang SL. Effects of particle size and ligand density on the kinetics of receptor-mediated endocytosis of nanoparticles. Appl Phys Lett 2010;96 033704.

Supplementary Information for

Focused ultrasound and microbubble treatment increases delivery of transferrin receptor-targeting liposomes to the brain

Marieke Olsman[1], Viktoria Sereti[2], Melina Muehlenpfordt[1], Kasper Bendix Johnsen[2], Thomas Lars Andresen[2], Andrew James Urquhart[2], Catharina de Lange Davies[1]

[1] Department of Physics, Norwegian University of Science and Technology, Høgskoleringen 5, 7491 Trondheim, Norway

[2] Department of Health Technology, Technical University Denmark, Ørsteds Plads, building 345C, DK-2800 Kongens Lyngby, Denmark

Corresponding author

Marieke Olsman, marieke.olsman@ntnu.no

Department of Physics, Norwegian University of Science and Technology, Høgskoleringen 5, 7491 Trondheim, Norway

Acoustic attenuation through the rat pup skull

The attenuation of the acoustic pressure through the rat skull was measured in a tank filled with degassed water. Harvested skull bone from animals (n=6, p14-p17) used during the BBBD experiments were placed 3-4 mm in front of a hydrophone (Onda, HGL-0200). The hydrophone was connected to a pre-amplifier (AG-2010) and mounted to a motorized 3D stage (Onda, AIMS III) and positioned in the focus of the transducer (60 mm). The acoustic attenuation of 30 cycle US pulses was measured at three different locations for each piece of parietal bone. The acoustic signals measured by the hydrophone were sent to an oscilloscope (PicoScope, 5244A) and post processed on a PC (Soniq Software). The average attenuation of the 6 skull bones was approximately 27±9% and used to estimate the *in situ* pressure during FUS treatment.

FUS induced BBBD shown in axial, coronal and sagittal planes of the brain

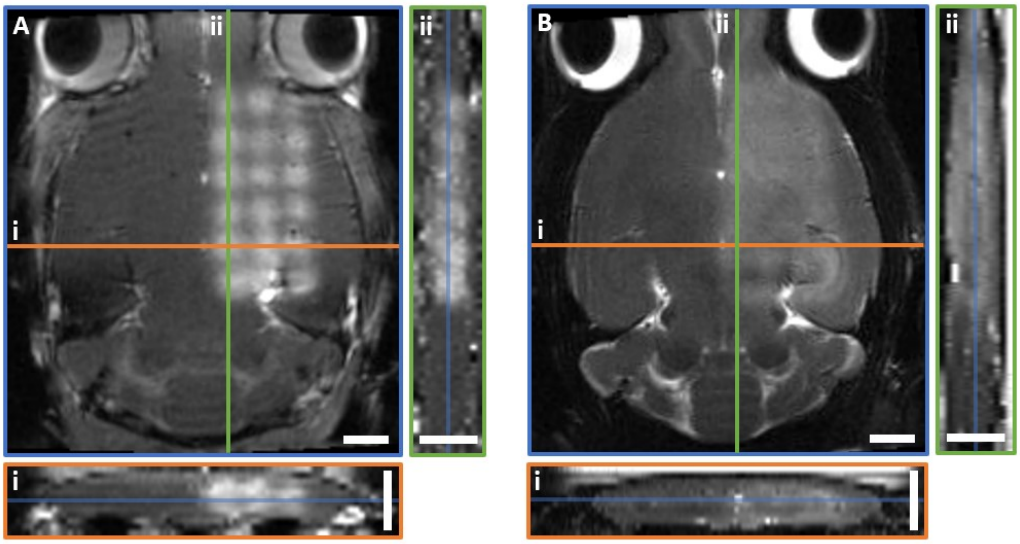

Figure S1: FUS-induced BBBD shown in the axial, coronal and sagittal plane of the brain. (A) Axial T1-weighted FLASH MR image at eye height and its (i) coronal and (ii) sagittal view. Increase in image intensity indicates extravasation of gadolinium contrast agent. (B) Axial T2-weighted MR image at eye height and its (i) coronal and (ii) sagittal view. Increase in image intensity indicates presence of oedema. (Scalebar in axial images 2 mm, Scalebar in coronal and sagittal images 12 mm).

Different extents of FUS-induced BBBD

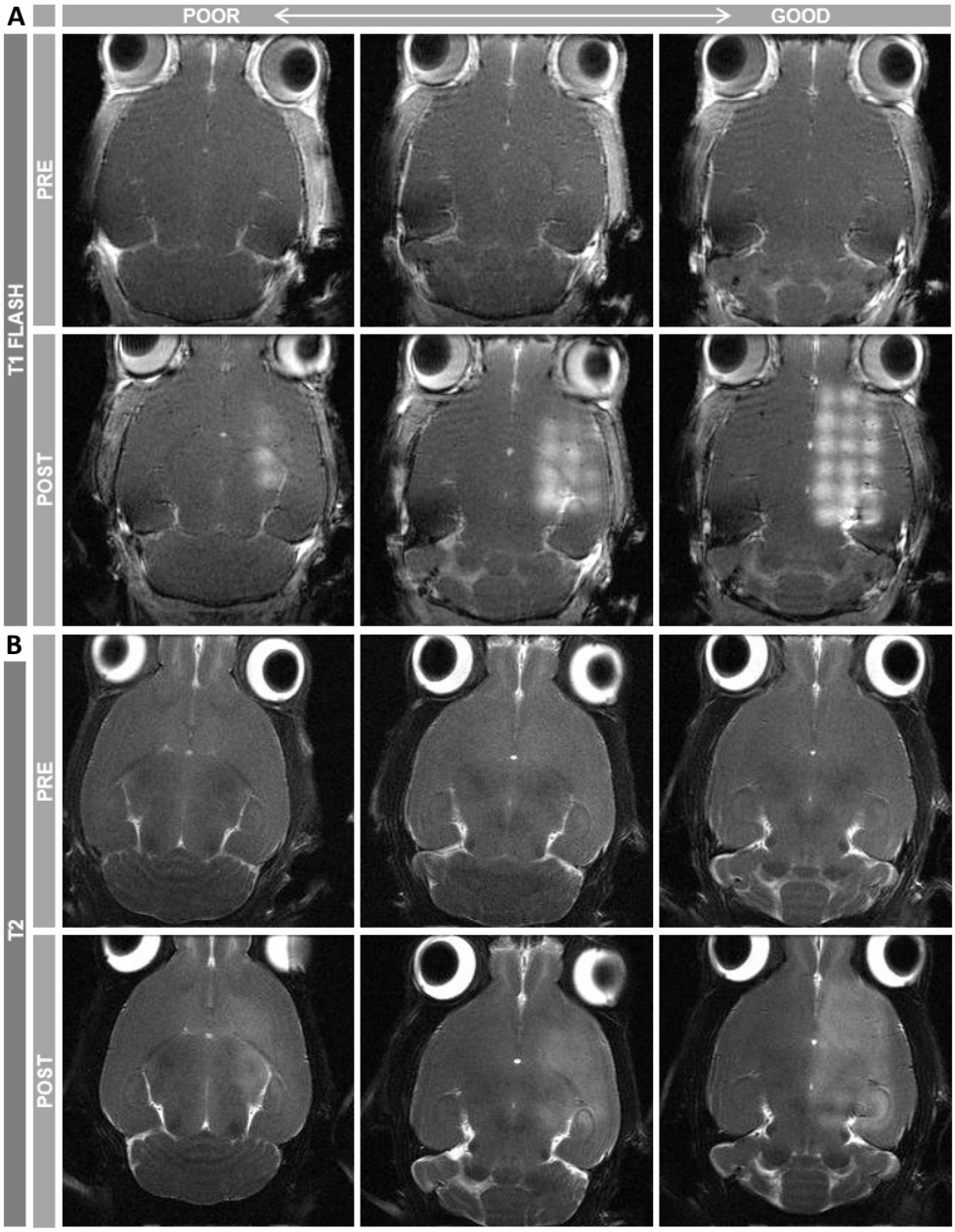

Figure S2: Representative images of (A) T1 FLASH images (T1) and (B) corresponding T2 images showing different extents of FUS-mediated BBBD.

Extent of BBBD for the isotype IgG and Anti-TfR liposomes treatment group

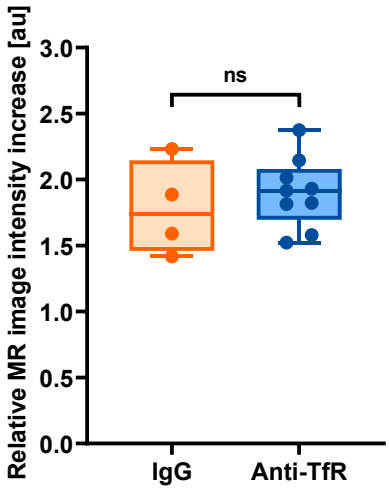

Figure S3: Relative MR image intensity increase plotted per liposome. An unpaired t-test showed no statistically significant difference between the two groups. Each symbol depicts an animal. (n=4 and n=9 for the isotype IgG and Anti-TfR treatment group, respectively)

CLSM image superimposed with the T1-weighted FLASH MR image

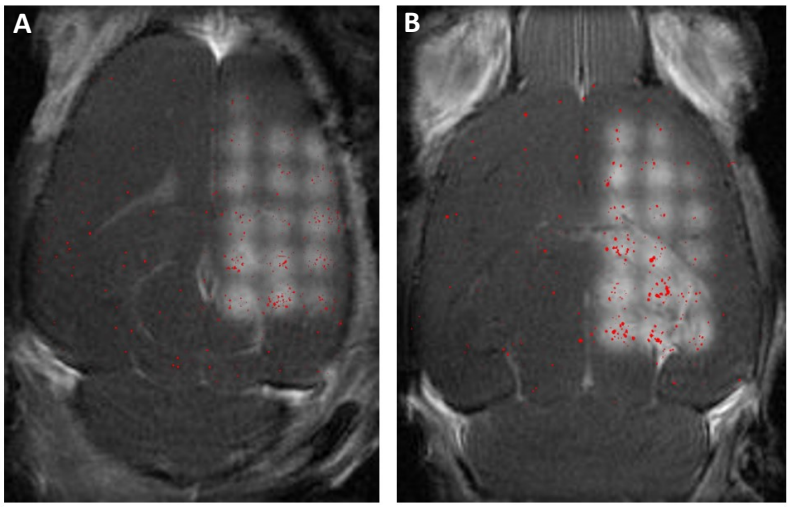

Figure S4: Liposomal channel of the CLSM image (red) superimposed on the corresponding T1-weighted FLASH images for an animal treated with the (A) isotype IgG liposome and (B) Anti-TfR liposome. Prior to superimposing the images, the microscopy image was thresholded, the background was removed and the image was cropped to only show liposomal signal in the hemispheres. Procedure was the same for both examples presented.

Example of CLSM tilescan of a section of which the corresponding MR image shows low gadolinium contrast at site of FUS treatment

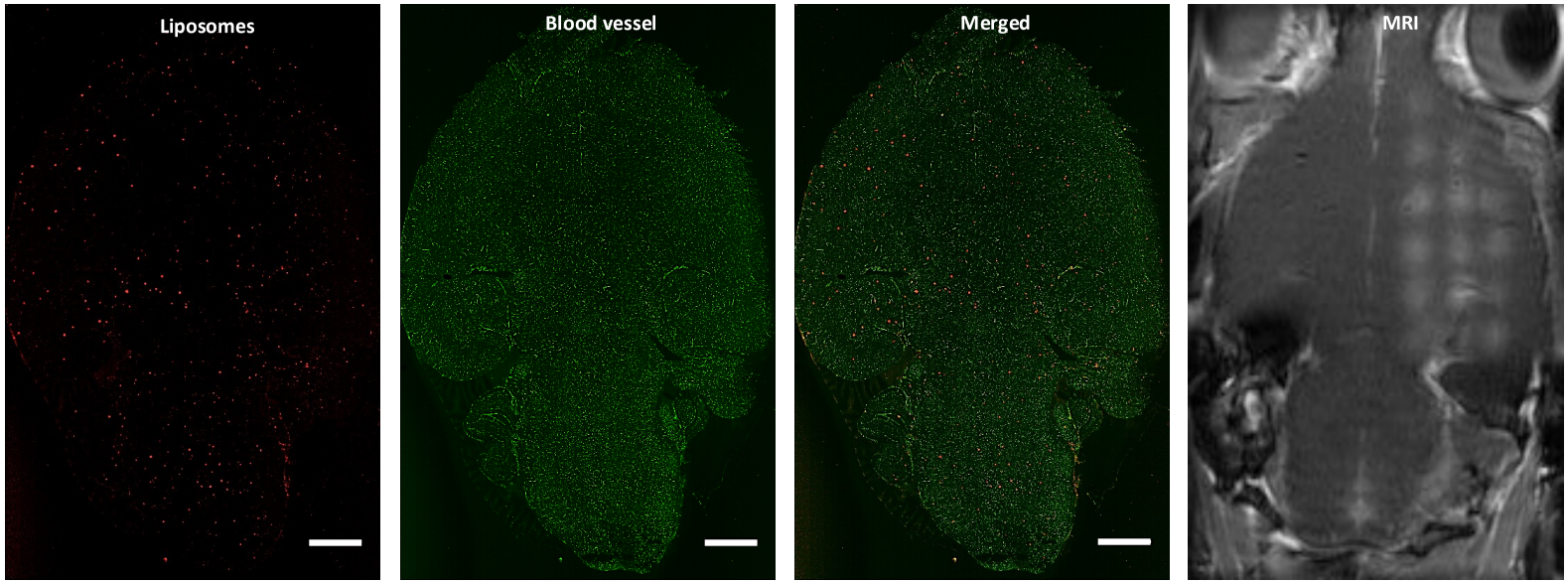

Figure S5: CLSM tile scan and corresponding MR image of an animal injected with the Anti-TfR liposome. Liposome (red) and blood vessel (green) image are shown separately and merged. Corresponding MR image shows low gadolinium enhanced contrast at the site of FUS treatment. Based on visual inspection, liposomal delivery to the FUS-treated hemisphere does not seem to be as profound as observed previously. No clear pattern or increase of liposomal delivery can be observed. Scalebar is 2000 µm.

High magnification CLSM images of animals injected with the isotype IgG liposome

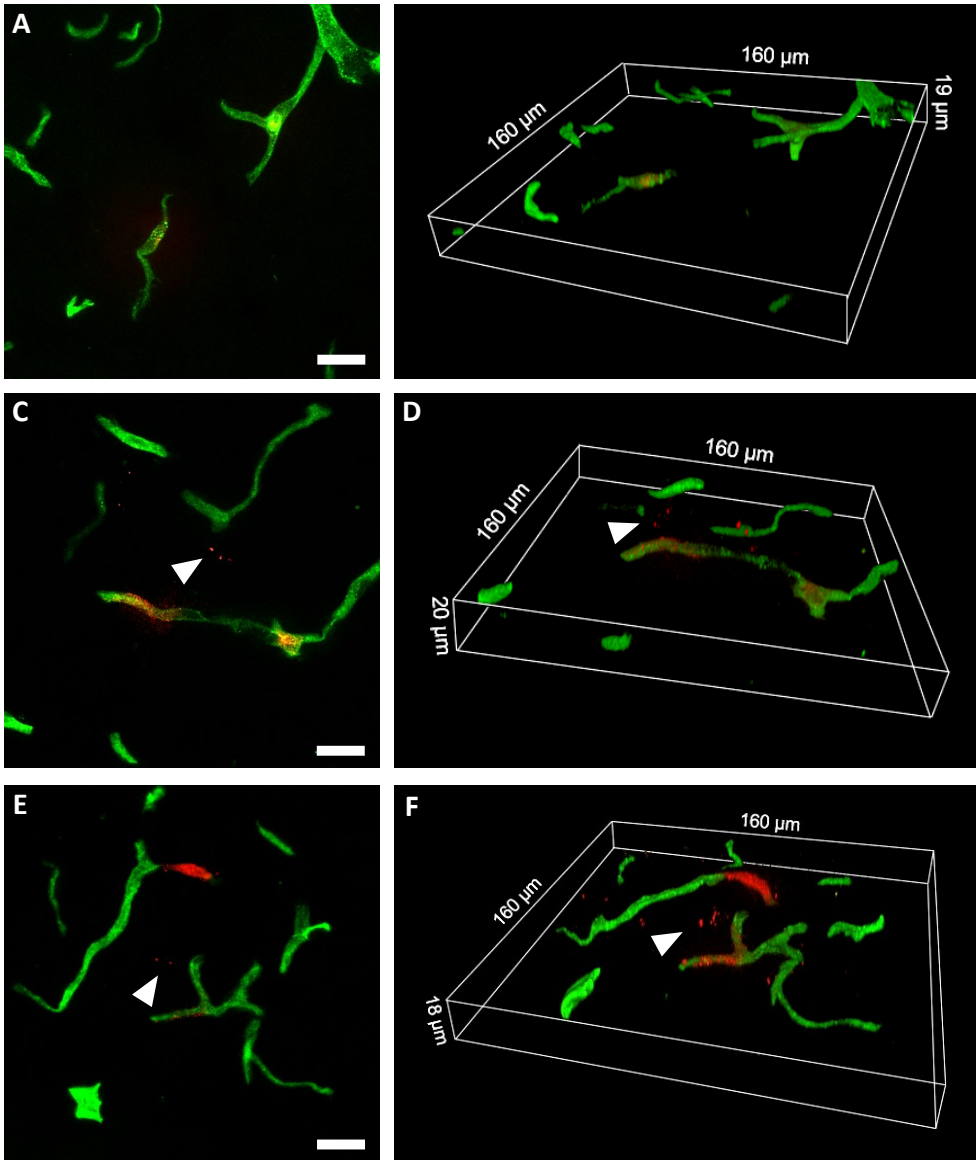

Figure S6: (A,C,E) High magnification CLSM images and (B,D,F) corresponding 3D renderings of those images acquired in sections of an animal injected with the isotype IgG liposomes. Liposomes and blood vessels are shown in red and green, respectively. Liposomes are found intravascular in the control hemisphere (A,B) while in the FUS-treated hemisphere (C-F), the liposomes are located mainly extravascular. Arrows indicate liposomes that are possibly located in the brain parenchyma. Scalebar is 20 µm.

High magnification CLSM images of animals injected with the Anti-TfR liposome

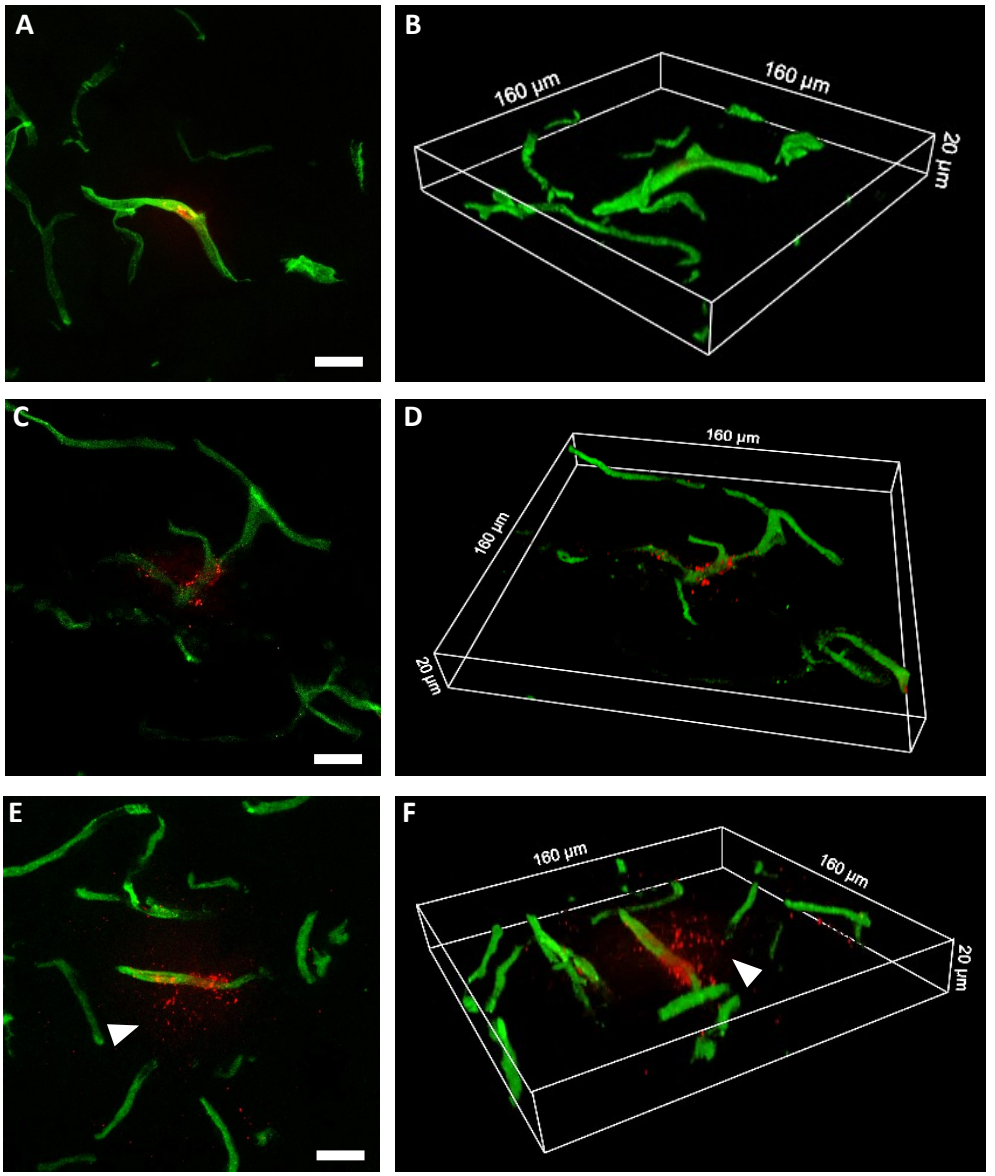

Figure S7: (A,C,E) High magnification CLSM images and (B,D,F) corresponding 3D renderings of those images acquired in sections of an animal injected with the Anti-TfR liposomes. Liposomes and blood vessels are shown in red and green, respectively. Liposomes are found intravascular in the control hemisphere (A,B) while in the FUS-treated hemisphere (C-F), the liposomes are located mainly extravascular. Arrows indicate liposomes that are possibly located in the brain parenchyma. Scalebar is 20 µm.

PAPER III

Acoustic Cluster Therapy (ACT®) increases blood-brain barrier permeability and enhances accumulation of core-crosslinked polymeric micelles

Marieke Olsman*, Melina Mühlenpfordt*, Emma Bøe Olsen, Sverre Helge Torp, Spiros Kotopoulis, Cristianne Rijcken, Qizhi Hu, Marielle Thewissen, Sofie Snipstad, Catharina de Lange Davies
*Equal contribution

Prepared for submission

PAPER IV

Real-time intravital multiphoton microscopy to visualize focused ultrasound and microbubble treatments to increase blood-brain barrier permeability

Charissa Poon, Melina Mühlenpfordt*, Marieke Olsman*, Spiros Kotopoulis, Catharina de Lange Davies, Kullervo Hynynen
**Equal contribution*

Submitted to Journal of Visualized Experiments

ISBN 978-82-326-5447-5 (printed ver.)
ISBN 978-82-326-5419-2 (electronic ver.)
ISSN 1503-8181 (printed ver.)
ISSN 2703-8084 (online ver.)

NTNU

Norwegian University of
Science and Technology